

# Thermalization and hydrodynamics in integrable systems

A Thesis

Submitted to the

Tata Institute of Fundamental Research, Mumbai

Subject Board of Physics

for the degree of Doctor of Philosophy

by

**Saurav Pandey**

International Centre for Theoretical Sciences

Tata Institute of Fundamental Research

June, 2025

## DECLARATION

This thesis is a presentation of my original research work. Wherever contributions of others are involved, every effort is made to indicate this clearly, with due reference to the literature, and acknowledgment of collaborative research and discussions.

The work was done under the guidance of Professor Abhishek Dhar at the International Centre for Theoretical Sciences, Tata Institute of Fundamental Research, Bengaluru.



Saurav Pandey

In my capacity as the formal supervisor of record of the candidate's thesis, I certify that the above statements are true to the best of my knowledge.



**Abhishek Dhar**

Date: June 20, 2025

## ACKNOWLEDGEMENTS

First and foremost, I sincerely thank my supervisor, Prof. Abhishek Dhar, for guiding me through my PhD journey. I have learned much from him and greatly admire his intuition and ability to simplify complicated ideas. I thank my collaborator Prof. Anupam Kundu with whom I first started my journey into statistical physics through projects before registering for my PhD. I also thank Prof. Manas Kulkarni with whom I had valuable discussions that helped me in my research. I thank Junaid for guiding me through my first work.

I thank my friends that I made at ICTS: Saikat, Aditya, Chandra, Jitendra, Manju, Saumav, Srashti, Rekha, Akshay, Sunidhi, and others, without whom my stay at ICTS would be much less happening. I thank Sunidhi and Saikat for all the good food they made for me. I thank the various people with whom I played football and badminton both of which I learned after coming here. I thank Rajarshi with whom I shared my office for being very helpful. I also thank my juniors with whom I have interacted.

I am grateful to my mother for being a constant source of inspiration in my life. Lastly, I thank ICTS for providing a lively research atmosphere, for its computational facilities, and for providing financial support to attend conferences.



# Contents

<b>1 Introduction</b>	<b>9</b>
1.1 Typicality and the Boltzmann entropy	10
1.2 Thermalization and hydrodynamics	13
<b>2 Boltzmann entropy of a freely expanding quantum ideal gas</b>	<b>17</b>
2.1 Boltzmann entropy for quantum systems	17
2.2 An illustrative example: a one-dimensional quantum ideal gas	20
2.3 Microscopic model and dynamical evolution	23
2.3.1 Density matrix	24
2.3.2 Wigner distribution function	27
2.4 Choices of macrostates and the corresponding entropies	28
2.4.1 $U$ -macrostate and $S_B^U$	28
2.4.2 $f$ -macrostate and $S_B^f$	31
2.5 Numerical results	36
2.5.1 Fermions	37
2.5.2 Bosons	42
2.6 Discussions and summary	44
<b>3 Generalized hydrodynamics and approach to Generalized Gibbs equilibrium for a classical harmonic chain</b>	<b>49</b>
3.1 Microscopic description of the system	51
3.2 Wigner function, conserved quantities and connection to GHD	54
3.2.1 Wigner function: its relation to the correlation matrix and evolution	54
3.2.2 Conserved quantities and connection to GHD	58

3.3 Comparison between microscopic and hydrodynamic evolution from do-	
main wall initial condition . . . . .	60
3.3.1 Domain wall initial condition composed of two GE states . . . . .	61
3.3.2 Domain wall initial condition composed of two GGE states . . . . .	69
3.4 Discussions and summary . . . . .	78
<b>4 Conclusions</b>	<b>81</b>
<b>Appendix A</b>	<b>85</b>
A.1 Marginals of the wavepacket density . . . . .	85
A.2 Maximizing the von Neumann entropy . . . . .	86
A.3 Dependence on $K$ . . . . .	88
A.4 Glossary . . . . .	89
<b>Appendix B</b>	<b>93</b>
B.1 GGE partition function . . . . .	93
B.2 Density evolution corresponding to the initial condition composed of two	
GGEs . . . . .	94
<b>Bibliography</b>	<b>105</b>
<b>Publications</b>	<b>107</b>

**Abstract:** Thermalization refers to the process in which macroscopic observables evolve with time and eventually attain constant values defined by an equilibrium ensemble. The microscopic understanding of thermalization is an active area of research. In one of our works, we study the time evolution of the Boltzmann entropy of a microstate during the non-equilibrium free expansion of a one-dimensional quantum ideal gas. This quantum Boltzmann entropy,  $S_B$ , essentially counts the “number” of independent wavefunctions (microstates) giving rise to a specified macrostate. It generally depends on the choice of macrovariables, such as the type and amount of coarse-graining, specifying a *non*-equilibrium macrostate of the system, but its extensive part agrees with the thermodynamic entropy in thermal equilibrium macrostates. We examine two choices of macrovariables: the  $U$ -macrovariables are local observables in position space, while the  $f$ -macrovariables also include structure in momentum space. For the quantum gas, we use a non-classical choice of the  $f$ -macrovariables. For both choices, the corresponding entropies  $s_B^f$  and  $s_B^U$  grow and eventually saturate. Similar to a classical ideal gas, the growth rate of  $s_B^f$  depends on the momentum coarse-graining scale. If the gas is initially at equilibrium and is then released to expand to occupy twice the initial volume, the per-particle increase in the entropy for the  $f$ -macrostate,  $\Delta s_B^f$ , satisfies  $\log 2 \leq \Delta s_B^f \leq 2 \log 2$  for fermions, and  $0 \leq \Delta s_B^f \leq \log 2$  for bosons. For the same initial conditions, the change in the entropy  $\Delta s_B^U$  for the  $U$ -macrostate is greater than  $\Delta s_B^f$  when the gas is in the quantum regime where the final stationary state is not at thermal equilibrium. One could also study thermalization from a hydrodynamic perspective. In another work, we study the evolution of a classical harmonic chain with nearest-neighbor interactions starting from domain wall initial conditions. The initial state is taken to be either a product of two Gibbs Ensembles (GEs) with unequal temperatures on the two halves of the chain or a product of two Generalized Gibbs Ensembles (GGEs) with different parameters in the two halves. For this system, we construct the Wigner function and demonstrate that its evolution defines the Generalized Hydrodynamics (GHD) describing the evolution of the conserved quantities. We solve the GHD for both finite and infinite chains and compute the evolution of conserved densities and currents. For a finite chain with fixed boundaries, we show that these quantities relax as  $\sim 1/\sqrt{t}$  to their respective steady-state values given by the final expected GE or GGE state, depending on the initial conditions.

Exact expressions for the Lagrange multipliers of the final expected GGE state are obtained in terms of the steady state densities. In the case of an infinite chain, we find that the conserved densities and currents at any finite time exhibit ballistic scaling while, at infinite time, any finite segment of the system can be described by a current-carrying non-equilibrium steady state (NESS). We compute the scaling functions analytically and show that the relaxation to the NESS occurs as  $\sim 1/t$  for the densities and as  $\sim 1/t^2$  for the currents. We compare the analytic results from hydrodynamics with those from exact microscopic numerics and find excellent agreement.

# Chapter 1

## Introduction

Thermodynamics is a branch of physics that studies quantities like heat and work and their relation to internal properties of matter like energy and entropy. It is governed by the famous laws of thermodynamics which are phenomenological statements establishing basic thermodynamic quantities like temperature, entropy, heat, and work and the relations between them. The second law of thermodynamics stands out from the rest as it is a statement about the impossibility of certain processes in nature. In one of its forms, it tells us that if we put a higher-temperature body in thermal contact with a lower-temperature body, then heat flows from the hotter to the colder body until they are in thermal equilibrium i.e. have the same temperature. This process of attaining thermal equilibrium is irreversible and is known as thermalization. One of the major issues in understanding thermalization has been to reconcile the time-reversibility of the microscopic laws of physics with the emergent irreversibility of the laws of thermodynamics.

Before going into the details of thermalization which is a non-equilibrium phenomenon, let us first try to understand the microscopic origins of equilibrium statistical mechanics. The explanation, found in most textbooks, is the ergodic hypothesis (see [1] and the references therein). It states that, for an isolated system, the long-time averages of observables are equal to the average values computed from a microcanonical ensemble, subject to the macroscopic constraints. The argument is that a chaotic system will, over time, explore the entire available phase space densely. There are however many issues with this explanation. The time it requires for a trajectory to explore the available phase space is exponentially large in system size. Whether a system is ergodic or not should

therefore be irrelevant on much smaller time scales at which thermalization takes place. Another objection is that the ergodic hypothesis only talks about long-time averages of observables while in actual experiments, it is the observables themselves that relax to their respective equilibrium values.

A more compelling explanation for thermalization is the concept of *typicality* [2] (see Chapter 14 on Gibbs and Boltzmann Entropy in Classical and Quantum Mechanics) that uses the notion of macrovariables which are nothing but coarse-grained observables. It states that most microscopic configurations correspond to the observables having their typical i.e. equilibrium values, subject to the constraints. Though the concept applies equally well to classical and quantum systems, we stick to the classical case here for simplicity of arguments. The central idea is that a given choice of observables divides the accessible phase space into two parts: an equilibrium part and a non-equilibrium part. As we increase the system size, the equilibrium region becomes much larger in volume than the non-equilibrium region. Hence, in the thermodynamic limit of large system size, the equilibrium region covers almost the entire available phase space. In [3], it was rigorously shown that for classical systems, assuming short-ranged interactions and local observables, the equilibrium region in the thermodynamic limit is exponentially large in system size compared to the non-equilibrium part. This would explain the much shorter time scales observed in the thermalization of physical systems as compared to the time taken by a trajectory to fill the entire phase space. Here, the thermodynamic limit plays a crucial role in thermalization as we would expect from statistical mechanics. Typically, a system starts in the non-equilibrium region of the phase space, but then quickly evolves to the much larger equilibrium region and stays there for very long periods of time. The formulation also allows for a finite system to occasionally leave the equilibrium region, though it is expected to happen on time scales much larger than it takes for the system to thermalize but much smaller than the Poincare recurrence time [4].

## 1.1 Typicality and the Boltzmann entropy

Since thermalization is an irreversible process, it is closely related to entropy. For the first time, the notion of entropy appeared in Clausius' formulation of the second law of

thermodynamics [5]. It is defined as an extensive property of systems, like internal energy. However, it has a very peculiar nature in that the entropy of an isolated system can only increase. In fact, it always increases for irreversible processes like thermalization. This presents a major challenge in the conceptual understanding of the microscopic origins of thermalization. The microscopic laws of nature like Newton’s equation for classical systems or Schrodinger’s equation for quantum systems are time-reversible. One of the major issues is to reconcile this microscopic reversibility with the emergent irreversibility, such as thermalization, at the macroscopic scales.

It was one of the most remarkable achievements of Boltzmann [6–14] to understand the origins of macroscopic irreversibility. He constructed an entropy function, satisfying the second law, for a typical individual microstate  $X$  of a macroscopic system that is in a macrostate specified by the values of a collection of macrovariables. This Boltzmann entropy is defined for systems both in and out of equilibrium as the logarithm of the “number” of microstates corresponding to the system’s macrostate. For a classical system, the microstates are specified by points  $X$  in phase space, and the Boltzmann entropy of  $X$  is, up to an additive constant, the logarithm of the phase space volume of the set of all microstates for which the macrovariables have the same values as they do for  $X$ . For a quantum system, the microstates are specified by wave functions  $|\Phi\rangle$ . This difference, which allows observables to have indeterminate values in the quantum microstate, can make the precise definition of quantum macrovariables and macrostates somewhat subtle [15–18], and also allows for new non-classical choices of macrovariables. The Boltzmann entropy of  $|\Phi\rangle$  is then the logarithm of the number of independent wave functions that have the same values of the chosen macrovariables as  $|\Phi\rangle$  does. At thermal equilibrium, for all proper choices of macrovariables, this definition coincides in its extensive part with the thermodynamic entropy of Clausius.

One of the simplest irreversible processes is the Joule expansion of gases as shown in the numerical demonstration in Fig. (1.1). A gas of particles, in a state of thermal equilibrium, is initially confined to a part of a container while the remaining region is a vacuum. As the confinement is removed, the gas rushes to fill the vacuum and eventually fills the entire container uniformly. For a classical ideal gas, it is well-known from thermodynamics, that the change in entropy per particle is  $\ln 2$  which can be easily computed by

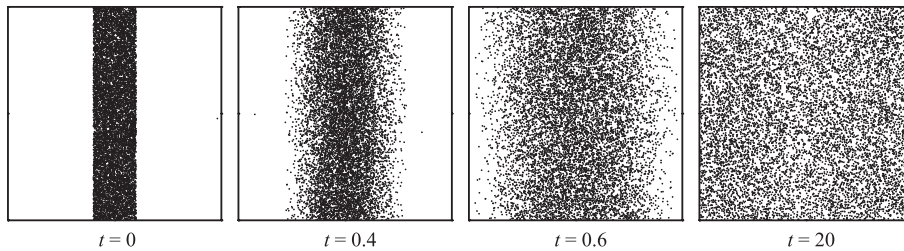


Figure 1.1: [Taken from [22]] Numerical simulation of the free expansion on the 2-torus of a non-interacting gas of  $10^4$  particles having a thermal distribution of momenta with mean thermal speed equal to unity, initially confined in the horizontal direction to the region  $0.4 < x < 0.6$ , at the sequence of times indicated.

replacing the highly irreversible expansion with an isothermal process. However, it would be interesting if we could determine the entropy growth curve itself. In a paper [19], the time evolution of the Boltzmann entropy for a freely expanding *classical* hard point gas (HPG) using two different choices of macrovariables was investigated. It was found that the resulting entropies grow and saturate, however, the growth is not necessarily monotonic and the entropy curves corresponding to different choices of macrostates may not coincide. This is due to the absence of interactions. In [20], the study was extended to the alternate mass hard particle gas (AMHPG) which is an interacting system. There the entropy curves are found to coincide with each other and show monotonic growth in agreement with the second law of thermodynamics. The  $f$ -macrostate entropy for 2-D hard rods was recently studied in [21].

As part of our thesis, we have extended the study in [19] to a freely expanding *quantum* ideal gas [23]. Our primary motive is to show that the notion of typicality and the Boltzmann entropy for individual microstates out of equilibrium work equally well in the quantum regime. We also wanted to see if the quantum statistics changes the classical results both qualitatively and quantitatively. To that extent, we studied both fermions and bosons in the low and high-temperature regimes. Before moving on, we mention some of the earlier works relevant to our study. Quantum quench of non-interacting fermions under various protocols have been studied using Wigner functions in [24, 25]. Lattice fermions evolving from domain wall initial conditions have been studied with a focus on the evolution of the density profile and the growth of entanglement entropy [26, 27]. The

diagonal entropy for isolated quantum systems has been studied [28] for both integrable and non-integrable cases. Some other recent relevant discussions of entropy in quantum systems in the nonequilibrium setting can be found in Refs. [29–33].

## 1.2 Thermalization and hydrodynamics

Another important tool in understanding the evolution of macroscopic systems is the theory of hydrodynamics. It studies the evolution of slowly varying macroscopic fields over an intermediate time scale that is larger than the time it takes for transient quantities to relax but smaller than the time it takes for the system to thermalize. Hydrodynamics works by first identifying the conserved quantities and writing down the continuity equations involving the conserved densities and the associated currents. We then choose to look at the system over intermediate length and time scales in which the transient quantities have relaxed and the system is in a state of local thermal equilibrium (LTE). This implies that at the Euler scale, the system must be completely characterized by the conserved densities. Hence the currents must be functionals of the densities themselves. Finding these functional dependences yields us with a hydrodynamic description of the system. The fundamental equations of hydrodynamics are the Euler equations [34] for ideal fluids and the Navier-Stokes corrections [35] taking dissipation into account.

Based on the number of functionally independent conserved quantities, systems can be classified into integrable and non-integrable. Systems where the number of conserved quantities does not scale with the number of degrees of freedom are called non-integrable. A generic isolated Hamiltonian system typically has few conserved quantities like the total particle number, the total momentum, and the total energy. On the other hand, an integrable system has an extensive number of conserved quantities and can be interacting or non-interacting. Thermalization is usually discussed in the context of non-integrable systems where the chaotic nature of interactions is believed to self-thermalize a system. For a chaotic system, a trajectory would, over time, lose information about almost all initial conditions and evolve to a Gibbs state characterized by a few conserved quantities and the corresponding intensive parameters such as density and temperature.

Recently, the notion of thermalization in integrable systems has gained considerable

interest. Such systems are expected to equilibrate to a Generalized Gibbs Ensemble (GGE) [36] which keeps information about all the conserved quantities. The relaxation and approach to a steady state has been shown in non-interacting integrable models such as the hard particle gas (HPG) [19] and the harmonic chain [37] and in interacting integrable models such as hard rods [38] and the Toda chain [39]. Thermalization for a low-density free fermion lattice model is shown rigorously in [40]. The approach to GGE however has been demonstrated mainly in quantum integrable models [28,36,41-44].

Hydrodynamics also has traditionally been applied to non-integrable systems, where the assumption of local thermal equilibrium is expected to hold due to the mixing property of the dynamics. For integrable systems, it is now widely accepted (see [42,45] and the references therein) that hydrodynamics still works and is referred to as generalized hydrodynamics (GHD) which is written in terms of the quasi-particle density and provides the evolution of all the slowly varying conserved fields. As mentioned above, integrable systems can be further classified into two categories: Non-interacting and interacting. In the former case, the GHD equations are easier to write down as the quasi-particles do not undergo any phase shifts. Common examples include the harmonic chain for which hydrodynamic equations were derived both at the Euler level [46] (see also [47]) and with higher derivative corrections [48], and the HPG [19]. On the other hand for the interacting case, quasi-particles undergo phase shifts upon collision. The simplest example of such systems is a collection of hard rods for which the hydrodynamic equations were written long back [49-51]. For the case of interacting integrable quantum systems, GHD was derived more recently [52,53] and quite remarkably they have the same structure as the classical systems [45]. A number of studies have established GHD for several interacting classical and quantum integrable systems such as Toda chain [54-57], the  $\delta$ -Bose gas [58] and hard rods [38,59]. GHD has been successfully used to understand unusual equilibration of trapped integrable systems [60-62] and also the predictions of GHD have been experimentally verified [63].

It is easy to see that, even among integrable systems, thermalization and the applicability of hydrodynamics to non-interacting cases would be the most surprising. The harmonic chain provides us with an example of a non-interacting integrable system that is analytically tractable and allows macroscopic description in terms of hydrodynamics.

For this system, a detailed comparison of the microscopic and hydrodynamic calculations is possible. Approach to GGE starting from a domain wall initial condition with unequal temperatures in the two halves has been studied for the case of an infinite quantum harmonic chain in [64] where the Lagrange multipliers of the final GGE state were evaluated explicitly. Convergence of the phase space distribution to a Gaussian stationary measure, starting from an initial state which is also Gaussian, is studied in [65]. In [66], two families of conserved quantities for infinite harmonic lattices were shown and the convergence of the covariance matrix to its stationary form was studied. Hydrodynamic approaches have also been applied to harmonic systems. In [46], starting from a family of initial states that are slowly varying in space, the hydrodynamic equation of an infinite classical harmonic chain was derived at the Euler level in terms of what is referred to as the spectral density matrix function (SDMF) in the paper, which is essentially the Fourier transform of the correlation matrix defined in a coarse-grained cell around a macroscopic point. The study was extended in [48] where the next-order correction (in space-time scaling parameter) to the Euler equation was derived. Alternatively, macroscopic evolution in the harmonic chain has been studied using Wigner functions [67–70]. The harmonic chain being an integrable system, one expects a generalized hydrodynamic description for the macro-evolution. However, the connections between the correlation matrix approach [46, 48] and the Wigner function method [67] have not been elaborated in the physics literature. Furthermore, and somewhat surprisingly, their relationship to GHD remains unexplored. In our work [71], we have addressed this gap and elucidated these connections which we then used to understand the non-equilibrium evolution and approach to the stationary state. We considered a classical harmonic chain with nearest-neighbor interactions either of finite length (with fixed boundary conditions) or of infinite extent. Initially, the system is prepared in a domain wall configuration by taking the two halves of the chain either in thermal equilibrium with unequal temperatures or in different GGEs with unequal parameters (Lagrange multipliers). Starting from this initial condition, we studied the evolution of the chain and the approach to the stationary state in the long time limit (for the finite case). For the density and current profiles, we found very good agreement between the coarse-grained microscopic and the GHD results.

In brief, the thesis addresses two main investigations and is organized as follows. In

chapter (2), we study the evolution of the Boltzmann entropy during the non-equilibrium free expansion of a quantum ideal gas. We discuss two choices of macrostates and calculate the corresponding entropies. In chapter (3), we study the hydrodynamic evolution and approach to a generalized Gibbs ensemble for a classical harmonic chain starting from domain-wall initial states. In chapter (4), we summarize our findings and discuss potential outlooks.

# Chapter 2

## Boltzmann entropy of a freely expanding quantum ideal gas

In this chapter, we study the evolution of the Boltzmann entropy during the free expansion of an ideal quantum gas. The summary of the formalism can be found in [2] (see Chapter 14 on Gibbs and Boltzmann Entropy in Classical and Quantum Mechanics). In [19], this formalism was first applied to the case of a classical ideal gas. In this study, we extend their work to the case of quantum ideal gases. Refer to appendix (A.4) for a glossary of the notations used in this work.

### 2.1 Boltzmann entropy for quantum systems

Let us now discuss the construction of macrostates and the Boltzmann entropy for isolated macroscopic quantum systems. For a more detailed discussion see Refs. [15–17]. Consider a quantum system with a Hilbert space  $\mathcal{H}$ , whose wave function lies in an energy shell  $\mathcal{H}_E$  of width  $\Delta E \ll E$ . As macro observables, one option is to choose a set of commuting coarse-grained operators  $\{\hat{M}_k\}$ ,  $k = 1, \dots, J$ , meaning that the eigenvalues of each operator are grouped into “bins” and all eigenvalues of that operator within each bin are set equal. The simultaneous diagonalization of all the  $\hat{M}_k$  operators then provides

a decomposition of the accessible Hilbert space into a sum of orthogonal subspaces  $\mathcal{H}_\nu$ ,

$$\mathcal{H}_E = \bigoplus_{\nu} \mathcal{H}_\nu, \quad (2.1)$$

where  $\nu = (\nu_1, \dots, \nu_J)$  defines a macrostate, and  $\mathcal{H}_\nu$  is the joint eigenspace of the  $\hat{M}_k$  with eigenvalues  $\nu_k$ . The  $\mathcal{H}_\nu$  will be referred to as macro-spaces, with  $|\mathcal{H}_\nu| = \dim \mathcal{H}_\nu$  the dimension of the corresponding macro-space. One then associates a Boltzmann entropy  $S_\nu = k_B \ln |\mathcal{H}_\nu|$  to each of the macro-spaces. Let us denote by  $\hat{P}_\nu$  the projector onto the space  $\mathcal{H}_\nu$ . Any microstate, which is a pure state  $|\Phi\rangle$ , is said to be in the macrostate  $\nu$  if  $|\Phi\rangle$  is almost in  $\mathcal{H}_\nu$ , i.e. if  $\langle \Phi | \hat{P}_\nu | \Phi \rangle \approx 1$ , and then its Boltzmann entropy is given by  $S_B(|\Phi\rangle) = S_\nu$ . It is expected for many systems, including the one we study here, that for appropriate physical macrovariables if the initial pure state  $|\Phi(0)\rangle$  is in a given macrostate, the time-evolved microstate  $|\Phi(t)\rangle$  will continue to be (at almost all times) in one single macrostate, i.e. Schrodinger cat-like states will not occur. The exception being when the system crosses from one macrostate to another.

As in the classical case, for a physical choice of the macrovariables, a particular macro-space has by far the largest dimension, which we refer to as the equilibrium macro-space and denote it by  $\mathcal{H}_{\text{eq}}$ . It is characterized by the fact  $|\mathcal{H}_{\text{eq}}| = (1 - \epsilon)|\mathcal{H}_E|$ ,  $\epsilon \ll 1$ , which we take as a physical requirement for any proper choice of the macrovariables. We also say that a system is in equilibrium when its microstate  $|\Phi\rangle$  is in, or almost in,  $\mathcal{H}_{\text{eq}}$ .

Now consider the unitary time-evolution of a system that is initially prepared in a non-equilibrium pure quantum state  $|\Phi(0)\rangle$ . Non-equilibrium means that  $|\Phi(0)\rangle$  is not in, or not almost in, the space  $\mathcal{H}_{\text{eq}}$ . It starts in one of the other macro-spaces  $\mathcal{H}_{\nu \neq \text{eq}}$  and with time it moves between different macro-spaces until it eventually ends up in the equilibrium macro-space and stays there for almost all subsequent times. It is expected that the non-equilibrium system should evolve to macro-spaces of higher dimensions, leading to a monotonic growth of entropy. This is what we would like to demonstrate in an explicit example. It is important to note that we are able to define this Boltzmann entropy for the pure quantum state,  $|\Phi(t)\rangle$ , at any time [14].

**Computing the Boltzmann entropy:** We note that the entropy  $S_\nu$  of the macrostate  $\nu$ , and thus  $S_B(|\Phi(t)\rangle)$  for  $|\Phi(t)\rangle$  in  $\mathcal{H}_\nu$ , is equal to the Gibbs-von Neumann entropy of a

generalized microcanonical ensemble, which is a mixed state that is uniform over (the unit sphere of)  $\mathcal{H}_\nu$ . It is important to stress, however, that this generalized microcanonical ensemble is not what we take as an accurate microscopic description of the microstate; it is only being used as a construction to compute the Boltzmann entropy of the microstate  $|\Phi(t)\rangle$  at time  $t$ . The Boltzmann entropy at a later time  $t' > t$  is dictated by what macrostate the unitarily time-evolved microstate  $|\Phi(t')\rangle$  at that time corresponds to. If we were to instead unitarily time-evolve the density matrix of this out-of-equilibrium generalized microcanonical ensemble, its Gibbs-von Neumann entropy would not change in contrast to the second law of thermodynamics. A typical out-of-equilibrium microstate will, as time advances, typically move to other macrostates of higher Boltzmann entropy, so the Boltzmann entropy thereby does obey the second law for almost all microstates. The macrostate does not time-evolve unitarily, due to it being constructed via a coarse-graining with suitably chosen macrovariables.

This generalized microcanonical ensemble that is used to calculate the Boltzmann entropy of the macrostate at time  $t$  may be replaced by an equilibrium ensemble for a fictitious system where constraints have been imposed on all macrovariables to have particular values  $\nu$ . Then, since that is a macroscopic equilibrium system, the extensive part of its microcanonical entropy should be equal to the extensive part of the Gibbs-von Neumann entropy of an equivalent generalized canonical ensemble. This shows that we can arrive at a correct (to leading order) count of the number of independent microstates in  $\mathcal{H}_\nu$  by calculating the Gibbs-von Neumann entropy of an equivalent generalized canonical ensemble. This is convenient because in many cases, calculating properties is simpler in the canonical ensemble than in the microcanonical ensemble.

If we accept, as is argued above, that the Boltzmann entropy of the microstate  $|\Phi(t)\rangle$  of a macroscopic system is equal, to leading order in system size, to the Gibbs-von Neumann entropy of a properly chosen generalized canonical ensemble, this allows us to skip the step of defining the generalized microcanonical ensemble. We use the expectation values,  $\langle \hat{M}_k \rangle = \langle \Phi(t) | \hat{M}_k | \Phi(t) \rangle$ ,  $k = 1, \dots, J$ , to define the “equivalent” generalized canonical

(GC) ensemble as

$$\hat{\rho}_{\text{GC}} = \frac{e^{-\sum_k \lambda_k \hat{M}_k}}{Z_{\text{GC}}}, \quad (2.2)$$

$$\text{where } Z_{\text{GC}} = \text{Tr} \left[ e^{-\sum_k \lambda_k \hat{M}_k} \right], \quad (2.3)$$

and the Lagrange multipliers  $\lambda_k$  are obtained from the constraint equations

$$\text{Tr}[\hat{M}_k \hat{\rho}_{\text{GC}}] = \langle \hat{M}_k \rangle, \quad k = 1, \dots, J. \quad (2.4)$$

The resulting Boltzmann entropy  $S_B$  for the microstate  $|\Phi(t)\rangle$  and the choice of  $\{\hat{M}_k\}$  is then given by

$$S_B = k_B \sum_k \lambda_k \langle \hat{M}_k \rangle + k_B \ln Z_{\text{GC}}. \quad (2.5)$$

We note that this is also equal to the maximum value of the Gibbs-von Neumann entropy

$$S_{\text{GvN}} = -k_B \text{Tr}[\hat{\rho}_N \ln \hat{\rho}_N] \quad (2.6)$$

over all  $\hat{\rho}_N$ , subject to the constraints  $\text{Tr}[\hat{M}_k \hat{\rho}_N] = \langle \hat{M}_k \rangle$  [72].

Using this generalized canonical approach to compute the Boltzmann entropy permits more flexibility in the choice of macrovariables, as compared to those that adhere to the conditions needed for the above construction of generalized microcanonical macrostates. In particular, the spectra of the operators  $\{\hat{M}_k\}$  need not be coarse-grained, and for quantum systems, these operators need not commute and may be microscopic operators, as we demonstrate in the example below.

## 2.2 An illustrative example: a one-dimensional quantum ideal gas

In this work, we consider a quantum ideal gas of  $N$  particles on a circle of length  $L$ . We examine the Boltzmann entropy for two different choices of macrovariables, schematically

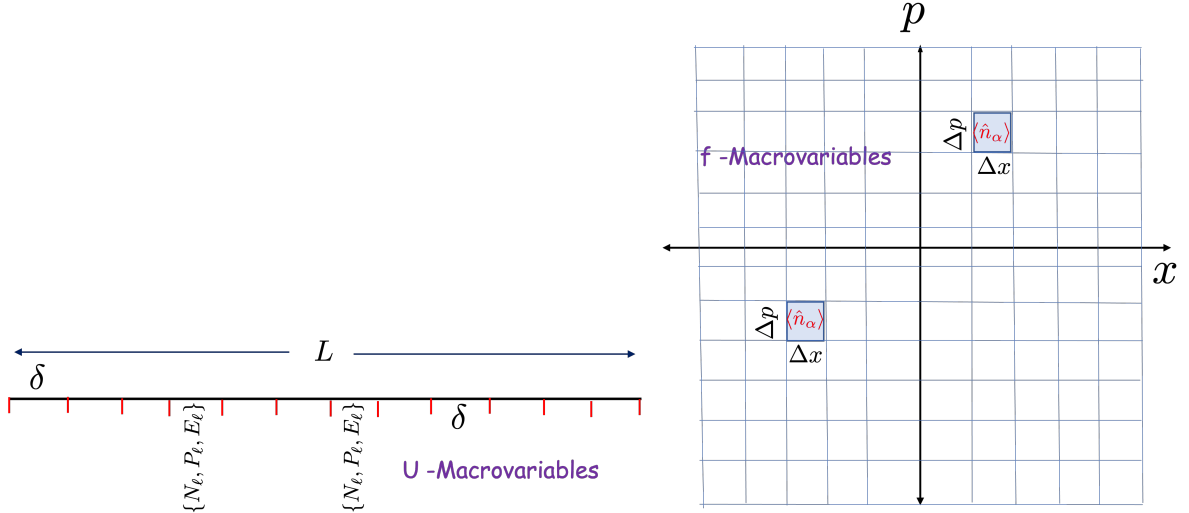


Figure 2.1: Schematic of the macrovariables that we consider. (Left panel)  $U$ -macrovariables in which, the box of length  $L$  is divided into cells of length  $\delta$ . By  $U$ -macrovariables, we mean coarse-grained particle number, momentum, and energy within each cell. (Right panel)  $f$ -macrovariables in which the macrovariables are defined by coarse-graining in the single-particle phase space. By  $f$ -macrovariables we mean coarse-grained particle numbers within each box of area  $\Delta x \Delta p$ . A macrostate corresponds to a specification of the values of the macrovariables.

described in Fig. (2.1), that are quantum analogs of those used for the classical ideal gas in Ref. [19]:

1.  $U$ -macrovariables: These are specified by the three conserved fields of particle number, momentum, and energy and are direct analogs of the corresponding classical macrovariables [19]. They correspond to the usual fields that are used in the hydrodynamic description of interacting systems — our non-interacting system has further conserved quantities but we can choose to consider the coarse-grained description in terms of these fields alone. More specifically, we divide our system of length  $L$  into  $A$  spatial cells of size  $\delta = L/A$ . We consider a set of operators  $\{\hat{N}_\ell, \hat{P}_\ell, \hat{E}_\ell\}$ ,  $\ell = 1, 2 \dots A$ , corresponding to the total number of particles, the total momentum, and the total energy in the  $\ell^{\text{th}}$  cell. The precise definitions of these operators are given in Sec. (2.4.1). Given that the system is in a microstate  $|\Phi(t)\rangle$ , let  $\langle \hat{B} \rangle = \langle \Phi | \hat{B} | \Phi \rangle$  denote the expectation value of any operator  $\hat{B}$ . Then, the set of expectation values  $\{N_\ell, P_\ell, E_\ell\} = \{\langle \hat{N}_\ell \rangle, \langle \hat{P}_\ell \rangle, \langle \hat{E}_\ell \rangle\}$  specify, as we argued in the preceding paragraphs, the  $U$ -macrostate.

2.  $f$ -macrovariables: For the classical gas, the  $f$ -macrovariables are the distribution  $f(x, p)$  of the single-particle positions and momenta [19]. Here we do not use a direct quantum analog of the classical macrovariables, but instead use a more microscopic choice, which is permitted for the quantum gas: We choose a complete and orthonormal basis of single-particle wavefunctions, each of which is approximately localized in position space within a width  $\Delta x$  and in momentum space with width  $\Delta p$ . Such states will necessarily have to satisfy the uncertainty relation  $\Delta x \Delta p \gtrsim \hbar$ . As we will show in Sec. (2.4.2), it is possible to construct such an orthonormal basis set on the circle with states that are approximately localized in position space with  $\Delta x = L/K$  and in momentum space with  $\Delta p = 2\pi\hbar K/L$ , where  $K$  is an integer. We denote these single-particle basis states by  $|\psi_\alpha\rangle$  with  $\alpha \equiv (r, v)$ , where  $r = 1, \dots, K$  and  $v = \vartheta K$  where  $\vartheta \in \mathbb{Z}$ . These states are localized around  $x = r\Delta x$  and  $p = \vartheta\Delta p$ . Let  $\hat{n}_\alpha$  be the number operator corresponding to the occupation of the state  $|\psi_\alpha\rangle$ . The commuting operators  $\{\hat{n}_\alpha\}$  form a set of *microvariables*, since specifying all of their eigenvalues specifies the microstate completely.

To define macrovariables for the quantum gas, we consider the expectation values  $\{D_\alpha = \langle \hat{n}_\alpha \rangle\}$  in the microstate  $|\Phi\rangle$ . Since a pure state wavefunction of a quantum system implies a probabilistic description, specifying only the  $\{D_\alpha\}$  implies a coarse-graining, in the sense that they do not specify the microstate. In fact, these expectation values  $\{D_\alpha\}$  constitute a good set of macrovariables that can be used to define a corresponding generalized canonical ensemble and Boltzmann entropy, following the procedure outlined above. The resulting Boltzmann entropy is

$$S_B^f = \sum_\alpha [-D_\alpha \ln D_\alpha \mp (1 \mp D_\alpha) \ln(1 \mp D_\alpha)], \quad (2.7)$$

where the negative and positive signs in the  $\mp$  are for fermions and bosons, respectively. This entropy can also be described from a generalized *grand* canonical ensemble, where each of the single-particle states  $\alpha$  has its own chemical potential  $\mu_\alpha$  in order to set  $D_\alpha$ . For the classical gas, the cells  $\Delta x \Delta p$  used to define the  $f$ -macrovariables must be large enough so that they are typically occupied by many particles, in order to have enough coarse-graining [19]. For the quantum gas, on the

other hand, fully microscopic cells may be used, and the needed coarse-graining is provided by using the expectation values as the macrovariables.

## 2.3 Microscopic model and dynamical evolution

Our system is a quantum ideal gas of  $N$  particles on a circle of length  $L$ . The microstate of the system is a pure state  $|\Phi(t)\rangle$  or, using the position representation, the wavefunction  $\Phi(x_1, x_2, \dots, x_N, t)$ . This state evolves in time via the Schrödinger equation  $i\hbar\partial_t\Phi = \hat{H}\Phi$  with the free circle Hamiltonian  $\hat{H} = -[\hbar^2/(2m)]\sum_{\ell=1}^N\partial_{x_\ell}^2$ . The gas is initially confined to a part of the circle, of length  $aL$  with  $0 < a < 1$  (usually  $a = 1/2$ ), which we refer to as a “box”. The initial  $N$ -particle state  $|\Phi(0)\rangle$  may be taken to be an eigenstate of the occupations of the single-particle energy eigenstates in the box. We also compare our results to the initial grand canonical mixed states in the box. At  $t = 0$ , the box walls are removed at both ends and the gas is allowed to freely expand on the full circle. As the gas expands, we are interested in the time evolution of the macrovariables  $U$  and  $f$  and of the corresponding entropies.

The single-particle energy eigenstates and eigenvalues on the circle are given by

$$\varphi_n(x) = \frac{1}{\sqrt{L}}e^{2\pi inx/L} \text{ for } x \in [0, L), \quad (2.8)$$

$$\epsilon_n = \frac{1}{2m} \left( \frac{2\pi n\hbar}{L} \right)^2, \quad (2.9)$$

where  $n$  runs over all integers. These are also momentum eigenstates with eigenvalues  $p_n = 2\pi n\hbar/L$ . A complete  $N$  particle basis of Fock states is specified by the occupations  $\{|N_n\rangle\}$  with  $N_n \in \{0, 1\}$  for fermions and  $N_n \in \{0, 1, \dots, \infty\}$  for bosons, constrained so that  $\sum_n N_n = N$ . We will find it useful sometimes to use the language of second quantization and so we define the particle creation and annihilation operators  $\hat{\Psi}^\dagger(x), \hat{\Psi}(x)$  which create or annihilate, respectively, a particle at position  $x$ . For fermions, they satisfy the anti-commutation relation  $\{\hat{\Psi}(x), \hat{\Psi}^\dagger(x')\} = \delta(x - x')$ , while for bosons they satisfy the commutation relation  $[\hat{\Psi}(x), \hat{\Psi}^\dagger(x')] = \delta(x - x')$ . We also define the creation and annihilation operators  $\hat{b}_n^\dagger, \hat{b}_n$ , corresponding to the single-particle energy eigenstate  $\varphi_n$ . These are related to the position operators as  $\hat{\Psi}(x) = \sum_n \hat{b}_n \varphi_n(x)$ . In the Heisenberg

representation, these operators have simple time evolution for our noninteracting gas

$$\hat{b}_n(t) = e^{-i\epsilon_n t/\hbar} \hat{b}_n(0). \quad (2.10)$$

As we will see in the subsequent sections, for our purposes, it suffices to study the single-particle density matrix and the corresponding Wigner function. Therefore, in the following subsections, we discuss the evolution of the density matrix and the Wigner function.

### 2.3.1 Density matrix

For our analysis of the dynamics, we will use the single-particle density operator  $\hat{\rho}_1$ . In the Heisenberg picture, and in the basis of the single-particle energy eigenstates,  $\hat{\rho}_1$  is a matrix of operators, with operator-valued matrix elements

$$\hat{\rho}_{1,mn}(t) \equiv \hat{\rho}_1(p_m, p_n, t) = \hat{b}_n^\dagger(t) \hat{b}_m(t). \quad (2.11)$$

Note that this is normalized so  $\sum_n \hat{\rho}_{1,nm}(t) = \hat{N}$  is the operator for the total particle number. In the position basis, the matrix elements of  $\hat{\rho}_1(t)$  are given by

$$\begin{aligned} \rho_1(x, x', t) &\equiv \langle x | \hat{\rho}_1(t) | x' \rangle = N \int dx_2 dx_3 \dots dx_N \\ &\Phi^*(x', x_2, x_3, \dots x_N, t) \Phi(x, x_2, x_3, \dots x_N, t) \\ &= \text{Tr} \left[ \hat{\Psi}^\dagger(x') \hat{\Psi}(x) \hat{\rho}_N(t) \right], \end{aligned} \quad (2.12)$$

where  $\hat{\rho}_N(t)$  is the many-particle density matrix. For this given many-particle state  $\hat{\rho}_N$ , the single-particle density matrix is the matrix of expectation values of the single-particle density operator, which in the single-particle momentum eigenbasis we write as

$$\begin{aligned} \tilde{\rho}_1(p_m, p_n, t) &\equiv \text{Tr} \left[ \hat{b}_n^\dagger(t) \hat{b}_m(t) \hat{\rho}_N \right] \\ &\equiv \left\langle \hat{b}_n^\dagger(t) \hat{b}_m(t) \right\rangle = e^{-i(\epsilon_m - \epsilon_n)t/\hbar} \tilde{\rho}_1(p_m, p_n, 0). \end{aligned} \quad (2.13)$$

Thus we can compute the evolution of  $\hat{\rho}_1$  once we know the initial value,  $\tilde{\rho}_1(p_m, p_n, 0)$ , which we now evaluate.

For the description of the initial state where the gas is confined to a box of length  $aL$ , we will need the following single-particle ‘‘box’’ energy eigenspectrum

$$\chi_s(x) = \sqrt{\frac{2}{aL}} \sin \frac{s\pi x}{aL} \text{ for } x \in [0, aL], \quad (2.14)$$

$$e_s = \frac{\pi^2 \hbar^2 s^2}{2ma^2 L^2}, \quad (2.15)$$

where  $s$  runs over all positive integers. The box and circle states are related by the transformation

$$\chi_s(x) = \sum_{n=-\infty}^{\infty} V_{sn} \varphi_n(x), \quad (2.16a)$$

$$\begin{aligned} V_{sn} &= \int_0^{aL} \chi_s(x) \varphi_n^*(x) dx \\ &= \frac{\sqrt{2}as}{\pi(4a^2n^2 - s^2)} [e^{-2\pi ina} \cos s\pi - 1]. \end{aligned} \quad (2.16b)$$

Note that since  $\{\chi_s(x), s = 1, \dots, \infty\}$  do not form a complete set for states on the circle,  $V$  is not an invertible matrix.

As mentioned before, we are interested in the evolution of an  $N$  particle Fock state with energy  $E$ . For large  $N$  and  $E$ , it is equivalent and more convenient to work with a grand-canonical distribution with  $\beta$  and  $\mu$  chosen according to

$$N = \sum_{s=1}^{\infty} f(e_s, \beta, \mu), \quad (2.17a)$$

$$E = \sum_{s=1}^{\infty} f(e_s, \beta, \mu) e_s, \quad (2.17b)$$

where  $f(e, \beta, \mu) = \frac{1}{e^{\beta(e-\mu)} \pm 1}$  is the Fermi (+) /Bose (-) function.

In our numerical implementation, we use the following protocol. We prepare the

system in a pure state with the single-particle density matrix given by

$$\hat{\rho}_1^{\text{P}}(0) = \sum_{s=1}^{\infty} n_s |\chi_s\rangle\langle\chi_s|, \quad (2.18)$$

where the superscript ‘‘P’’ in Eq. (2.18) denotes pure state and the set  $\{n_s\}$  is chosen from the grand-canonical distribution

$$P(\{n_s\}) = \frac{1}{Z} e^{-\beta \sum_s (e_s - \mu) n_s}, \quad (2.19)$$

$$Z = \prod_s [1 \pm e^{-\beta(e_s - \mu)}]^{\pm 1}, \quad (2.20)$$

subject to the constraints  $\sum_s n_s = N$  and  $\sum_s n_s e_s = E$ . Here  $n_s \in \{0, 1\}$  for fermions (+) and  $n_s \in \{0, 1, \dots, \infty\}$  for bosons (-). In practice, these constraints are difficult to satisfy exactly. Hence we chose the set  $\{n_s\}$  such that these constraints are satisfied within some desired tolerance. We compare our results for the pure initial state with the mixed (thermal) state described by the single-particle density matrix

$$\hat{\rho}_1^{\text{M}}(0) = \sum_{s=1}^{\infty} f(e_s, \beta, \mu) |\chi_s\rangle\langle\chi_s|, \quad (2.21)$$

where the superscript ‘‘M’’ in Eq. (2.21) denotes mixed thermal state. Using the box-to-circle transformation in Eq. (2.16a), we can write the density matrix in Eq. (2.21) in terms of the circle eigenfunctions to give

$$\tilde{\rho}_1^{\text{M}}(p_m, p_n, 0) = \sum_{s=1}^{\infty} f(e_s, \beta, \mu) V_{sm} V_{sn}^*. \quad (2.22)$$

Using Eq. (2.13), the evolution of the density matrix in Eq. (2.22) is thus given by:

$$\hat{\rho}_1^{\text{M}}(t) = \sum_{s=1}^{\infty} f(e_s, \beta, \mu) \sum_{m, n=-\infty}^{\infty} V_{sm} V_{sn}^* e^{-i(\epsilon_m - \epsilon_n)t/\hbar} |\varphi_m\rangle\langle\varphi_n|. \quad (2.23)$$

The pure state density matrix  $\hat{\rho}_1^{\text{P}}$  has a similar representation with  $f(e_s, \beta, \mu)$  replaced by  $n_s$  in Eqs. (2.22) and (2.23). Note that the normalization condition  $\text{Tr} \hat{\rho}_1(t) = N$  implies  $(VV^\dagger)_{ss} = 1$ . The density matrix in Eq. (2.23) and the corresponding representation of

$\hat{\rho}_1^P(t)$  are used to calculate local densities corresponding to conserved quantities.

### 2.3.2 Wigner distribution function

The Wigner distribution function (WDF) was introduced by Wigner [73,74] as a quantum analog of the phase space distribution in classical systems. In 1-d, on the infinite line, the WDF, denoted by  $w(x, p, t)$ , is defined as

$$w(x, p, t) = \frac{1}{2\pi\hbar} \int_{-\infty}^{\infty} dy \rho_1 \left( x + \frac{y}{2}, x - \frac{y}{2}, t \right) e^{ipy/\hbar}. \quad (2.24)$$

We point out that the above transformation is one-to-one, thus the WDF and the density matrix contain the same information. For noninteracting systems in the absence of external potentials,  $w(x, p, t)$  satisfies the simple equation

$$\partial_t w(x, p, t) + \frac{p}{m} \partial_x w(x, p, t) = 0, \quad (2.25)$$

which is identical to the evolution equation of the single-particle phase space density in classical non-interacting systems. The solution of Eq. (2.25) is simply given by boosting the initial profile

$$w(x, p, t) = w \left( x - \frac{pt}{m}, p, 0 \right). \quad (2.26)$$

In our model, the gas is confined to a circle of length  $L$  instead of the infinite line. Therefore, we have  $x \in [0, L)$  and the allowed momenta,  $p_n = 2\pi n\hbar/L$ , with integer  $n$ , are discrete. A natural extension of the definition in Eq. (2.24) to the case of circular coordinates would be to replace  $p$  by  $p_n$  and restrict the integral from 0 to  $L$  [75-77]. However, this extension does not satisfy Eq. (2.25) with  $p$  replaced by  $p_n$ . It turns out that a modified definition of the WDF on the circle, that obeys Eq. (2.25), can be obtained. For this one needs to define a new momentum variable:

$$q_n = \frac{\pi n\hbar}{L} = \frac{p_n}{2}, \quad (2.27)$$

that takes both integer as well as half-integer values. The modified WDF on the circle is thus defined as

$$w(x, q_n, t) = \frac{1}{2L} \int_{-L}^L dy \rho_1 \left( x + \frac{y}{2}, x - \frac{y}{2}, t \right) e^{iq_n y/\hbar}, \quad (2.28)$$

$$= \frac{1}{L} \sum_{m=-\infty}^{\infty} \tilde{\rho}_1 \left( q_n + \frac{p_m}{2}, q_n - \frac{p_m}{2}, t \right) e^{ip_m x/\hbar}, \quad (2.29)$$

where, in Eq. (2.29), the sum is over even values of  $m$  if  $q_n$  is an integer and odd values of  $m$  if  $q_n$  is a half-integer. The inverse transform is given by

$$\tilde{\rho}_1(p_m, p_n, t) = \int_0^L dx w \left( x, \frac{p_m + p_n}{2}, t \right) e^{-i(p_m - p_n)x/\hbar}. \quad (2.30)$$

It is easy to check that the Wigner function in Eq. (2.28) satisfies Eq. (2.25) on the circle with  $p$  replaced by  $q_n$  and thus has a solution of the form in Eq. (2.26) with periodicity  $L$ . Using Eq. (2.23) in Eq. (2.29), we get

$$\begin{aligned} w(x, q_n, t) &= \sum_{s=1}^{\infty} f(e_s, \beta, \mu) \sum_{\ell, m=-\infty}^{\infty} V_{s\ell} V_{sm}^* \varphi_{\ell}(x) \varphi_m^*(x) \\ &\times e^{-i(\epsilon_{\ell} - \epsilon_m)t/\hbar} \delta(\ell + m - n), \end{aligned} \quad (2.31)$$

for the mixed state and a similar expression for the pure state with  $f(e_s, \beta, \mu)$  replaced by  $n_s$ . As we shall see in the next section, the WDF provides a simple way to define particle, momentum, and energy densities which are needed for defining the  $U$ -macrostate.

## 2.4 Choices of macrostates and the corresponding entropies

### 2.4.1 $U$ -macrostate and $S_B^U$

In this section, we present the details of the construction of the  $U$ -macrostate. In this description, the observables that define the system's macrostate are the expectation values

of the three conserved macroscopic fields, namely the particle, momentum, and energy densities. We first motivate the basic definition of the operators corresponding to these observables and then show that their expectation values can be written in a simple and physically intuitive form in terms of the WDF. We then discuss the corresponding entropy  $S_B^U$ .

Using second quantized notation, the operators corresponding to the total number of particles, total momentum, and total energy on the circle, in units of  $\hbar = m = 1$ , are given by

$$\hat{N} = \int_0^L dx \hat{\Psi}^\dagger(x, t) \hat{\Psi}(x, t), \quad (2.32a)$$

$$\hat{P} = -i \int_0^L dx \hat{\Psi}^\dagger(x, t) \partial_x \hat{\Psi}(x, t), \quad (2.32b)$$

$$\hat{E} = -\frac{1}{2} \int_0^L dx \hat{\Psi}^\dagger(x, t) \partial_x^2 \hat{\Psi}(x, t). \quad (2.32c)$$

It is then natural to define the following local density operators for the three fields:

$$\hat{n}(x, t) = \hat{\Psi}^\dagger(x, t) \hat{\Psi}(x, t), \quad (2.33a)$$

$$\hat{p}(x, t) = \frac{i}{2} \left[ (\partial_x \hat{\Psi}^\dagger(x, t)) \hat{\Psi}(x, t) - \hat{\Psi}^\dagger(x, t) \partial_x \hat{\Psi}(x, t) \right], \quad (2.33b)$$

$$\begin{aligned} \hat{e}(x, t) = & -\frac{1}{8} \left[ \hat{\Psi}^\dagger(x, t) \partial_x^2 \hat{\Psi}(x, t) + (\partial_x^2 \hat{\Psi}^\dagger(x, t)) \hat{\Psi}(x, t) \right. \\ & \left. - 2(\partial_x \hat{\Psi}^\dagger(x, t)) (\partial_x \hat{\Psi}(x, t)) \right]. \end{aligned} \quad (2.33c)$$

Note that hermitising, as done here, only produces corrections that are spatial derivatives and therefore, does not change the total quantities. Though our choices of the expressions for the densities are not unique, they are motivated by the simple forms they take when we write their expectation values in terms of the WDF. To define our coarse-grained macrovariables, we divide the circle into  $A$  cells of size  $\delta = L/A$  and label them by the index  $\ell = 1, 2, \dots, A$  with the  $\ell^{\text{th}}$  cell beginning at  $x = (\ell - 1)\delta$ . Our macrovariables are

then the set of operators

$$\{\hat{N}_\ell, \hat{P}_\ell, \hat{E}_\ell\} = \int_{(\ell-1)\delta}^{\ell\delta} dx \{\hat{n}(x), \hat{p}(x), \hat{e}(x)\}. \quad (2.34)$$

To find the values of the macrovariables for a given microstate, we need the expectation values of the above operators. We find that the expectation values for the densities take the following simple forms when written in terms of the WDF:

$$n(x, t) = \sum_{n=-\infty}^{\infty} w(x, q_n, t), \quad (2.35a)$$

$$p(x, t) = \sum_{n=-\infty}^{\infty} q_n w(x, q_n, t), \quad (2.35b)$$

$$e(x, t) = \sum_{n=-\infty}^{\infty} (q_n^2/2) w(x, q_n, t). \quad (2.35c)$$

As is clear from the above equations, the densities take a physically intuitive form as the marginals of the Wigner function. The expectation values of the macrovariables in Eq. (2.34) are denoted by  $\{N_\ell, P_\ell, E_\ell\}$  and are readily obtained by integrating Eq. (2.35) across cells.

**Entropy of the  $U$ -macrostate:** We now return to our goal of defining the entropy for the  $U$ -macrostate. Given the set  $\{N_\ell, P_\ell, E_\ell\}$ ,  $\ell = 1, 2, \dots, A$ , we need to find the number of microstates consistent with a given specification for the values of the set. Assuming small correlations between cells, the number of microstates with these constraints is simply the product of the number of possible microstates in each cell (with the local constraints). Hence we get the entropy

$$S_B^U = \sum_{\ell=1}^A S(N_\ell, P_\ell, E_\ell), \quad (2.36)$$

where  $S(N_\ell, P_\ell, E_\ell)$  is the equilibrium entropy of the  $\ell^{\text{th}}$  cell of size  $\delta = L/A$  with the specified values of the conserved quantities  $N_\ell, P_\ell, E_\ell$ .

## 2.4.2 $f$ -macrostate and $S_B^f$

As discussed in Sec. (2.1) the construction of the  $f$ -macrostate requires us to find a basis set of single particle wavefunctions that are localized both in position and momentum space. We now discuss its construction. The  $\varphi$ -basis, defined in Eq. (2.8), consists of momentum eigenstates on the circle that are completely delocalized in position space. To construct our localized basis, we superimpose  $K$  number of successive  $\varphi$ -states labelled by a central momentum  $p = 2\pi\hbar v/L$ , and generate  $K$  new states

$$|\psi_\alpha\rangle \equiv |r, v\rangle = \frac{1}{\sqrt{K}} \sum_{n \in \mathcal{R}_v} |\varphi_n\rangle e^{-in\frac{2\pi r}{K}}, \quad (2.37)$$

where  $\mathcal{R}_v = \{v - (K - 1)/2, \dots, v + (K - 1)/2\}$  and  $\alpha \equiv (r, v)$  is a collective index for the basis states. Note that  $r = 1, \dots, K$  and  $v = \vartheta K$  where  $\vartheta$  takes all integer values. The  $K$  resulting  $|r, v\rangle$  states for a given  $v$  are localized around  $rL/K$ ,  $r = 1, \dots, K$  in the position space and around  $2\pi\hbar v/L$  in the momentum space. For this reason, we shall refer to the  $\psi$ -basis in Eq. (2.37) as the *wavepacket basis*.

We now define the *wavepacket density*, denoted by  $D_\alpha(t) = \langle \hat{n}_\alpha \rangle \equiv D(r, v, t)$ , as the diagonal of the single-particle density matrix  $\hat{\rho}_1(t)$  in the wavepacket basis

$$D_\alpha(t) \equiv D(r, v, t) = \langle r, v | \hat{\rho}_1(t) | r, v \rangle. \quad (2.38)$$

It turns out that one can write down the wavepacket density in terms of the Wigner function as

$$D(r, v, t) = \frac{1}{K} \sum_{\ell, m \in \mathcal{R}_v} \int_0^L dx w\left(x, \frac{\ell + m}{2}, t\right) e^{-2\pi i(\ell - m)z}, \quad (2.39)$$

where  $z = x/L - r/K$ . Making the variable transformation  $q = (\ell + m)/2$  and  $n = \ell - m$ , we can rewrite Eq. (2.39) as

$$D(r, v, t) = \frac{1}{K} \sum_{q=v_-}^{v_+} \int_0^L dx w(x, q, t) \sum_{n=2(q-v_+)}^{2(q-v_-)} e^{-2\pi i n z}, \quad (2.40)$$

where  $v_{\pm} = v \pm (K - 1)/2$ . Summing over  $n$  yields

$$D(r, v, t) = \frac{1}{K} \sum_{q=v_{-}}^{v_{+}} \int_0^L dx w(x, q, t) G_K(q - v, x), \quad (2.41)$$

$$G_K(q, x) = e^{-4\pi i q z} \frac{\sin(2K - 1)\pi z}{\sin \pi z}, \quad (2.42)$$

where recall  $z = x/L - r/K$ . Eq. (2.41) suggests that the wavepacket density is nothing but a coarse-grained WDF. It is also instructive to look at the marginals of the wavepacket density. The momentum marginal is given by the expression (see Appendix A.1)

$$D_v(v) = \sum_{r=1}^K D(r, v, t) = \sum_{n \in \mathcal{R}_v} \tilde{\rho}_1(p_n, p_n, 0), \quad (2.43)$$

where recall  $\mathcal{R}_v$  denotes set of momenta centered around  $v$ . Similarly, the position marginal is given by (see Appendix A.1)

$$D_r(r, t) = \sum_v D(r, v, t) = \int_0^L dx h_K \left( \frac{x}{L} - \frac{r}{K} \right) \rho_1(x, x, t), \quad (2.44)$$

$$\text{with } h_K(x) = \frac{1}{K^2} \left( \frac{\sin \pi K z}{\sin \pi z} \right)^2. \quad (2.45)$$

Note that Eqs. (2.43, 2.44) represent coarse-grained versions of the diagonal elements of the density matrix in the momentum and position basis.

**Entropy of the  $f$ -macrostate:** We now discuss the entropy formula in Eq. (2.7) for a given specification of the set  $\{D_{\alpha}\}$ . To derive this formula, one maximizes the Gibbs-von Neumann entropy,  $S_{\text{GvN}} = -\text{Tr}[\hat{\rho}_N \log \hat{\rho}_N]$ , subject to the constraint

$$D_{\alpha}(t) = \langle \psi_{\alpha} | \hat{\rho}_1(t) | \psi_{\alpha} \rangle = \text{Tr} \left[ \hat{\rho}_N(t) \hat{\Psi}_{\alpha}^{\dagger} \hat{\Psi}_{\alpha} \right], \quad (2.46)$$

where  $\hat{\Psi}_\alpha$  creates a particle in the state  $|\psi_\alpha\rangle$ . The density matrix  $\hat{\rho}_N^*$  that maximizes  $S_{\text{GvN}}$  is given by

$$\hat{\rho}_N^* = \frac{1}{Z} e^{-\sum_\alpha \lambda_\alpha \hat{\Psi}_\alpha^\dagger \hat{\Psi}_\alpha}, \quad (2.47)$$

$$Z = \prod_\alpha [1 \pm e^{-\lambda_\alpha}]^{\pm 1}, \quad (2.48)$$

where  $+$  is for fermions and  $-$  is for bosons. Note that the expression for the density matrix in Eq. (2.48) is correct even if the operators  $\{\hat{M}_k\}$  do not commute [see Appendix (A.2) for a detailed derivation]. Also note that it is precisely the density matrix that defines the equivalent generalized canonical ensemble  $\hat{\rho}_{GC}$ , as mentioned in Sec. (2.1). The Lagrange multipliers  $\lambda_\alpha$  are given by the relation

$$D_\alpha = \text{Tr}[\hat{\rho}_N^* \hat{\Psi}_\alpha^\dagger \hat{\Psi}_\alpha] = \frac{1}{e^{\lambda_\alpha} \pm 1}. \quad (2.49)$$

We can thus write down the maximal Gibbs-von Neumann entropy,  $S_B^f = -\text{Tr}[\hat{\rho}_N^* \log \hat{\rho}_N^*]$ , in terms of  $D_\alpha$  as

$$S_B^f = \sum_\alpha [-D_\alpha \ln D_\alpha \mp (1 \mp D_\alpha) \ln(1 \mp D_\alpha)], \quad (2.50)$$

where the  $-$  in the  $\mp$  is for fermions and the  $+$  is for bosons.

In order to compute the final change in entropy  $\Delta s_B^f = (S_B^f(\infty) - S_B^f(0))/N$ , we next provide analytical estimates for the values of  $D_\alpha(t)$  at  $t \rightarrow \infty$  and  $t = 0$ . Substituting the expression for  $\hat{\rho}_1(t)$  from Eq. (2.23) into Eq. (2.38), we obtain an explicit expression for the wavepacket density

$$D_\alpha(t) = \sum_{s=1}^{\infty} f(e_s, \beta, \mu) \sum_{m,n=-\infty}^{\infty} V_{sm} V_{sn}^* e^{-i(\epsilon_m - \epsilon_n)t/\hbar} \langle \psi_\alpha | \varphi_m \rangle \langle \varphi_n | \psi_\alpha \rangle. \quad (2.51)$$

We first discuss the late time limit. As  $t \rightarrow \infty$ , we only get contributions from the  $m = n$  terms in Eq. (2.51)

$$D_\alpha(\infty) = \sum_{s=1}^{\infty} f(e_s, \beta, \mu) \sum_{n=-\infty}^{\infty} |V_{sn}|^2 \|\langle \varphi_n | \psi_\alpha \rangle\|^2. \quad (2.52)$$

In the limit of large  $N$  and  $L$  (keeping  $N/L = \rho$  fixed), we use the explicit form of  $V_{sn}$  in Eq. (2.16b) and find that  $|V_{sn}|^2$  is highly peaked around  $s \approx 2an$  for large  $n$ . Hence the sum can be approximated as  $\sum_s f(e_s, \beta, \mu) |V_{sn}|^2 \approx f(e_{2an}, \beta, \mu) \sum_s |V_{sn}|^2 = af(\epsilon_n, \beta, \mu)$ . We thus get for the late time

$$D_\alpha(\infty) = \frac{a}{K} \sum_{n \in \mathcal{R}_v} f(\epsilon_n, \beta, \mu). \quad (2.53)$$

To compute  $D_\alpha(0)$  we start with the expression

$$D_\alpha(0) = \sum_{s=1}^{\infty} f(e_s, \beta, \mu) \sum_{m,n=-\infty}^{\infty} V_{sm} V_{sn}^* \langle \psi_\alpha | \varphi_m \rangle \langle \varphi_n | \psi_\alpha \rangle. \quad (2.54)$$

Using Eq. (2.16b) for  $V_{sm}$ , we obtain the following simplified form:

$$D_\alpha(0) = \frac{1}{K} \sum_{s=1}^{\infty} f(e_s, \beta, \mu) |g_v(s, r)|^2, \quad \text{where} \quad (2.55)$$

$$g_v(s, r) = \sqrt{\frac{2}{a}} \int_{-r/K}^{a-r/K} dz \sin \left[ \frac{s\pi}{a} \left( z + \frac{r}{K} \right) \right] e^{-2\pi i v z} \frac{\sin \pi K z}{\sin \pi z}. \quad (2.56)$$

Since the integrand in  $g_v(s, r)$  is highly peaked about  $z = 0$  for large  $K$ , we make the replacement  $\sin(\pi z) \approx \pi z$  in the numerator whenever  $z = 0$  falls inside the integration limit *i.e.* for  $r < Ka$ . This allows us to make the following approximation  $g_v(s, r) \approx \Theta(Ka - r) \tilde{g}_v(s, r)$  where  $\Theta(r)$  is the Heaviside Theta function and  $\tilde{g}_v(s, r)$  is given by

$$\tilde{g}_v(s, r) \approx \sqrt{\frac{2}{a}} \int_{-\infty}^{\infty} dz \sin \left[ \frac{s\pi}{a} \left( z + \frac{r}{K} \right) \right] e^{-2\pi i v z} \frac{\sin \pi K z}{\pi z}. \quad (2.57)$$

This finally implies

$$|\tilde{g}_v(s, r)|^2 \approx \frac{1}{2a} \Theta(s_+ - s) \Theta(s - s_-), \quad (2.58)$$

with  $s_\pm = 2av \pm Ka$ . Using this approximation in Eq. (2.55), we get

$$D_\alpha(0) \approx \frac{1}{2aK} \sum_{s=s_-}^{s_+} f(e_s, \beta, \mu) \Theta(r < Ka). \quad (2.59)$$

Note that while making the above approximations, we have ignored possible  $r$  dependence near the edges of the initial box of size  $aL$ . As a result, the approximated density  $D_\alpha(0)$  slightly underestimates the initial entropy.

Using  $D_\alpha(\infty)$  from Eq. (2.53) and  $D_\alpha(0)$  from Eq. (2.59), in Eq. (2.50) one can numerically compute  $\Delta s_B^f$  for different  $T$  and  $\mu$ . However the above procedure does not remain valid for bosons at very low temperatures because the particles occupy only a few low-lying energy states and consequently they do not relax. On the other hand for fermions, the above procedure works for all  $T$ , and specifically at  $T = 0$ , one can obtain an explicit expression of  $\Delta s_B^f$ . To obtain this expression we first note that for  $T = 0$ , Eq. (2.53) gives  $D_\alpha(\infty) = a$  for all  $\alpha$  except those which are very close to the Fermi surface. Using  $D_\alpha(\infty) \approx a$  in Eq. (2.50), we find

$$S_B^f(\infty) = - \sum_{\alpha} [a \ln a + (1 - a) \ln(1 - a)], \quad (2.60)$$

where the summation extends over  $2n_{max}$  terms such that  $\epsilon_{n_{max}} = \mu$ . Given that  $e_s = \epsilon_{s/2a}$  and  $e_N = \mu$ , we get  $n_{max} = N/2a$ . The number of terms in the  $\alpha$ -sum is thus  $N/a$  and hence, the late time entropy per particle is given by

$$s_B^f(\infty) = -\frac{1}{a} [a \ln a + (1 - a) \ln(1 - a)]. \quad (2.61)$$

For  $a = 1/2$ , we obtain  $s_B^f(\infty) = 2 \ln 2$ . The initial density in Eq. (2.59) simplifies in a similar manner and we get

$$D_\alpha(0) = \frac{1}{2aK} \sum_{s=s_-}^{s_+} \Theta(e_s < \mu) \approx 1, \quad (2.62)$$

which results in the initial entropy at  $T = 0$  being zero (neglecting edge contributions as mentioned earlier). We therefore get  $\Delta s_B^f(T = 0) = 2 \ln 2$  for the Fermi gas expanding to twice the initial volume.

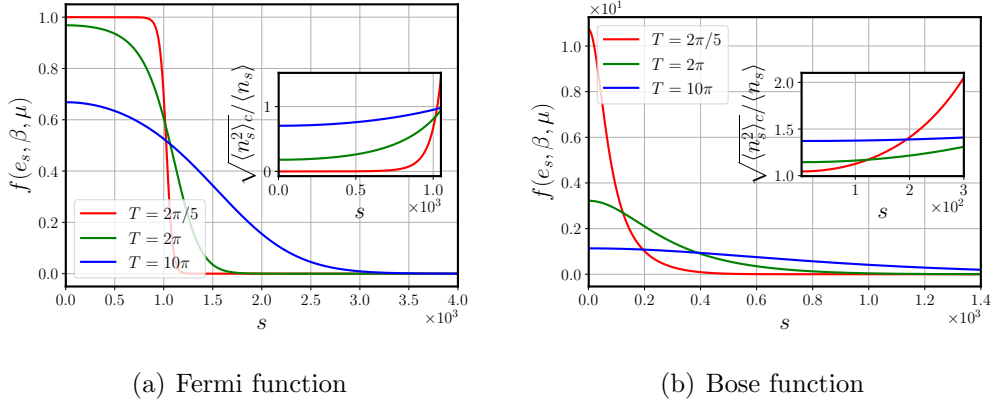


Figure 2.2: Fermi and Bose distribution functions showing the mean occupation numbers of energy levels at the low and high temperatures (along with an intermediate temperature for comparison) used in our numerical study. The particle density was set to  $\rho = 1$ . The insets show the relative number fluctuations.

## 2.5 Numerical results

In this section, we present the results of the evolution of the two macrovariables  $f$  and  $U$ , and the corresponding entropies for fermions in Sec. (2.5.1) and for bosons in Sec. (2.5.2).

The equilibrium state of an ideal gas is described by its temperature  $T$  and density  $\rho = N/L$ . For a quantum system, a relevant parameter that tells us whether we are in the quantum or classical regime is the ratio of the interparticle distance  $1/\rho$  to the thermal de Broglie wavelength,  $\lambda_{\text{th}} = h/(2\pi mk_B T)^{1/2}$ . With our choice of units with  $m = k_B = \hbar = 1$  and density fixed at  $\rho = 1$ , we take the square of this ratio,  $(\lambda_{\text{th}}\rho)^{-2} = T/(2\pi)$  to be the controlling parameter. In the following, we will present results for two sets of parameters: (i) low-temperature highly quantum regime  $T = 2\pi/5$ ; (ii) high-temperature regime  $T = 10\pi$ . In Fig. (2.2) we show the mean energy-level occupation number and their fluctuations for fermions and bosons at different temperatures.

We recall the two different initial conditions [see Sec. (2.3.1)] for which we present our results.

1. We consider the initial state to be a single pure many-body Fock state given by the box eigenstate:

$$|\Phi\rangle = |\{n_s\}\rangle, \quad (2.63)$$

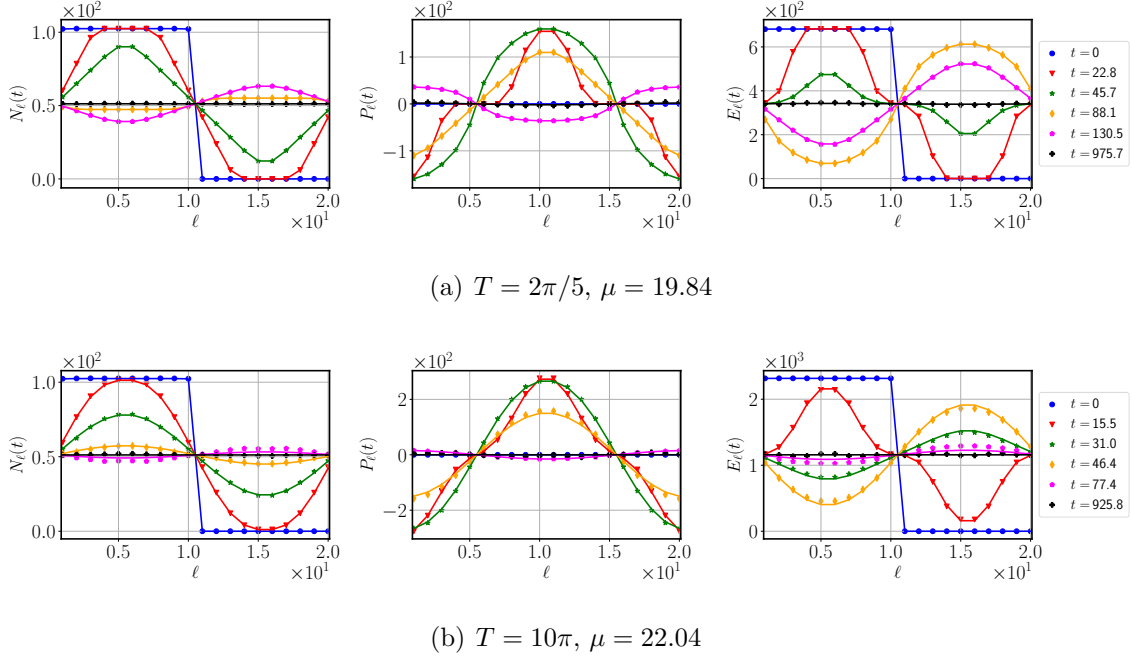


Figure 2.3: **Fermions - evolution of  $U$ -macrovariables**: Plots showing the spatial profiles of the number of particles, the total momentum, and the total energy in each of the  $A = 20$  cells for  $N = L = 1024$  at different times. The dots represent results for the pure state initial condition while the solid lines correspond to a thermal mixed state. Results are presented for two different temperatures  $T = 2\pi/5$ ,  $10\pi$  (top and bottom row respectively), and chemical potentials are fixed so that the mean density is set at  $\rho = 1$ . We see a good agreement between the pure state and the thermal state results.

where the single-particle level box occupancies,  $\{n_s\}$ , are chosen with probabilities given by the grand-canonical distribution [in the box  $x \in (0, L/2)$ ] with  $T$ ,  $\mu$  fixed at the desired values corresponding to our specified initial  $T$ ,  $\rho$ . We sample only one initial state this way; for large  $N$ , this comes close to “self-averaging”.

2. We consider an initial state whose one-particle density matrix is identical to that of the grand-canonical distribution in the box.

### 2.5.1 Fermions

In this section, we present results for fermions first for the  $U$ -macrovariable and then for the  $f$ -macrovariable.

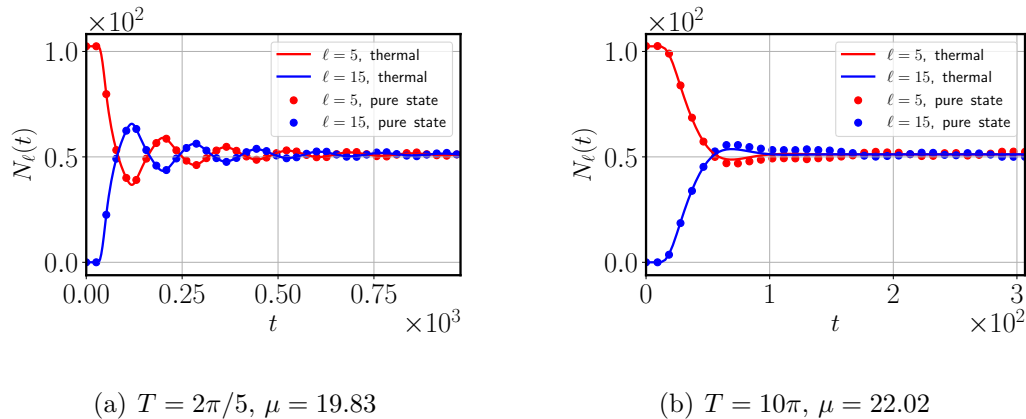
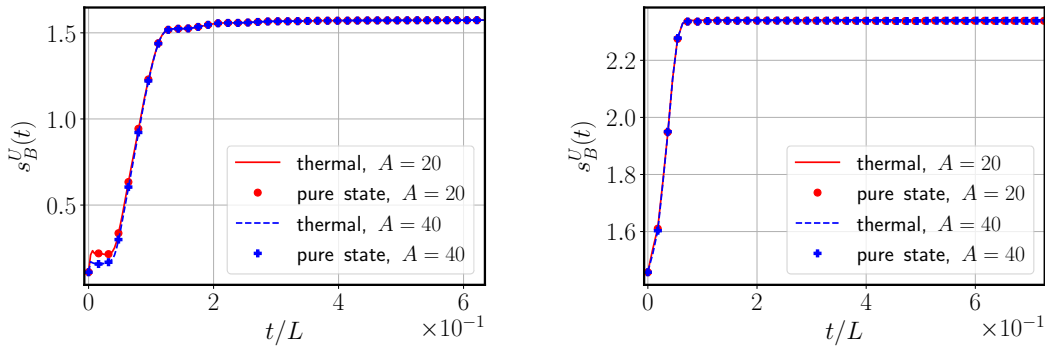


Figure 2.4: **Fermions:** Time evolution of the number of particles inside the 5<sup>th</sup> and 15<sup>th</sup> cells out of a total of  $A = 20$  cells for  $N = L = 1024$ . As in Fig. (2.3), we see a good agreement between the pure state (dots) and the thermal state results (solid line). We see marked oscillations at low temperatures with a time period  $\tau_p = L/v_f$  (see text).

### *U*-macrostate

In this case, we set  $L = N = 1024$  in all our numerics. Some of our main observations are:

1. In Fig. (2.3), we show the spatial profiles of the *U*-macrovariables, given by the expectation values of the operators in Eq. (2.34), at different times starting with the gas in the region  $(0, L/2)$  and with  $A = 20$  partitions of the system. Results are shown for both the pure state and the thermal state initial conditions and we find a very good agreement between the two. We observe that at late times, all three fields approach uniform profiles which characterize our equilibrium state.
2. In Fig. (2.4), we consider two fixed cells centered at  $x = L/4$  and  $3L/4$  and plot the time-evolution of the number of particles in these cells. We again see a good agreement between the pure state and the thermal state initial conditions. An oscillatory relaxation to the uniform equilibrium state is observed. We note that the oscillation period in the low-temperature limit is given by  $\tau_p = L/v_f$  where  $v_f$  is the Fermi velocity. The amplitude of the oscillations decreases with increasing temperature.
3. The evolution of the Boltzmann entropy  $S_B^U$  at the two temperatures are shown



(a)  $T = 2\pi/5$ ,  $\mu = 19.83$ ,  $\Delta s = 1.46$

(b)  $T = 10\pi$ ,  $\mu = 22.02$ ,  $\Delta s = 0.88$

Figure 2.5: **Fermions:**  $U$ -macrostate entropy growth for fermions for  $N = L = 1024$  at two different temperatures and for two different coarse-graining scales with  $A = 20$  (blue lines) and  $A = 40$  (red lines). Results are presented for the pure state (dots) and thermal state (solid lines) initial conditions. The initial sharp rise corresponds to the filling of the two empty cells on either side of the unfilled part of the circle. This jump is smaller for finer coarse-graining size. We also observe an initial flat profile in (a) which persists till time  $(L/4)/v_f$ , where  $v_f$  is the Fermi velocity. At large times, in all cases, the entropy saturates to the thermodynamic entropy of the new equilibrium state (corresponding to uniform values of the three conserved fields on the circle). The sub-captions give the values for the change in entropy per particle,  $\Delta s$ , for the two cases.

in Fig. (2.5), for two choices of cell sizes, with  $A = 20, 40$ . We see a convergence of the growth curve with decreasing cell size. A monotonic growth of the entropy and an eventual saturation to the expected equilibrium value (corresponding to uniform values of the conserved fields) is observed. In the low-temperature case, we observe an initial jump in the  $S_B^U$  followed by a small flat regime and then a sharp increase. The initial jump size is smaller for finer coarse-graining. On the other hand, the initial flat profile seen in Fig. (2.5)(a) is a result of the sharp cutoff in the momentum distribution in the low-temperature Fermi gas. The flat region is observed till time  $(L/4)/v_f$ , where  $v_f$  is the Fermi velocity, which corresponds to the time taken by the gas to fill the circle for the first time.

### $f$ -macrostate

In this case, we set  $L = N = 2048$  in all our numerics. Some of our main observations are:

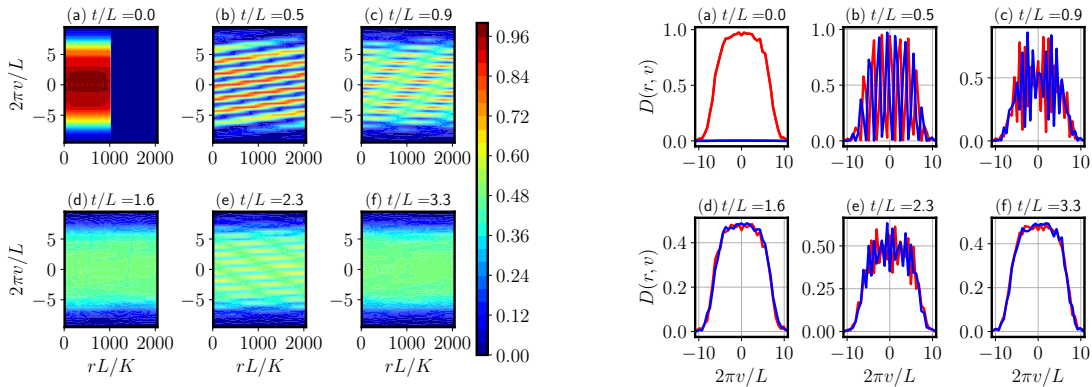
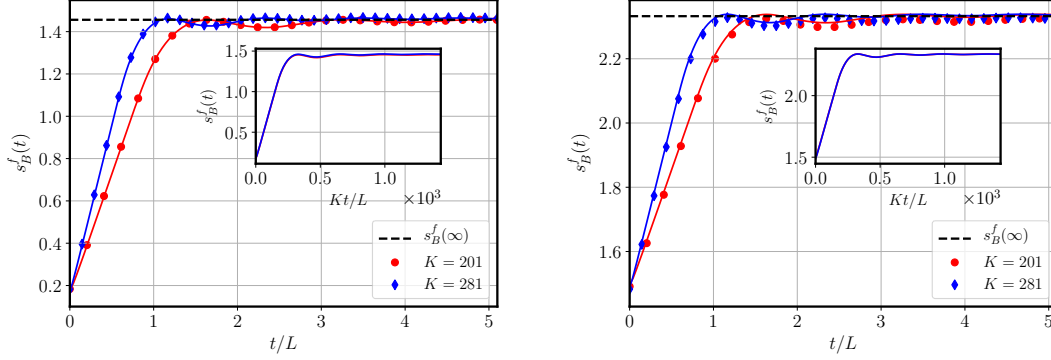


Figure 2.6: **Fermions - evolution of  $f$ -macrovariables.** Top left: Heat map plot of the wave packet density for parameters  $T = 2\pi$ ,  $\mu = 21.53$ ,  $N = L = 2048$ , and  $K = 201$ . Top right: The wave packet density as a function of momentum at two values of  $r = K/4$  (red) and  $r = 3K/4$  (blue), at the same time instances as in the heat map. Bottom left: The entropy evolution with time where the points  $a - f$  correspond to the same time snapshots as in the top row. The relative values of the entropy at these points are consistent with the presence of structures (or lack thereof) in the heat map and the cross-sectional profiles.

1. To see the evolution of the  $f$ -macrovariables, we plot heat maps in the top left of Fig. (2.6) showing the values of wavepacket density  $D_\alpha$  in the two-dimensional  $\alpha = (r, v)$  plane for an intermediate temperature  $T = 2\pi$ . We present six different time snapshots indicated by (a)-(e). The wavepacket density is initially flat in the box and there is an oscillatory relaxation to an eventual flat profile over the circle. We see an interference pattern that disappears in (d) and reappears in (e) and then again disappears in (f). This feature is more manifest in the top right panel of Fig. (2.6) which shows the wave packet density as a function of momentum at two values of  $r = K/4$  (red) and  $r = 3K/4$  (blue), at the same time instances as in the heat map. These features lead to an oscillatory relaxation of the entropy growth curve as seen in the bottom left panel of Fig. (2.6) where we find that the time for the



(a)  $T = 2\pi/5$ ,  $\mu = 19.82$ ,  $\Delta s = 1.28$

(b)  $T = 10\pi$ ,  $\mu = 22.01$ ,  $\Delta s = 0.84$

Figure 2.7: **Fermions**: Time evolution of the  $f$ -macrostate entropy per particle,  $s_B^f$ , at two different temperatures and for two coarse-graining scales  $K$  at each temperature. We see very good agreement between results for the pure state (red dots) and thermal state (solid lines) initial conditions. The inset in each plot shows the collapse of different  $K$  curves on re-scaling time.

entropy to first reach the saturation value, i.e, the point (d) is given by  $L^2/(2\pi K)$ . This is also the period of the subsequent oscillations seen in the entropy evolution. This time scale can be understood within a semi-classical framework and using the results from Ref. [19]. There it was shown that the time scale of oscillations of  $s_B^f$  is given by  $\tau = L/\Delta v$ , where  $\Delta v$  is the momentum coarse-graining scale. In the quantum case, we replace this by  $\Delta v = \Delta p/m = 2\pi\hbar K/(mL)$ . With our choice of units  $\hbar = m = 1$ , we therefore get  $\tau = L^2/(2\pi K)$ .

- In Fig. (2.7), we plot the entropy growth for the two temperatures (low and high) and for two different  $K$  values corresponding to each temperature. At both coarse graining scales,  $K$ , we see a good agreement between the entropy calculated from the pure state and the thermal state initial conditions. The entropy saturates to a value as predicted from Eqs. (2.50, 2.53). In the inset, we see a collapse of the data for different  $K$  on scaling time by  $K$ , consistent with the expression for  $\tau$  mentioned above. Note that similar oscillations and collapse of data were seen in the entropy growth in the free expansion of the non-interacting classical ideal gas [19].

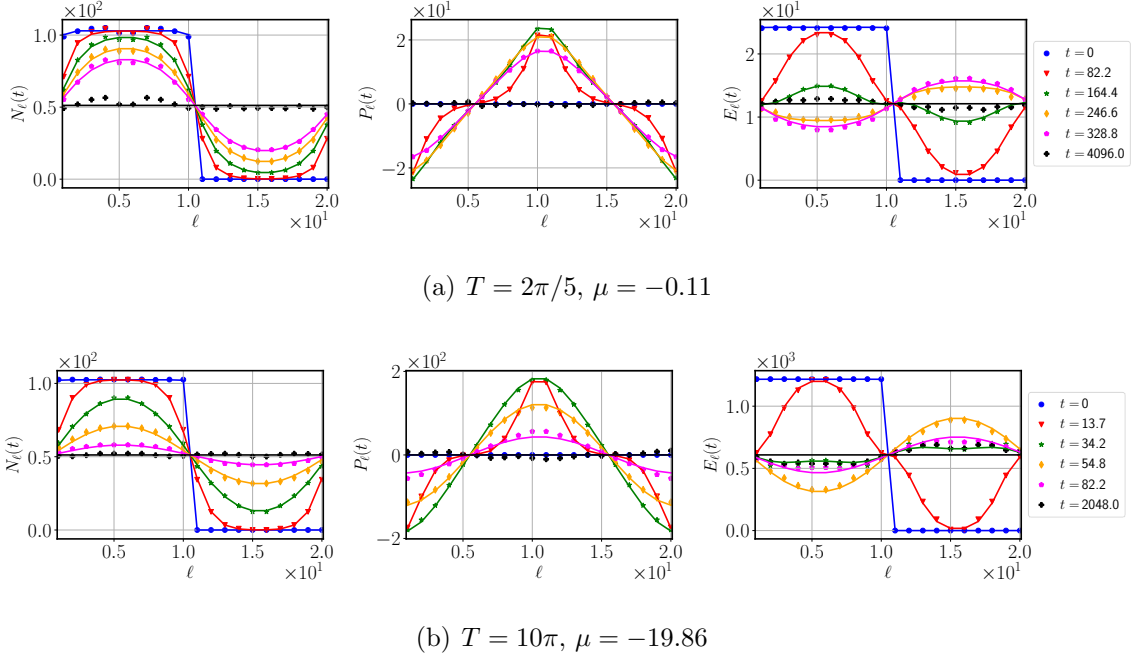


Figure 2.8: **Bosons - evolution of  $U$ -macrovariables**: Plots showing the spatial profiles of the number of particles, the total momentum, and the total energy in each of the  $A = 20$  cells for  $N = L = 1024$  at different times. Results are presented for two different temperatures  $T = 2\pi/5$ ,  $10\pi$ , and chemical potentials are fixed so that the mean density is set at  $\rho = 1$ . We see a reasonable agreement between the pure state (red dots) and the thermal state (solid lines) results, but significant deviations (due to finite-size effects) are observed at the latest times.

## 2.5.2 Bosons

We now present results for bosons for the  $U$  and  $f$  macrovariables. Except at very low temperatures, we find that several features are the same as that of fermions irrespective of the difference in statistics. We also highlight the striking differences between bosons and fermions. For bosons at very low temperatures, only levels with the energy of order  $\lesssim k_B T$  will be occupied. The number of occupied levels is thus small unless we consider very large  $N$ . Therefore it is difficult to see relaxation at such low temperatures and we do not consider such temperatures.

### $U$ -macrostate

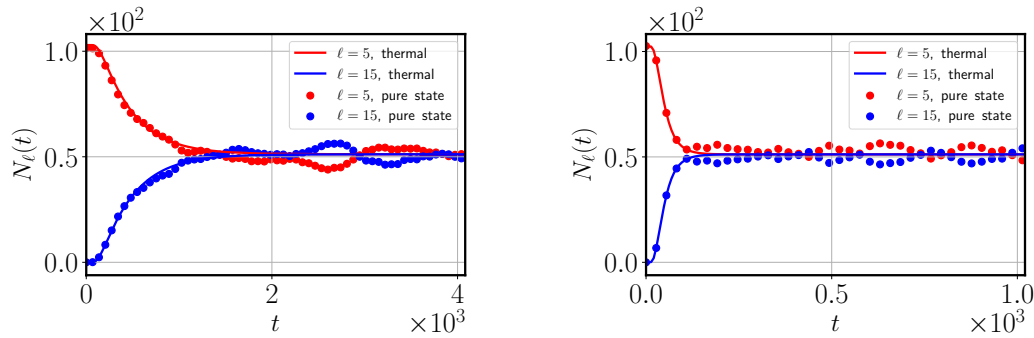
In Fig. (2.8) we show the spatial profiles of the  $U$ -macrovariables, given by the expectation values of the operators in Eq. (2.34), at different times starting with the gas in the left half of the box. We again consider a partition of the box into  $A = 20$  cells. Results are

shown for both the pure state and the thermal state initial conditions and as before we find reasonable agreement between the two though we find significant differences at long times. In general, we find that for bosons the agreement is not as good as that of fermions due to stronger finite size effects. This is because, for a fixed total particle number and temperature, the typical number of occupied levels in the pure state is less for bosons compared to that for fermions and fluctuations are larger [see Fig. (2.2)].

In Fig. (2.9), we consider two fixed cells located on the two halves of the circle centered at  $x = L/4$  and  $3L/4$  and plot the time-evolution of the number of particles inside these cells. We again see a reasonable agreement between the results from the pure and thermal states, though the differences are significantly larger than what was seen for fermions. It is worth noting that unlike in the case of fermions, here we do not see any oscillations but rather a monotonic relaxation to the uniform equilibrium state. The oscillations in the fermionic case arise due to the sharpness of the distribution near the Fermi energy at low temperatures which allows one to define a typical velocity  $v_f$  – hence a period of oscillation  $\tau_p = L/v_f$ . On the other hand in the case of bosons, we cannot identify such a typical velocity. Note that even though the evolution equation for the Wigner function is formally identical for bosons and fermions (as also classical particles), differences arise due to the form of the initial conditions. More precisely, for a typical pure state corresponding to thermal equilibrium, the form of the initial state is entirely different for bosons and fermions. The evolution of the Boltzmann entropy per particle  $s_B^U$  at the two temperatures is shown in Fig. (2.10), for two choices of cell sizes  $A = 20, 40$ . We observe: (i) a convergence of the growth curve with decreasing cell size; (ii) a monotonic growth of the entropy and an eventual saturation to the expected equilibrium value (corresponding to uniform values of the conserved fields).

### ***f*-macrostate**

For the *f*-macrostate, we again plot the heat map of the wavepacket density and the corresponding entropy growth curve in Fig. (2.11). The results look similar to fermions, except for the fact that the wavepacket density for bosons is more smeared out as compared to fermions. This is due to the usual difference between the Bose and the Fermi function at low temperatures. However, in the entropy growth curves for bosons in



(a)  $T = 2\pi/5$ ,  $\mu = -0.11$ ,  $N = L = 1024$

(b)  $T = 10\pi$ ,  $\mu = -19.85$ ,  $N = L = 1024$

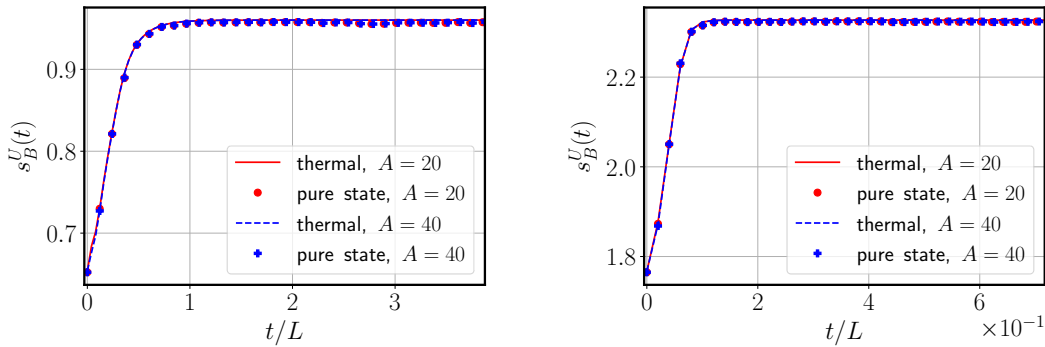
Figure 2.9: **Bosons**: Time evolution of the number of particles inside the 5<sup>th</sup> and 15<sup>th</sup> cells out of a total of  $A = 20$  cells for  $N = L = 1024$ . As in Fig. (2.8), we see a reasonable agreement, at early times, between the pure state (dots) and the thermal state results (solid line) while at longer times there are significant deviations. Note that the thermal data shows the absence of oscillations while in the pure state data, we see fluctuations that are expected to decrease with increasing system size.

Fig (2.12), the saturation value of the entropy depends rather strongly on  $K$ , especially in the low-temperature case [see details in appendix (A.3)].

## 2.6 Discussions and summary

The main aim of this study has been to use Boltzmann's ideas to construct an entropy function that can be defined for a pure quantum state and which allows us to characterize irreversibility in macroscopic systems. For the example of the quantum ideal gas, two sets of macroscopic descriptions (called  $U$  and  $f$ ) were defined that provide a coarse-grained view of the system, which is in a pure quantum state. The evolution of the entropy functions associated with these macrostates was studied for the case where the gas, initially in a pure state and spatially confined, was allowed to expand to twice its volume. We summarize and comment on some of our main results.

1. The  $U$ -macrovariables are the coarse-grained operators corresponding to the number, momentum, and energy of particles in spatial cells of size  $\delta = L/A$ . For both fermions and bosons, we see that the macrostates reach a steady state characterized by the three fields reaching homogeneous spatial profiles. Depending on the



(a)  $T = 2\pi/5$ ,  $\mu = -0.11$ ,  $\Delta s = 0.31$

(b)  $T = 10\pi$ ,  $\mu = -19.86$ ,  $\Delta s = 0.56$

Figure 2.10: **Bosons**:  $U$ -macrostate entropy growth for  $N = L = 1024$  at two different temperatures and for two different coarse-graining scales with  $A = 20$  (blue lines) and  $A = 40$  (red lines). Results are presented for the pure state (dots) and thermal state (solid lines) initial conditions. Unlike for fermions, the initial sharp rise is not seen in the case of bosons. At large times, in all cases, the entropy saturates to the thermodynamic entropy of the new equilibrium state (corresponding to uniform values of the three conserved fields on the circle). The sub-captions give the values for the change in entropy per particle,  $\Delta s$ , for the two cases.

parameter values, we see either damped or oscillatory relaxation of the fields to the steady state. However, we always observe a monotonic increase of the associated entropy,  $s_B^U$ .

2. The definition of our  $f$ -macrostate is aimed at obtaining an analogue of the single-particle phase space density in classical systems. A natural candidate for this are the number operators corresponding to a localized wavepacket set of basis states. While these operators are not bonafide macrovariables, we nevertheless can use their *expectation values* as macrovariables to identify macrostates and compute an entropy function by maximizing the Gibbs-von Neumann entropy, given those expectation values.

The wavepackets that we construct are located at discrete space and momentum points, denoted  $\alpha \equiv (r, v)$ , and localized on a scale of  $\hbar$ . We show that the average occupancy of these states denoted  $D_\alpha$ , constitute a coarse-graining of the Wigner function on a scale of  $\hbar$ . Unlike the Wigner function,  $D_\alpha$  is positive and is thus similar to the so-called Husimi function [78]. However, the Husimi function has the full information on the one-particle density matrix and so for non-interacting

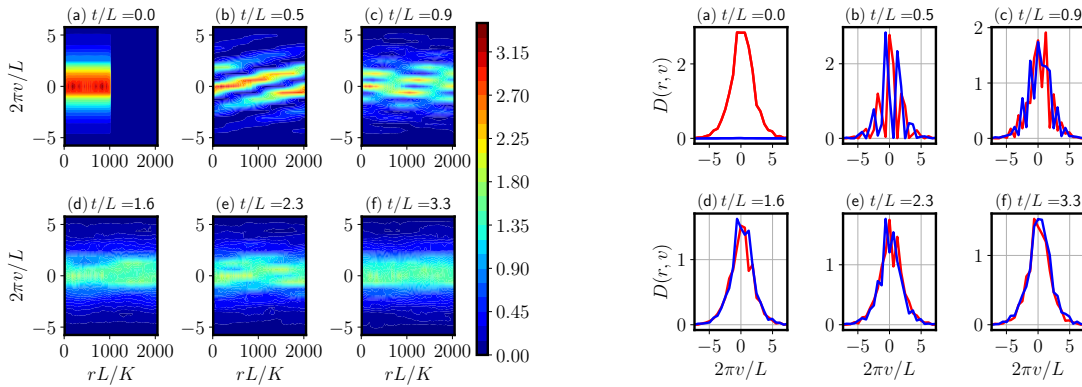
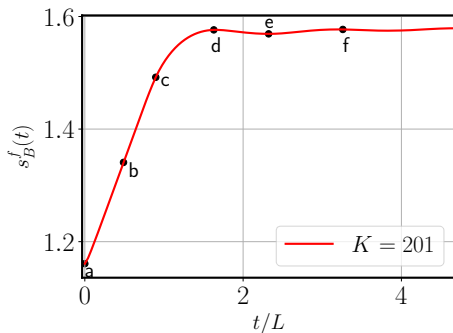


Figure 2.11: **Bosons - evolution of  $f$ -macrovariables.** Top left: Heat map plot of the wave packet density at  $T = 2\pi$ ,  $\mu = -1.7$ ,  $N = L = 2048$ , and  $K = 201$ . Top right: The wave packet density as a function of momentum at two values of  $r = K/4$  (red) and  $r = 3K/4$  (blue), at the same time instances as in the heat map. Bottom left: The entropy evolution with time where the points  $a - f$  correspond to the same time snapshots as in the top row. Like fermions, here also the relative values of the entropy at these points are consistent with the presence of structures (or lack thereof) in the heat map and the cross-sectional profiles.



systems, it cannot be used for the construction of an entropy function. The function  $D_\alpha$  incorporates coarse-graining required to demonstrate entropy growth in the quantum ideal gas. We note that the Wehrl entropy [79] uses the Husimi function and has been used to study irreversibility in interacting quantum systems [80–82].

Our  $f$ -macrostate entropy,  $S_B^f$ , also increases with time and reaches a steady state saturation value. In this case, the entropy growth is oscillatory with a period given by  $L/\Delta p$  where  $\Delta p$  is the momentum coarse-graining scale – this can be understood from semi-classical considerations. The change in entropy per particle satisfies the bound  $\ln 2 \leq \Delta s_B^f \leq 2 \ln 2$  for fermions and  $0 \leq \Delta s_B^f \leq \ln 2$  for bosons. This can be understood from the momentum distribution in the final state.

3. Results obtained for the evolution of pure states were compared with those of

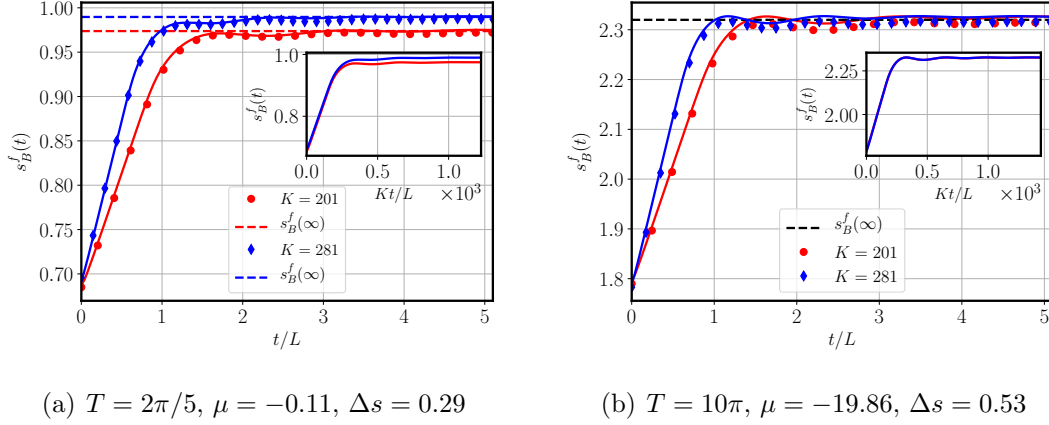


Figure 2.12: **Bosons**: Time evolution of the  $f$ -macrostate entropy per particle,  $s_B^f$ , at two different temperatures and for two coarse-graining scales  $K$  at each temperature. We see a good agreement between results for the pure state (red dots) and thermal state (solid lines) initial conditions. The inset in each plot shows the collapse of different  $K$  curves on re-scaling time.

corresponding thermal initial states and we showed evidence of their equivalence at larger system sizes. This demonstrates typicality in the dynamical evolution. Bosons showed larger finite size effects at low temperatures because of the fact that a relatively smaller number of single-particle levels are occupied and the number fluctuations is larger.

4. From the single-particle spectrum on the circle, it is clear that the system has an exact recurrence at a time  $\tau_{rec} = L^2/\pi$  (in units of  $m = \hbar = 1$ ). However for both our macrovariables, relaxation to the steady state occurs on a time scale  $\tau_{eq} \sim L$  and so, in the thermodynamic limit  $L, N \rightarrow \infty$  with  $L/N$  constant, there is a clear separation between the relaxation and recurrence time-scales. This kind of recurrence is expected whenever the single-particle spectrum is given in terms of integers and would be observed in quantum particles in harmonic traps but would not be present in generic anharmonic potentials (see for e.g [83]).

As expected, our system does not reach a Gibbs equilibrium state. The final effective temperature and chemical potential corresponding to the final particle and energy density do not determine the true single-particle momentum distribution, which is not able to attain thermal equilibrium for the quantum ideal gas. This is different from the classical

gas, where an initial Maxwell velocity distribution would continue to be the correct equilibrium velocity distribution for the expanded gas. In quantum gas, it would be necessary to include interactions to allow the momentum distribution to relax to thermal equilibrium; this does not happen for the ideal quantum gas. A recent study considered Boltzmann's entropy growth in a classical interacting gas and interesting differences with the non-interacting case were noted [20]. The effect of interactions in the quantum case would be interesting to explore, however, this would then become a highly entangled many-body system and thus very challenging to treat accurately.

# Chapter 3

## Generalized hydrodynamics and approach to Generalized Gibbs equilibrium for a classical harmonic chain

In this chapter, we study the other part of our thesis which is to study thermalization and check the validity of the prediction of generalized hydrodynamics (GHD) for a classical harmonic chain. Being an integrable system, the harmonic chain thermalizes to a generalized Gibbs ensemble. We study the GHD evolution of the harmonic chain and its approach to the GGE state. Following is a summary of our main results:

- We clarify how the Wigner function method [67] is related to the correlation matrix approach in [46]. In particular, we write an explicit expression for the Wigner function in terms of the Fourier transform of the local correlation function — this allows us to show the equivalence between the Euler equation in [46] and the equation satisfied by the Wigner function [see Sec. (3.2.1)].
- We express all the local conserved densities and currents in terms of the Wigner function which allows us to write the hydrodynamic equations for all the conserved quantities. The equation for the coarse-grained Wigner function can thus be considered as the GHD equation for the harmonic chain. This approach is similar to

that used for deriving the GHD equation for free fermions [42].

- Using the non-interacting structure, we solve the GHD equations analytically and obtain explicit expressions for the time evolution of the density and current profiles starting from non-equilibrium initial conditions. We compare these solutions with microscopic computations and find remarkable agreement.
- On the infinite line, the domain wall spreads ballistically and from our solution of GHD equations we can compute the exact scaling functions corresponding to both the density and current profiles. At any fixed location, the density and the current corresponding to any conserved quantity approach a stationary finite value in the  $t \rightarrow \infty$  limit. The approach to the steady state value is  $\sim 1/t$  and  $\sim 1/t^2$ , for densities and currents respectively. Therefore the stationary state inside any finite segment should be describable by a GGE which, in addition to the conserved densities, also includes all the associated currents that are conserved in the infinite geometry [64].
- For the domain wall initial condition on a finite chain, we observe that the chain relaxes to a final stationary state that is consistent with a GGE state in which all the conserved densities become homogeneous in space and stationary in time while the corresponding currents vanish. Note that in this case, current conservation is violated by the reflections at the boundaries. The conserved densities and the associated currents approach their stationary values as  $1/\sqrt{t}$  in the  $t \rightarrow \infty$  limit.
- The final expected GGE state in the finite chain is characterized by chemical potentials  $\{\lambda_n\}$  that are completely determined by the values of the conserved quantities. We provide explicit expressions for them in terms of the conserved densities. For the particular case of the initial condition composed of two Gibbs states at different temperatures, the final stationary state is also a Gibbs state. For the other case studied in this work in which the initial domain wall state is composed of two GGEs where only the first two Lagrange parameters are non-zero in either half of the chain, we find that the final state is also expected to be a GGE with chemical potentials that decay exponentially in strength for large  $n$ .

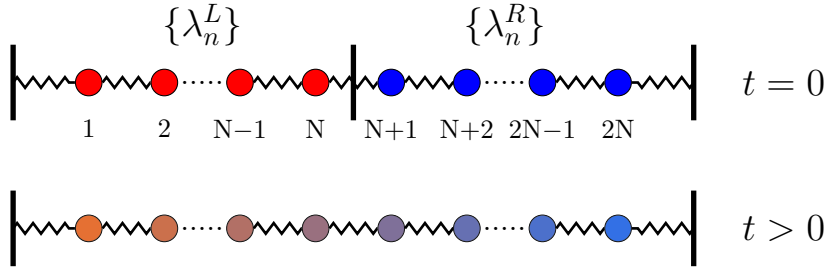


Figure 3.1: Plot showing a schematic of the harmonic chain system of length  $2N$ . Initially, at  $t = 0$ , the left and right halves are disconnected and in general, described by two GGEs with unequal chemical potentials  $\lambda_n^L \neq \lambda_n^R$ . At  $t > 0$ , the two halves interact and the system evolves as a whole towards a new stationary state.

### 3.1 Microscopic description of the system

In this section, we define the microscopic model of our classical harmonic chain and state the exact expressions for various correlation functions that can be obtained from the solution of the microscopic dynamics. We consider a chain of  $2N$  particles of unit masses whose positions and momenta are denoted by  $\{q_j, p_j\}$ ,  $j = 1, \dots, 2N$ . Assuming fixed boundary conditions:  $q_0 = q_{2N+1} = 0$ , the Hamiltonian is given by

$$H = \sum_{j=1}^{2N} \frac{p_j^2}{2} + \sum_{j=0}^{2N} \frac{(q_{j+1} - q_j)^2}{2} = \frac{1}{2} (\mathbf{p}^T \mathbf{p} + \mathbf{q}^T \Phi \mathbf{q}), \quad (3.1)$$

where  $\mathbf{q} = \{q_1, \dots, q_{2N}\}$  and  $\mathbf{p} = \{p_1, \dots, p_{2N}\}$  are vectors containing the particle positions and momenta respectively and  $\Phi$  denotes the force matrix with elements  $\Phi_{j,j'} = 2\delta_{j,j'} - \delta_{j+1,j'} - \delta_{j-1,j'}$  for  $j, j' = 1, 2, \dots, 2N$ , where  $\delta_{j,j'}$  is Kronecker delta. This gives us the equations of motion (EOM)

$$\ddot{\mathbf{q}} = -\Phi \mathbf{q}. \quad (3.2)$$

Let  $U$  be the matrix of eigenfunctions that diagonalises  $\Phi$  *i.e.*,  $U^T \Phi U = \Omega^2$  where  $\Omega_{k,k'}^2 = \omega_k^2 \delta_{k,k'}$ . The eigenvalues and eigenfunctions are given by

$$\omega_{k_\ell}^2 = 2(1 - \cos k_\ell), \quad (3.3a)$$

$$\psi_{k_\ell}(j) = U_{jk_\ell} = \sqrt{\frac{2}{2N+1}} \sin jk_\ell, \quad (3.3b)$$

$$\text{where } k_\ell = \frac{\pi \ell}{2N+1}, \ell = 1, \dots, 2N. \quad (3.3c)$$

We can write down a general solution to Eq. (3.2) in matrix notation as

$$\mathbf{q}(t) = \dot{A}(t)\mathbf{q}(0) + A(t)\mathbf{p}(0), \quad (3.4a)$$

$$\mathbf{p}(t) = \ddot{A}(t)\mathbf{q}(0) + \dot{A}(t)\mathbf{p}(0), \quad (3.4b)$$

where we have defined

$$A(t) = U \frac{\sin(\Omega t)}{\Omega} U^T. \quad (3.5)$$

For a harmonic chain of  $N$  particles, one can construct  $N$  number of local conserved quantities which we denote by  $Q^{(n)}(\mathbf{p}, \mathbf{q})$ ,  $n = 0, 1, 2, \dots, N-1$ . These conserved quantities are of the form:

$$Q^{(n)}(\mathbf{p}, \mathbf{q}) = \frac{1}{2} (\mathbf{p}^T B^{(n)} \mathbf{p} + \mathbf{q}^T M^{(n)} \mathbf{q}), \quad (3.6)$$

where  $B^{(n)}$  and  $M^{(n)}$  are  $N \times N$  symmetric matrices [see Sec. (3.2.2) for a detailed discussion]. The general stationary state of the chain is therefore described by a GGE of the form

$$P_{\text{GGE}}(\mathbf{p}, \mathbf{q}) = \frac{1}{Z(\{\lambda_n\})} \exp \left( - \sum_{n=0}^{N-1} \lambda_n Q^{(n)} \right), \quad (3.7)$$

where  $\lambda_n$  are the corresponding Lagrange multipliers that determine the average values of the conserved quantities. Here,  $Z(\{\lambda_n\})$  is the GGE partition function for a chain of

$N$  particles, which is explicitly given by [see Appendix (B.1)]

$$Z(\{\lambda_n\}) = (2\pi)^N \prod_{\ell=1}^N \frac{1}{\omega_{k_\ell} \sum_{n=0}^{N-1} \lambda_n \cos(nk_\ell)}, \quad (3.8)$$

where  $\omega_k$  and  $k_\ell$  are given in Eqs. (3.3a, 3.3c), respectively.

**Initial condition:** As shown in the schematic in Fig. (3.1), our system comprises of two such  $N$ -particle chains that are initially in a domain wall configuration described by a product of two GGE states

$$P_{\text{in}} = \frac{e^{-\sum_n \lambda_n^L Q_L^{(n)}}}{Z^L} \times \frac{e^{-\sum_n \lambda_n^R Q_R^{(n)}}}{Z^R}, \quad (3.9)$$

with different values of the Lagrange multipliers in the left and right halves, denoted respectively by  $\{\lambda_n^L\}$  and  $\{\lambda_n^R\}$ , corresponding to the conserved quantities  $Q_L^{(n)}$  and  $Q_R^{(n)}$ . Substituting the expression for  $Q^{(n)}$  from Eq. (3.6) into Eq. (3.9), we can express  $P_{\text{in}}$  in the following Gaussian form

$$P_{\text{in}} = \frac{1}{Z^L Z^R} \exp\left(-\frac{1}{2}[\mathbf{p}^T \mathcal{B} \mathbf{p} + \mathbf{q}^T \mathcal{M} \mathbf{q}]\right), \quad (3.10)$$

where  $\mathcal{B}$  and  $\mathcal{M}$  are  $2N \times 2N$  symmetric matrices defined as

$$\mathcal{B} = \begin{pmatrix} \sum_n \lambda_n^L B^{(n)} & 0 \\ 0 & \sum_n \lambda_n^R B^{(n)} \end{pmatrix}, \quad \mathcal{M} = \begin{pmatrix} \sum_n \lambda_n^L M^{(n)} & 0 \\ 0 & \sum_n \lambda_n^R M^{(n)} \end{pmatrix}, \quad (3.11)$$

where the Lagrange multipliers are chosen such that  $\mathcal{B}$  and  $\mathcal{M}$  are positive definite matrices.

The initial correlations can be immediately inferred from Eq. (3.10) and are given by  $\langle \mathbf{q}(0) \mathbf{q}(0)^T \rangle = \mathcal{M}^{-1}$ ,  $\langle \mathbf{p}(0) \mathbf{p}(0)^T \rangle = \mathcal{B}^{-1}$ , and  $\langle \mathbf{p}(0) \mathbf{q}(0)^T \rangle = 0$ . Using Eq. (3.4), the

equal time two-point correlations can then be easily obtained and we find

$$\langle \mathbf{q}(t)\mathbf{q}(t)^T \rangle = A(t)\mathcal{B}^{-1}A(t) + \dot{A}(t)\mathcal{M}^{-1}\dot{A}(t), \quad (3.12a)$$

$$\langle \mathbf{p}(t)\mathbf{p}(t)^T \rangle = \dot{A}(t)\mathcal{B}^{-1}\dot{A}(t) + \ddot{A}(t)\mathcal{M}^{-1}\ddot{A}(t), \quad (3.12b)$$

$$\langle \mathbf{q}(t)\mathbf{p}(t)^T \rangle = A(t)\mathcal{B}^{-1}\dot{A}(t) + \dot{A}(t)\mathcal{M}^{-1}\ddot{A}(t), \quad (3.12c)$$

where  $A(t)$  is given in Eq. (3.5).

## 3.2 Wigner function, conserved quantities and connection to GHD

In this section, we discuss the Generalized Hydrodynamics (GHD) for the harmonic chain through its connection to the Wigner function formalism. This is similar to the approach followed in [42] for non-interacting fermions on a one-dimensional lattice. Using GHD, we obtain an analytical understanding of the correlations and conserved quantities on a macroscopic scale. Unless stated otherwise, we will assume the chain to be infinite at both ends for which the eigen-spectrum in Eq. (3.3a) becomes continuous:  $\omega^2(k) = 2(1 - \cos k)$  where  $k \in [-\pi, \pi]$ .

### 3.2.1 Wigner function: its relation to the correlation matrix and evolution

Although the Wigner function was originally introduced as a quantum analog of the classical phase space distribution [73, 74], it has also been used widely in the context of transport and hydrodynamics of classical harmonic crystals. Following [67], we construct the Wigner function for the classical harmonic chain defined in Eq. (3.1). For this, we first define the quantity

$$a(k, \tau) = \frac{1}{\sqrt{2}} \left[ \sqrt{\omega(k)}q(k, \tau) + \frac{i}{\sqrt{\omega(k)}}p(k, \tau) \right], \quad (3.13)$$

where the Fourier and inverse Fourier transforms are defined as

$$q(k, \tau) = \sum_{j \in \mathbb{Z}} e^{-ijk} q_j(\tau); \quad q_j(\tau) = \int_{-\pi}^{\pi} \frac{dk}{2\pi} e^{ijk} q(k, \tau), \quad (3.14a)$$

$$p(k, \tau) = \sum_{j \in \mathbb{Z}} e^{-ijk} p_j(\tau); \quad p_j(\tau) = \int_{-\pi}^{\pi} \frac{dk}{2\pi} e^{ijk} p(k, \tau), \quad (3.14b)$$

$$a(k, \tau) = \sum_{j \in \mathbb{Z}} e^{-ijk} a_j(\tau); \quad a_j(\tau) = \int_{-\pi}^{\pi} \frac{dk}{2\pi} e^{ijk} a(k, \tau), \quad (3.14c)$$

where  $a_j(\tau)$  is defined as the Fourier transform of  $a(k, \tau)$ . The quantity  $a(k, \tau)$  has a simple evolution:  $a(k, \tau) = e^{-i\omega(k)\tau} a(k, 0)$ . We then define the Wigner function in terms of  $a(k, \tau)$  as

$$W^1(y, k, \tau) = \int_{-2\pi}^{2\pi} \frac{d\xi}{4\pi} e^{i\xi y} \langle a^*(k - \xi/2, \tau) a(k + \xi/2, \tau) \rangle = \sum_{j \in \mathbb{Z}} e^{-ijk} \langle a_{y-j/2}^*(\tau) a_{y+j/2}(\tau) \rangle, \quad (3.15)$$

where  $y \in \mathbb{Z}/2$ . The sum on  $j$  runs over even/odd integers if  $y$  is integer/half-integer and the average is over an initial ensemble. Substituting Eq. (3.13) into Eq. (3.15), we obtain

$$\begin{aligned} W^1(y, k, \tau) &= \frac{1}{2} \int_{-2\pi}^{2\pi} \frac{d\xi}{4\pi} \sum_{j, j' \in \mathbb{Z}} e^{i\xi(y-(j+j')/2)} e^{i(j-j')k} \\ &\times \left[ \sqrt{\omega(k - \xi/2)\omega(k + \xi/2)} \langle q_j q_{j'} \rangle(\tau) + i \sqrt{\frac{\omega(k - \xi/2)}{\omega(k + \xi/2)}} \langle q_j p_{j'} \rangle(\tau) \right. \\ &\left. - i \sqrt{\frac{\omega(k + \xi/2)}{\omega(k - \xi/2)}} \langle p_j q_{j'} \rangle(\tau) + \frac{1}{\sqrt{\omega(k - \xi/2)\omega(k + \xi/2)}} \langle p_j p_{j'} \rangle(\tau) \right]. \end{aligned} \quad (3.16)$$

Note that the above expression readily provides a connection between the Wigner function and the correlations. If we assume the correlations to be homogeneous in space, then we obtain a steady-state Wigner function

$$W_{ss}(k) = \frac{1}{2} \left[ \omega(k) F_{11}(k) - i F_{12}(k) + i F_{21}(k) + \frac{1}{\omega(k)} F_{22}(k) \right], \quad (3.17)$$

where  $F_{mn}(k)$  are elements of the  $2 \times 2$  correlation matrix

$$F(k) = \sum_{r \in \mathbb{Z}} e^{ikr} \bar{F}(r), \quad \text{where } \bar{F}(j - j') = \begin{pmatrix} \langle q_j q_{j'} \rangle & \langle q_j p_{j'} \rangle \\ \langle p_j q_{j'} \rangle & \langle p_j p_{j'} \rangle \end{pmatrix}. \quad (3.18)$$

We point out that  $F_{11}^*(k) = F_{11}(k)$ ,  $F_{22}^*(k) = F_{22}(k)$  and  $F_{12}^*(k) = F_{21}(k)$  so that the Wigner function is always real. In thermal equilibrium at an inverse temperature  $\beta$ , we simply get

$$W_\beta(k) = \frac{1}{\beta \omega(k)}. \quad (3.19)$$

In general, for a chain of  $N$  particles in GGE described by the distribution in Eq. (3.7), the Wigner function can be obtained by computing the correlations  $F_{j-j'}$  in Eq. (3.18) and using them in Eq. (3.17). One finds the following explicit expression

$$W_{GGE}(k) = \frac{1}{\omega(k) \sum_{n=0}^{N-1} \lambda_n \cos nk}. \quad (3.20)$$

On the other hand, when the correlation functions are inhomogeneous and evolve over a large space-time scale, one can assume the system to be locally in a steady state characterized by the local values of the correlations. Transforming to the scaled variables:  $x = \epsilon y, t = \epsilon \tau$ , and taking the  $\epsilon \rightarrow 0$  limit in Eq. (3.16), the relation in Eq. (3.17) between the Wigner function and the correlation matrix gets modified to

$$W(x, k, t) = \frac{1}{2} \left[ \omega(k) F_{11}(x, k, t) - i F_{12}(x, k, t) + i F_{21}(x, k, t) + \frac{1}{\omega(k)} F_{22}(x, k, t) \right], \quad (3.21)$$

where

$$W(x, k, t) := \lim_{\epsilon \rightarrow 0} W^1(x/\epsilon, k, t/\epsilon) = \lim_{\epsilon \rightarrow 0} \epsilon \int_{-2\pi/\epsilon}^{2\pi/\epsilon} \frac{d\eta}{4\pi} e^{i\eta x} \langle a^*(k - \epsilon\eta/2, t/\epsilon) a(k + \epsilon\eta/2, t/\epsilon) \rangle, \quad (3.22)$$

and

$$F_{mn}(x, k, t) = \lim_{\epsilon \rightarrow 0} \sum_{r=-\infty}^{\infty} e^{-irk} \left\langle y_{[\epsilon^{-1}x-r/2]}^m y_{[\epsilon^{-1}x+r/2]}^n \right\rangle (\epsilon^{-1}t). \quad (3.23)$$

Here  $y_j^1 = q_j$  is the displacement and  $y_j^2 = p_j$  is the momentum of the  $j^{\text{th}}$  oscillator. The local correlation functions  $F_{mn}(x, k, t)$  were shown, in Ref. [46], to satisfy the Euler equations, using which one can show that the Wigner function  $W(x, k, t)$  satisfies the following transport equation:

$$\partial_t W(x, k, t) + \omega'(k) \partial_x W(x, k, t) = 0. \quad (3.24)$$

A more direct way to derive this equation is to start with  $W^1(y, k, \tau)$  defined in Eq. (3.15) which satisfies

$$\partial_\tau W^1(y, k, \tau) = i \int_{-2\pi}^{2\pi} \frac{d\xi}{4\pi} e^{i\xi y} [\omega(k - \xi/2) - \omega(k + \xi/2)] \langle a^*(k - \xi/2, \tau) a(k + \xi/2, \tau) \rangle. \quad (3.25)$$

We then transform to the scaled variables ( $x = \epsilon y, t = \epsilon \tau$ ) on both sides of Eq. (3.25) and expand the right-hand side in  $\epsilon$ . At the leading order in  $\epsilon$ , one finds the evolution equation (3.24) for  $W(x, k, t)$  defined in Eq. (3.22). On an infinite line, the solution of Eq. (3.24) at a later time can be simply obtained by boosting the initial function  $W(x, k, 0)$  with the phonon group velocity  $\omega'(k)$ :

$$W(x, k, t) = W(x - \omega'(k)t, k, 0). \quad (3.26)$$

Note that in thermal equilibrium the average internal energy at a site can be obtained from  $W_\beta(k)$  [given in Eq. (3.19)] as  $\int_{-\pi}^{\pi} dk / (2\pi) \omega(k) W_{eq}(k) = 1/\beta$ . Generalizing this relation to the inhomogeneous case we find that the average internal energy density can be expressed in terms of the Wigner function as

$$e(x, t) = \int_{-\pi}^{\pi} \frac{dk}{2\pi} \omega(k) W(x, k, t). \quad (3.27)$$

It is easy to see that  $e(x, t)$  satisfies a continuity equation  $\partial_t e(x, t) + \partial_x j(x, t) = 0$  where the average energy current density is given by

$$j(x, t) = \int_{-\pi}^{\pi} \frac{dk}{2\pi} \omega(k) \omega'(k) W(x, k, t). \quad (3.28)$$

In the following, we discuss other conserved densities and the associated currents and show how one can express them in terms of the Wigner function.

### 3.2.2 Conserved quantities and connection to GHD

The Hamiltonian in Eq. (3.1) for  $N \rightarrow \infty$  can be written in Fourier space as

$$H = \int_{-\pi}^{\pi} \frac{dk}{2\pi} \mathcal{E}(k) \quad \text{with} \quad \mathcal{E}(k) = \frac{\omega(k)}{2} [a^*(k, \tau) a(k, \tau) + a^*(-k, \tau) a(-k, \tau)], \quad (3.29)$$

where  $a(k, \tau)$  is defined in Eq. (3.13). Note that  $\mathcal{E}(k) = \frac{|p(k, \tau)|^2}{2} + \omega(k)^2 \frac{|q(k, \tau)|^2}{2}$  represents the energy of a single mode and is a conserved quantity. This allows us to define a set of new conserved quantities as the following linear combinations:

$$Q^{(n)} := \int_{-\pi}^{\pi} \frac{dk}{2\pi} \mathcal{E}(k) e^{ink} = \int_{-\pi}^{\pi} \frac{dk}{2\pi} \cos nk \omega(k) a^*(k, \tau) a(k, \tau) \quad \text{for } n = 0, 1, 2, \dots \quad (3.30)$$

We now show that these conserved quantities are local in nature, i.e., they can be expressed as a sum over local terms. To see this, we insert Eq. (3.13) into Eq. (3.30) and after some simplifications, obtain

$$Q^{(n)} = \sum_{\ell \in \mathbb{Z}} \varrho_{\ell}^{(n)}(\tau) \quad \text{where} \quad \varrho_{\ell}^{(n)}(\tau) = \frac{1}{2} [p_{\ell} p_{\ell-n} + 2q_{\ell} q_{\ell-n} - q_{\ell} q_{\ell-n+1} - q_{\ell} q_{\ell-n-1}]. \quad (3.31)$$

It is easy to see that the microscopic densities  $\varrho_{\ell}^{(n)}(\tau)$  obey a discrete continuity equation

$$\partial_{\tau} \varrho_{\ell}^{(n)}(\tau) = j_{\ell-1}^{(n)}(\tau) - j_{\ell}^{(n)}(\tau), \quad (3.32)$$

where the microscopic current  $\mathbf{j}_\ell^{(n)}(\tau)$  from site  $\ell$  to  $\ell + 1$  is given by

$$\mathbf{j}_\ell^{(n)}(\tau) = \frac{1}{2} (p_{\ell-n+1}q_\ell - p_{\ell-n}q_{\ell+1}). \quad (3.33)$$

Note that  $Q^{(n)}$  in Eq. (3.31) can also be written in matrix form as

$$Q^{(n)} = \frac{1}{2} (\mathbf{p}^T B^{(n)} \mathbf{p} + \mathbf{q}^T M^{(n)} \mathbf{q}), \quad (3.34)$$

where  $B^{(n)}$  and  $M^{(n)}$  are symmetric matrices defined as

$$B_{\ell,\ell'}^{(n)} = \frac{1}{2} (\delta_{\ell-n,\ell'} + \delta_{\ell+n,\ell'}), \quad (3.35a)$$

$$M_{\ell,\ell'}^{(n)} = \delta_{\ell-n,\ell'} + \delta_{\ell+n,\ell'} - \frac{1}{2} (\delta_{\ell-n+1,\ell'} + \delta_{\ell+n-1,\ell'} + \delta_{\ell-n-1,\ell'} + \delta_{\ell+n+1,\ell'}). \quad (3.35b)$$

These matrix forms are particularly useful for numerical microscopic computations. For initial conditions chosen from a distribution such as in Eq. (3.9), one is interested in the average values of these conserved densities  $\rho_\ell^{(n)} := \langle \varrho_\ell^{(n)} \rangle$ , which, on a macroscopic scale can be expressed in terms of the coarse-grained Wigner function  $W(x, k, t)$ . Noting  $\langle a^*(k, \tau) a(k, \tau) \rangle = \sum_y W^1(y, k, \tau)$  from Eq. (3.15) and substituting it in Eq. (3.30) gives

$$\langle Q^{(n)} \rangle = \sum_y \int_{-\pi}^{\pi} \frac{dk}{2\pi} \cos nk \omega(k) W^1(y, k, \tau). \quad (3.36)$$

Defining  $\rho^{(n)}(x, t) = \lim_{\epsilon \rightarrow 0} \epsilon^{-1} \rho_{[\epsilon^{-1}x]}^{(n)}(\epsilon^{-1}t)$ , we can write  $\langle Q^{(n)} \rangle = \int dx \rho^{(n)}(x, t)$ , where

$$\rho^{(n)}(x, t) = \int_{-\pi}^{\pi} \frac{dk}{2\pi} \cos nk \omega(k) W(x, k, t). \quad (3.37)$$

Using Eq. (3.24), it is easy to see that the densities in Eq. (3.37) obey the continuity equation

$$\partial_t \rho^{(n)}(x, t) + \partial_x \mathbf{j}^{(n)}(x, t) = 0, \quad (3.38)$$

where the macroscopic currents  $j^{(n)}(x, t)$  are given by

$$j^{(n)}(x, t) = \int_{-\pi}^{\pi} \frac{dk}{2\pi} \cos nk \omega(k) \omega'(k) W(x, k, t). \quad (3.39)$$

We now comment on the connection to GHD. We see that the coarse-grained Wigner function in Eq. (3.22) indeed has the structure of GHD equations if we identify  $W(x, k, t)$  as a phase space distribution of non-interacting quasi-particles (basically the phonons) with position  $x$ , momentum  $k$ , and velocity  $\omega'(k)$ . This identification is natural as was pointed out in [67]. The definition of conserved densities and currents in Eqs. (3.37, 3.39) is consistent with this identification. One question is regarding the positivity of  $W$ . At the microscopic level, it can be negative but coarse-graining can lead to a positive-definite quantity. Various possibilities for coarse-graining exist, for example through the construction of the Husimi function (see [47]). Another more physical construction was discussed in [23] in the context of a non-interacting quantum gas where the coarse-grained Wigner function has the direct interpretation as the number of quasi-particles in a coarse-grained cell. Note that at a physical level, the GHD equation for the harmonic chain is the same as the Peierls-Boltzmann equation for a weakly anharmonic chain with collision terms neglected (see [84]).

### 3.3 Comparison between microscopic and hydrodynamic evolution from domain wall initial condition

In this section, we apply the hydrodynamic formulation developed in Sec. (3.2) to the study of equilibration of the harmonic chain starting from a domain wall initial condition as depicted in Fig. (3.1). We study both a chain of infinite extent and a chain of finite length with fixed boundaries. For the hydrodynamics of a finite-sized chain, we assume its length to be  $2L$  with  $2N$  particles and lattice constant  $\epsilon$  such that  $N \rightarrow \infty$  and  $\epsilon \rightarrow 0$  with  $L = N\epsilon$  held fixed. The microscopic numerical calculations are done for finite  $N$  with unit lattice constant and to compare the results, we make the identification  $L = N$ . For both

cases, we consider two types of domain wall initial conditions. In the first choice, only the (inverse) temperatures in the two halves of the chain are different, namely  $\beta_1$  and  $\beta_2$ , while all other Lagrange multipliers are zero *i.e.*,  $\lambda_n^L = \lambda_n^R = 0$ ,  $\forall n \geq 1$ . For a finite chain, this implies that the only conserved quantity with a non-zero average value initially is the energy. As a consequence of conservation laws, the values of higher conserved quantities remain zero in the final stationary state which is thus again expected to be described by a GE with the final temperature being the mean of the initial temperatures in the two halves. In Sec. (3.3.1), by studying the evolution of the conserved densities we show how the system relaxes to the final expected GE state. In Sec. (3.3.2), we consider the second choice of the initial condition in which the first two parameters (Lagrange multipliers) are non-zero and take different values in the two halves while other parameters are zero on both sides. In this case, all the conserved quantities have non-zero average values initially, and consequently, we expect the system to finally reach a GGE stationary state. Once again, by solving the GHD equation in Eq. (3.24), we study the evolution of the conserved densities and the associated currents and show how the system in this case approaches the final expected GGE state. Note that for both types of initial conditions, the infinite chain is expected to go to a GGE stationary state which is current carrying. This is due to the presence of additional conserved quantities (see (66)).

### 3.3.1 Domain wall initial condition composed of two GE states

As described above, initially, there is a domain wall at the center of the chain such that the left and the right halves are described by two GE states with unequal inverse temperatures  $\beta_1$  and  $\beta_2$  respectively. We first consider the simpler case of an infinite chain which will be followed by a discussion on finite-size chain.

**Infinite chain:** We assume the domain wall to be initially located at  $x = 0$ . Using Eq. (3.19), we can write down the Wigner function at  $t = 0$  as

$$W(x, k, 0) = \frac{1}{\omega(k)} \left[ \frac{1}{\beta_1} - \left( \frac{1}{\beta_1} - \frac{1}{\beta_2} \right) \Theta(x) \right]. \quad (3.40)$$

From Eq. (3.26) the Wigner function at time  $t$  can straightforwardly be written as

$$W(x, k, t) = \frac{1}{\omega(k)} \left[ \frac{1}{\beta_1} - \left( \frac{1}{\beta_1} - \frac{1}{\beta_2} \right) \Theta(x - \omega'(k)t) \right]. \quad (3.41)$$

Substituting Eq. (3.41) into Eq. (3.27) and performing the integral, one can compute the average internal energy density  $e(x, t)$ . Since we assume the lattice spacing to be unity, the particle density is unity everywhere. Hence,  $e(x, t)$  is essentially the temperature profile which is explicitly given by

$$T(x, t) := e(x, t) = \begin{cases} \frac{1}{\beta_1}, & x < -t \\ \frac{1}{2} \left( \frac{1}{\beta_1} + \frac{1}{\beta_2} \right) - \frac{1}{\pi} \left( \frac{1}{\beta_1} - \frac{1}{\beta_2} \right) \sin^{-1} \left( \frac{x}{t} \right), & |x| < t \\ \frac{1}{\beta_2}, & x > t \end{cases} \quad (3.42)$$

The expressions for other conserved quantities  $\rho^{(n)}(x, t)$  for  $n > 0$  can be calculated similarly and are given by

$$\rho^{(n)}(x, t) = \frac{1}{2n\pi} \left( \frac{1}{\beta_1} - \frac{1}{\beta_2} \right) \sin \left\{ 2n \cos^{-1} \left( \frac{x}{t} \right) \right\} \Theta \left( 1 - \frac{|x|}{t} \right). \quad (3.43)$$

Using the continuity equation in Eq. (3.38) for  $n = 0$ , we can also write down the energy current density

$$\mathbf{j}^{(0)}(x, t) = \frac{1}{\pi} \left( \frac{1}{\beta_1} - \frac{1}{\beta_2} \right) \sqrt{1 - \left( \frac{x}{t} \right)^2} \Theta \left( 1 - \frac{|x|}{t} \right). \quad (3.44)$$

The higher currents  $\mathbf{j}^{(n)}(x, t)$  for  $n > 0$  can be similarly evaluated and one finds the following expression

$$\begin{aligned} \mathbf{j}^{(n)}(x, t) &= \left[ 2n \frac{x}{t} \sin \left( 2n \mu \left( \frac{x}{t} \right) \right) + \sqrt{1 - \left( \frac{x}{t} \right)^2} \cos \left( 2n \mu \left( \frac{x}{t} \right) \right) \right] \\ &\times \frac{(-1)^{n+1}}{\pi(4n^2 - 1)} \left( \frac{1}{\beta_1} - \frac{1}{\beta_2} \right) \Theta \left( 1 - \frac{|x|}{t} \right), \end{aligned} \quad (3.45)$$

where  $\mu(z) = \sin^{-1}(z)$ .

To compare the numerical microscopic computations with the theoretical results from hydrodynamics, we coarse-grain the microscopic densities (and currents) by averaging over  $\Delta$  number of consecutive sites:

$$\bar{\rho}_y^{(n)}(t) = \frac{1}{\Delta} \sum_{j=(\ell-1)\Delta+1}^{\ell\Delta} \rho_j^{(n)}(t) \quad \text{where } y = \ell \frac{\Delta}{2}. \quad (3.46)$$

Note that we have expressed the coarse-grained densities as functions of macroscopic time variable  $t$ , because, as mentioned earlier, in our case  $\epsilon = 1$  which is small compared to  $L = N$ . In Fig. (3.2a) and Fig. (3.2b), we plot the coarse-grained temperature and the corresponding current density obtained numerically from the microscopic computations in a chain of length  $2N$ . In the insets of these figures, we show that these profiles have ballistic scaling and we compare the scaling functions with those (dashed black lines) obtained analytically in Eqs. (3.42) and (3.44) for temperature and the associated current respectively. The microscopic calculations are performed by evaluating averages of the corresponding microscopic quantities given in Eq. (3.31) and Eq. (3.33) and for that, we use the correlations from Eq. (3.12). We see that the hydrodynamic results for both temperature and energy current density match with the corresponding finite-size microscopic computations as long as  $t < N$ . This can be understood since  $N$  is the time taken by the step initial condition to spread and reach the boundaries.

It is interesting to note that in the  $t \rightarrow \infty$  limit, the currents at any fixed point  $x$  in the system approach stationary nonzero values given by

$$j_{ss}^{(n)} = \frac{(-1)^{n+1}}{\pi(4n^2 - 1)} \left( \frac{1}{\beta_1} - \frac{1}{\beta_2} \right), \quad (3.47)$$

and the relaxation happens as  $\sim 1/t^2$ . On the other hand, at any fixed location in the  $t \rightarrow \infty$  limit, all the densities of the conserved quantities approach zero except temperature which approaches the mean temperature. The relaxation to these stationary values occurs as  $\sim 1/t$ . Therefore any finite segment of the infinite chain reaches a non-equilibrium steady state (NESS) which cannot be described by a GE but possibly by a current carrying GGE instead, as shown for the quantum harmonic chain in [64].

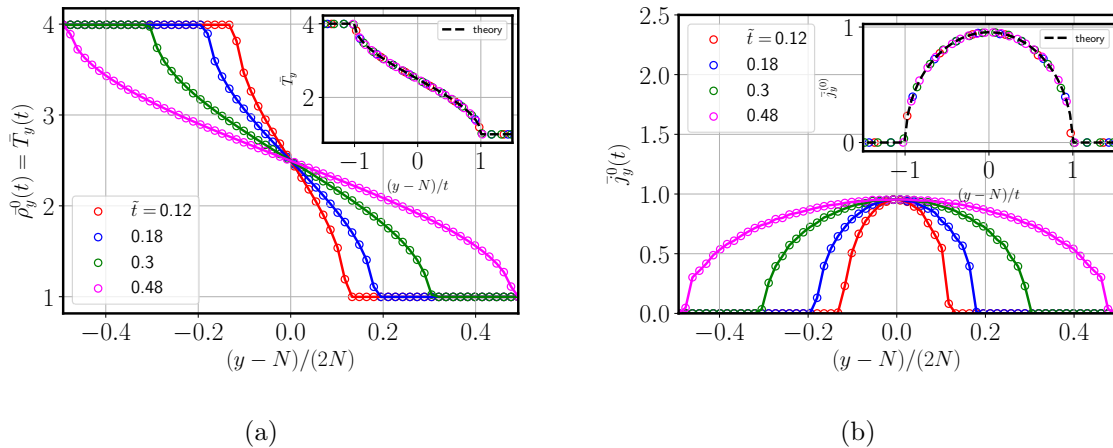


Figure 3.2: Plot showing the early time behavior of the coarse-grained microscopic (a) temperature profile and (b) energy current density profile at different times (in the scaled units  $\tilde{t} = t/(2N)$ ). The insets in both figures show the collapse of the profiles upon  $x/t$  scaling of the x-axis where  $x = y - N$ . The dashed black lines in the insets correspond to the analytic scaling functions obtained from Eq. (3.42) and Eq. (3.44) respectively. The coarse-graining was done over  $\Delta = 8$  consecutive sites. The parameters used are  $\beta_1 = 0.25, \beta_2 = 1.0$  and  $2N = 512$ .

As we will see below, this is different from the case of the finite chain where the steady state is indeed expected to be described by a GE since the currents, decay to zero due to reflections at the boundaries.

**Finite chain:** We now turn our attention to the case of a finite chain. Let the length of the chain be  $2L$  and the initial condition be that of a domain wall at  $x = L$  as given in Eq. (3.9) with  $\lambda_0^L = \beta_1, \lambda_0^R = \beta_2$  and all other  $\lambda_n^{L,R} = 0$ . Using Eq. (3.19), we can write down the Wigner function for the finite chain at  $t = 0$  as

$$W(x, k, 0) = \frac{1}{\omega(k)} \left[ \frac{1}{\beta_2} + \left( \frac{1}{\beta_1} - \frac{1}{\beta_2} \right) [\Theta(x+L) - \Theta(x-L)] \right], \quad (3.48)$$

where  $x \in [0, 2L]$ . Using Eq. (3.26) and taking care of reflections at the boundaries (following a similar procedure as done in Appendix A of Ref. [19]), the Wigner function

at a later time  $t$  is given by

$$W(x, k, t) = \frac{1}{\omega(k)} \left( \frac{1}{\beta_1} - \frac{1}{\beta_2} \right) \sum_{s=-\infty}^{\infty} [\Theta(x - \omega'(k)t + 4sL + L) - \Theta(x - \omega'(k)t + 4sL - L)] + \frac{1}{\beta_2 \omega(k)}. \quad (3.49)$$

Substituting Eq. (3.49) into Eq. (3.37) with  $n = 0$ , we obtain the following series representation for the temperature

$$T(x, t) = \frac{1}{\beta_2} + \left( \frac{1}{\beta_1} - \frac{1}{\beta_2} \right) \sum_{s=-\infty}^{\infty} \left[ I \left( \frac{x + 4sL + L}{t} \right) - I \left( \frac{x + 4sL - L}{t} \right) \right], \quad (3.50)$$

where we have defined the integral

$$I(z) := \int_{-1}^1 \frac{du \Theta(z - u)}{\pi \sqrt{1 - u^2}} = \begin{cases} 0, & z < -1 \\ \frac{1}{2} + \frac{1}{\pi} \sin^{-1} z, & |z| < 1 \\ 1, & z > 1 \end{cases} \quad (3.51)$$

Note that Eq. (3.49) can alternatively be written in a compact form

$$W(x, k, t) = \frac{1}{\omega(k)} \left[ \frac{1}{\beta_1} - \left( \frac{1}{\beta_1} - \frac{1}{\beta_2} \right) \Theta \left( \left\{ \frac{x - \omega'(k)t + L}{4L} \right\} - \frac{1}{2} \right) \right], \quad (3.52)$$

where  $\{x\} = x - [x]$  is the fractional part function. Defining  $z = \left\{ \frac{x - \omega'(k)t + L}{4L} \right\}$ , we write the Fourier series representation,  $\Theta \left( z - \frac{1}{2} \right) = \frac{1}{2} - \sum_{\ell \neq 0} \frac{(e^{\pi i \ell} - 1) e^{-2\pi i \ell z}}{2\pi i \ell}$ . Putting this in Eq. (3.52) gives

$$W(x, k, t) = \frac{1}{2\omega(k)} \left( \frac{1}{\beta_1} + \frac{1}{\beta_2} \right) + \frac{1}{\omega(k)} \left( \frac{1}{\beta_1} - \frac{1}{\beta_2} \right) \sum_{\ell \neq 0} \frac{\sin(\pi \ell / 2)}{(\pi \ell)} \exp \left( -2\pi i \ell \frac{x - \omega'(k)t}{4L} \right). \quad (3.53)$$

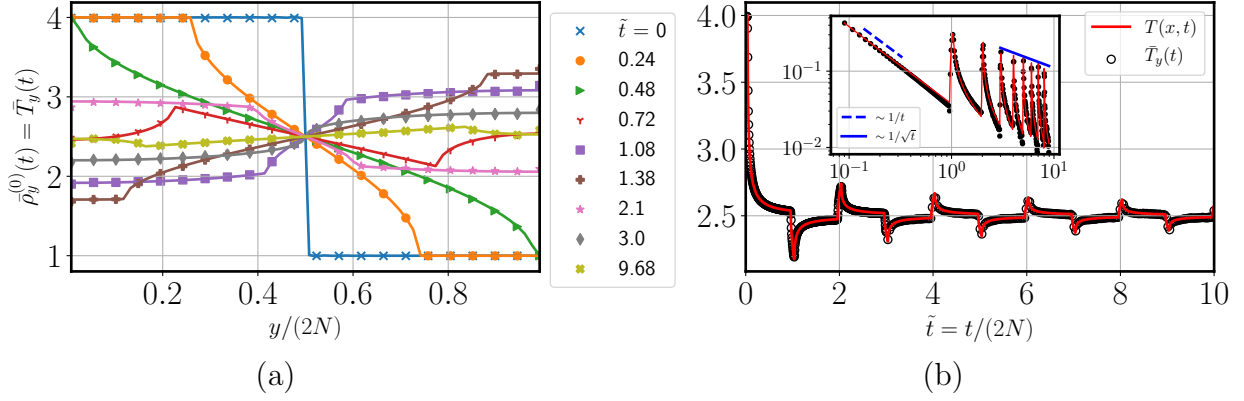


Figure 3.3: (a) Plot showing the coarse-grained temperature profile at different times  $\tilde{t} = t/(2N)$ . (b) shows the evolution of the temperature with time at a fixed coarse-grained point  $y/(2N) \approx 0.46$ . The inset in (b) shows the same curve on a log-log scale but with the steady state value subtracted. We observe a  $\sim 1/t$  decay at small times which, after many reflections from the boundaries, changes to a  $\sim 1/\sqrt{t}$  decay at large times as expected from the analytical expressions. In both figures, the points are calculated by coarse-graining the microscopic temperature profile whereas the continuous lines are obtained from the analytic GHD solutions. We find an excellent agreement between the coarse-grained microscopic and the GHD results. The coarse-graining is done over  $\Delta = 8$  consecutive sites. The parameters used are  $\beta_1 = 0.25$ ,  $\beta_2 = 1.0$  and  $2N = 512$ .

Now substituting Eq. (3.53) into Eq. (3.37) after setting  $n = 0$  and integrating over  $k$  yields an alternate series representation for the temperature profile

$$T(x, t) = \rho^{(0)}(x, t) = \frac{1}{2} \left( \frac{1}{\beta_1} + \frac{1}{\beta_2} \right) + \left( \frac{1}{\beta_1} - \frac{1}{\beta_2} \right) \sum_{\ell=1}^{\infty} \frac{\sin(\pi\ell/2)}{(\pi\ell/2)} \cos \frac{\pi\ell x}{2L} J_0 \left( \frac{\pi\ell t}{2L} \right), \quad (3.54)$$

where  $J_\nu(z)$  is the Bessel function.

From Eq. (3.53), we can also compute all other densities  $\rho^{(n)}(x, t)$  for  $n > 0$  and we find the following evolution

$$\rho^{(n)}(x, t) = (-1)^n \left( \frac{1}{\beta_1} - \frac{1}{\beta_2} \right) \sum_{\ell=1}^{\infty} \frac{\sin(\pi\ell/2)}{(\pi\ell/2)} \cos \frac{\pi\ell x}{2L} J_{2n} \left( \frac{\pi\ell t}{2L} \right). \quad (3.55)$$

Similarly putting Eq. (3.53) into Eq. (3.39) and integrating over  $k$  gives us the current

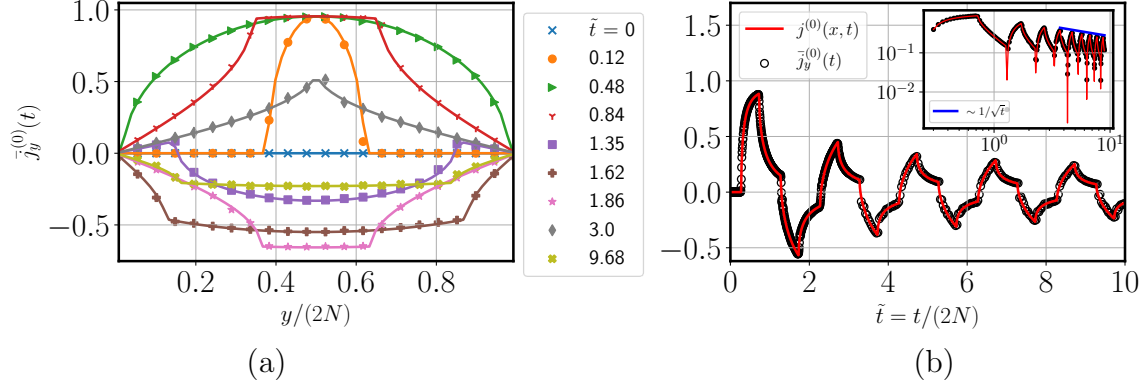


Figure 3.4: (a) Plot showing the coarse-grained energy current density profile at different times  $\tilde{t} = t/(2N)$ . (b) shows the evolution of the energy current density with time at a fixed coarse-grained point  $y/(2N) \approx 0.23$ . The inset in (b) shows the same curve on a log-log scale. We observe a  $\sim 1/\sqrt{t}$  decay at large times as expected from the analytical expressions. In both figures, the points are calculated by coarse-graining the microscopic energy current density profile whereas the continuous lines are obtained from the analytic GHD expressions. We find an excellent agreement between the coarse-grained microscopic and the GHD results. The coarse-graining is done over  $\Delta = 8$  consecutive sites. The parameters used are  $\beta_1 = 0.25, \beta_2 = 1.0$  and  $2N = 512$ .

densities

$$\mathbf{j}^{(0)}(x, t) = \left( \frac{1}{\beta_1} - \frac{1}{\beta_2} \right) \sum_{\ell=1}^{\infty} \frac{\sin(\pi\ell/2)}{(\pi\ell/2)} \sin \frac{\pi\ell x}{2L} J_1 \left( \frac{\pi\ell t}{2L} \right), \quad (3.56a)$$

$$\mathbf{j}^{(n)}(x, t) = \frac{(-1)^n}{2} \left( \frac{1}{\beta_1} - \frac{1}{\beta_2} \right) \sum_{\ell=1}^{\infty} \frac{\sin(\pi\ell/2)}{(\pi\ell/2)} \sin \frac{\pi\ell x}{2L} \left[ J_{2n+1} \left( \frac{\pi\ell t}{2L} \right) - J_{2n-1} \left( \frac{\pi\ell t}{2L} \right) \right], \quad n > 0. \quad (3.56b)$$

The Bessel function  $J_\nu(z)$  decays as  $1/\sqrt{z}$  for large  $z$ . Therefore, the temperature goes to a steady state value of  $(1/2)(\beta_1^{-1} + \beta_2^{-1})$  while all other quantities in Eqs. (3.55, 3.56) go to zero. All quantities relax as  $1/\sqrt{t}$  in the large  $t$  limit.

In Figs. (3.3-3.5), we show a comparison of the analytic results from hydrodynamics, for temperature, energy current density, and  $Q^{(1)}$  density, with those obtained numerically from the microscopics by computing averages of the corresponding microscopic quantities in Eqs. (3.31, 3.33) and using the correlations from Eq. (3.12).

In Fig. (3.3a) we show the temperature profiles at different scaled times  $\tilde{t} = t/2N$ . The initial front spreads freely as long as  $t < N$ . At  $t = N$  the front reaches the boundaries for

the first time and gets reflected back into the bulk. These reflections continue to even out the temperature in the two halves as can be observed from the profile corresponding to the largest time  $\tilde{t} = 9.68$  shown in (3.3a). The temperature eventually becomes flat and equal to the mean of the initial temperatures. In Fig. (3.3b), we show how the temperature evolves with time at a coarse-grained point  $y \approx (2N) \times 0.46$  that is slightly to the left of the center. The temperature remains unchanged until  $\tilde{t} = (N - y)/(2N) \approx 0.04$  which is the time taken by the edge of the front to reach that point (not visible in the scale of the plot). After that it starts decaying as  $\sim 1/t$  [see inset of Fig. (3.3b)] similar to the infinite chain case and continues to do so until an edge of the reflected front [in Fig. (3.3a)] crosses the particular coarse-grained point for the first time. The temperature at any given point continues to show an overall decay interspersed with the presence of isolated kinks that appear corresponding to the passing of an edge of the reflected front. Eventually, the temperature at a fixed coarse-grained point approaches the final value as  $\sim 1/\sqrt{t}$  (as also expected from our hydrodynamic calculations). In both figures, points represent numerical data, and the solid lines are analytical results from Eq. (3.54) and we observe an excellent agreement between the two, thus demonstrating the validity of the GHD results for the case of finite-size chains.

In Fig. (3.4a), we plot the energy current density profiles at a few different times. The current profile is initially zero everywhere and starts to grow from the center. As long as  $t < N$ , the current evolves according to Eq. (3.44) after which the reflections from the boundaries become relevant. Fig. (3.4b) shows the evolution of energy current density at a coarse-grained point that lies near the middle of the left half. The current stays zero until  $\tilde{t} = (N - y)/(2N) \approx 0.27$  which is the time taken by the edge of the front to reach that point. Here also we observe kinks that correspond to the passing of an edge of the reflected front of the current profile in Fig. (3.4a). The current eventually approaches zero as  $\sim 1/\sqrt{t}$  [see inset of Fig. (3.4b)]. We again see good agreement between the numerical microscopic computations and the analytical results from hydrodynamics.

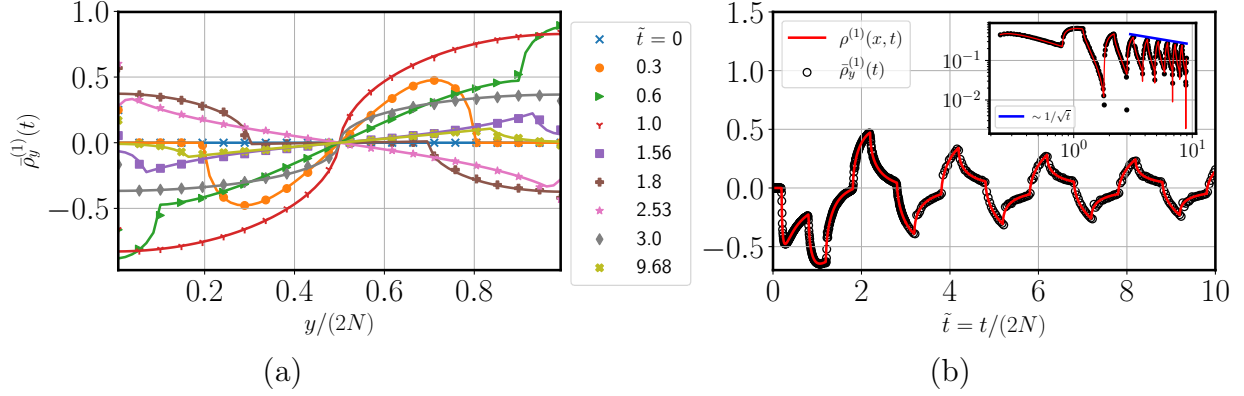


Figure 3.5: (a) Plot showing the coarse-grained  $Q^{(1)}$  density profile at different times  $\tilde{t} = t/(2N)$ . (b) shows the evolution of the  $Q^{(1)}$  density with time at a fixed coarse-grained point  $y/(2N) \approx 0.30$ . The inset in (b) shows the same curve on a log-log scale. We again observe a  $\sim 1/\sqrt{\tilde{t}}$  decay at large times as expected from the analytical expressions. In both figures, the points are calculated by coarse-graining the microscopic  $Q^{(1)}$  density profile whereas the continuous lines are obtained from the analytic GHD expressions. We find an excellent agreement between the coarse-grained microscopic and the GHD results. The coarse-graining is done over  $\Delta = 8$  consecutive sites. The parameters used are  $\beta_1 = 0.25, \beta_2 = 1.0$  and  $2N = 512$ .

### 3.3.2 Domain wall initial condition composed of two GGE states

We now consider a more general initial condition where the two halves are described by a product of two GGEs, as given in Eq. (3.9). The initial Wigner functions in the left and right parts are given by Eq. (3.20) with the Lagrange parameters  $\{\lambda_n^L\}$  and  $\{\lambda_n^R\}$  respectively. In the following, we focus on the particular case where only the first two parameters are non-zero and the rest are zero on both sides of the chain.

**Infinite chain:** Once again we assume that the domain wall is initially located at  $x = 0$  and the first two Lagrange multipliers have values  $\lambda_0^L = \beta_1$ ,  $\lambda_1^L = -\beta_1\gamma_1$ ,  $\lambda_0^R = \beta_2$ , and  $\lambda_1^R = -\beta_2\gamma_2$ . The initial Wigner function in this case is

$$W(x, k, 0) = \frac{1}{\omega(k)} \left[ \frac{1}{\beta_1(1 - \gamma_1 \cos k)} - \left( \frac{1}{\beta_1(1 - \gamma_1 \cos k)} - \frac{1}{\beta_2(1 - \gamma_2 \cos k)} \right) \Theta(x) \right], \quad (3.57)$$

which according to Eq. (3.26) takes the following form at time  $t$

$$W(x, k, t) = \frac{1}{\omega(k)} \left[ \frac{1}{\beta_1(1 - \gamma_1 \cos k)} - \left( \frac{1}{\beta_1(1 - \gamma_1 \cos k)} - \frac{1}{\beta_2(1 - \gamma_2 \cos k)} \right) \Theta(x - \omega'(k)t) \right]. \quad (3.58)$$

Using this solution in Eq. (3.37) and simplifying we find that the density profiles associated with the conserved quantities are given by

$$\rho^{(n)}(x, t) = \begin{cases} g^{(n)}(\beta_1, \gamma_1), & x < -t \\ \frac{1}{2} [g^{(n)}(\beta_1, \gamma_1) + g^{(n)}(\beta_2, \gamma_2)] \\ - \int_0^{\sin^{-1}(x/t)} \frac{d\theta}{\pi} \cos\{2n \cos^{-1} |\sin \theta|\} \left( \frac{1}{\beta_1(1 + \gamma_1 \cos 2\theta)} - \frac{1}{\beta_2(1 + \gamma_2 \cos 2\theta)} \right), & |x| < t \\ g^{(n)}(\beta_2, \gamma_2), & x > t \end{cases} \quad (3.59)$$

where the quantity  $g^{(n)}(\beta, \gamma)$  is given by

$$g^{(n)}(\beta, \gamma) = \frac{1}{\beta(1 + \gamma)} {}_3F_2^{\text{reg}} \left( \left\{ 1/2, 1, 1 \right\}; \left\{ 1 - n, 1 + n \right\}; \frac{2\gamma}{1 + \gamma} \right), \quad (3.60)$$

with  ${}_pF_q^{\text{reg}}(\{a_1, \dots, a_p\}; \{b_1, \dots, b_q\}; z)$  being the regularized generalized Hypergeometric function. The details of the calculation are given in Appendix (B.2). Putting  $n = 0$  in

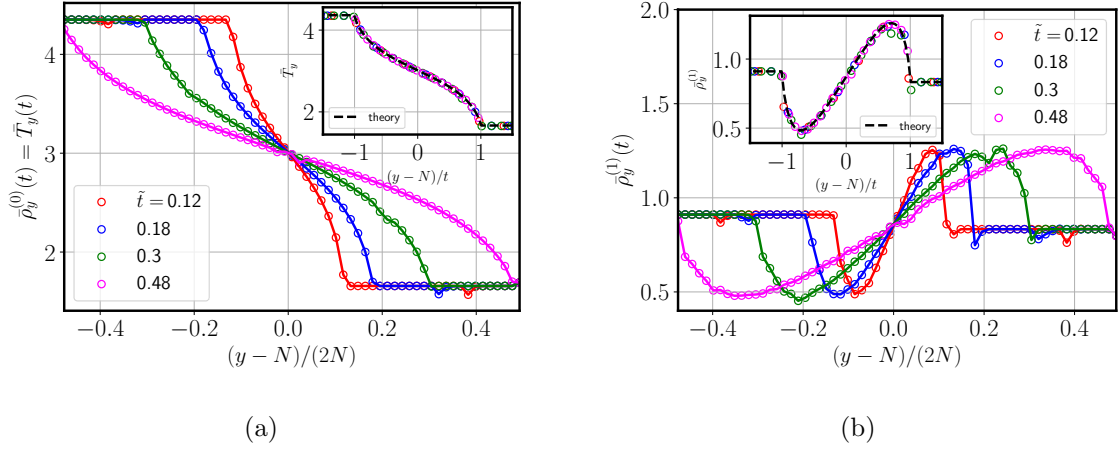


Figure 3.6: Plot showing the early time behavior of the coarse-grained microscopic (a) temperature profile and (b)  $Q^{(1)}$  density profile at different times (in the scaled units  $\tilde{t} = t/(2N)$ ). The insets in both figures show the collapse of the profiles upon  $x/t$  scaling of the x-axis where  $x = y - N$ . The dashed black lines in the insets correspond to the analytic scaling functions obtained from Eq. (3.61) and Eq. (3.63) respectively. The coarse-graining was done over  $\Delta = 8$  consecutive sites. The parameters used are  $\beta_1 = 0.25, \beta_2 = 1.0, \gamma_1 = 0.4, \gamma_2 = 0.8$  and  $2N = 512$ .

Eq. (3.59) and performing the integrals we find that the temperature profile is given by

$$T(x, t) = \rho^{(0)}(x, t) = \begin{cases} g^{(0)}(\beta_1, \gamma_1), & x < -t \\ \frac{1}{2} (g^{(0)}(\beta_1, \gamma_1) + g^{(0)}(\beta_2, \gamma_2)) - \frac{1}{\pi} [g^{(0)}(\beta_1, \gamma_1) \tan^{-1} \{u(\gamma_1)s(x/t)\} \\ - g^{(0)}(\beta_2, \gamma_2) \tan^{-1} \{u(\gamma_2)s(x/t)\}], & |x| < t \\ g^{(0)}(\beta_2, \gamma_2), & x > t \end{cases} \quad (3.61)$$

where  $g^{(0)}(\beta, \gamma) = \frac{1}{\beta\sqrt{1-\gamma^2}}$  and  $s(z)$  and  $u(\gamma)$  are defined as

$$s(z) = \frac{z}{\sqrt{1-z^2}}, \quad u(\gamma) = \sqrt{\frac{1-\gamma}{1+\gamma}}. \quad (3.62)$$

The expression for the density corresponding to  $Q^{(1)}$  is similarly given by

$$\rho^{(1)}(x, t) = \begin{cases} g^{(1)}(\beta_1, \gamma_1), & x < -t \\ \frac{1}{2} (g^{(1)}(\beta_1, \gamma_1) + g^{(1)}(\beta_2, \gamma_2)) \\ + \frac{1}{\pi} \left[ \left( \frac{1}{\beta_1 \gamma_1} \tan^{-1} \left\{ \frac{[1 - u(\gamma_1)]s(x/t)}{1 + u(\gamma_1)s(x/t)^2} \right\} - \frac{1}{\beta_2 \gamma_2} \tan^{-1} \left\{ \frac{[1 - u(\gamma_2)]s(x/t)}{1 + u(\gamma_2)s(x/t)^2} \right\} \right) \right] \\ - \frac{1}{\pi} [g^{(1)}(\beta_1, \gamma_1) \tan^{-1} \{u(\gamma_1)s(x/t)\} - g^{(1)}(\beta_2, \gamma_2) \tan^{-1} \{u(\gamma_2)s(x/t)\}], & |x| < t \\ g^{(1)}(\beta_2, \gamma_2), & x > t \end{cases} \quad (3.63)$$

where  $g^{(1)}(\beta, \gamma) = \frac{1}{\beta\gamma} \left( \frac{1}{\sqrt{1-\gamma^2}} - 1 \right)$  and  $s(z)$  and  $u(\gamma)$  are defined in Eq. (3.62).

In Fig. (3.6), we show a comparison of the analytic results from hydrodynamics with those obtained microscopically for a chain of length  $2N$ . The averages of the corresponding microscopic quantities in Eq. (3.31) are evaluated by using the correlations from Eq. (3.12). We see that the hydrodynamic results in Eqs. (3.61) and (3.63) for temperature and  $Q^{(1)}$  density, respectively, match with the corresponding finite-size microscopic computations as long as  $t < N$ .

**Finite chain:** We now turn our attention to the case of a finite chain. Let the length of the chain be  $2L$  and the initial condition be that of a domain wall at  $x = L$  as given in Eq. (3.9) with  $\lambda_0^L = \beta_1$ ,  $\lambda_1^L = -\beta_1\gamma_1$ ,  $\lambda_0^R = \beta_2$ ,  $\lambda_1^R = -\beta_2\gamma_2$  and all other  $\lambda_n^{L,R} = 0$ . Using Eq. (3.20) with these parameters in the two halves of the chain, we can write down the Wigner function at  $t = 0$  as

$$W(x, k, 0) = \frac{1}{\omega(k)} \left( \frac{1}{\beta_1(1 - \gamma_1 \cos k)} - \frac{1}{\beta_2(1 - \gamma_2 \cos k)} \right) [\Theta(x + L) - \Theta(x - L)] \\ + \frac{1}{\omega(k)} \frac{1}{\beta_2(1 - \gamma_2 \cos k)}, \quad (3.64)$$

where  $x \in [0, 2L]$ . As was argued in Sec. (3.3.1) for the finite chain, we can similarly

write down the Wigner function at time  $t$  as

$$W(x, k, t) = \frac{1}{\omega(k)} \left[ \frac{1}{\beta_2(1 - \gamma_2 \cos k)} + \left( \frac{1}{\beta_1(1 - \gamma_1 \cos k)} - \frac{1}{\beta_2(1 - \gamma_2 \cos k)} \right) \right. \\ \left. \times \sum_{s=-\infty}^{\infty} [\Theta(x - \omega'(k)t + 4sL + L) - \Theta(x - \omega'(k)t + 4sL - L)] \right]. \quad (3.65)$$

Substituting Eq. (3.65) into Eq. (3.37) with  $n = 0$ , we obtain the following series representation for the temperature

$$T(x, t) = \frac{1}{\beta_2 \sqrt{1 - \gamma_2^2}} + \sum_{s=-\infty}^{\infty} \left[ \frac{1}{\beta_1} I_{\gamma_1} \left( \frac{x + 4sL + L}{t} \right) - \frac{1}{\beta_2} I_{\gamma_2} \left( \frac{x + 4sL - L}{t} \right) \right], \quad (3.66)$$

where  $I_\gamma(z)$  is defined as the integral

$$I_\gamma(z) := \int_{-1}^1 \frac{du}{\pi} \frac{\Theta(z - u)}{\sqrt{1 - u^2} [1 - \gamma(2u^2 - 1)]}. \quad (3.67)$$

Note that, as before, Eq. (3.65) can alternatively be written in a compact form

$$W(x, k, t) = -\frac{1}{\omega(k)} \left( \frac{1}{\beta_1(1 - \gamma_1 \cos k)} - \frac{1}{\beta_2(1 - \gamma_2 \cos k)} \right) \Theta \left( \left\{ \frac{x - \omega'(k)t + L}{4L} \right\} - \frac{1}{2} \right) \\ + \frac{1}{\omega(k)} \frac{1}{\beta_1(1 - \gamma_1 \cos k)}, \quad (3.68)$$

As done in Sec. (3.3.1) for the finite case, we define  $z = \left\{ \frac{x - \omega'(k)t + L}{4L} \right\}$  and write the Fourier series representation,  $\Theta \left( z - \frac{1}{2} \right) = \frac{1}{2} - \sum_{\ell \neq 0} \frac{(e^{\pi i \ell} - 1) e^{-2\pi i \ell z}}{2\pi i \ell}$ . Putting this in Eq. (3.68) gives

$$W(x, k, t) = \frac{1}{2\omega(k)} \left( \frac{1}{\beta_1(1 - \gamma_1 \cos k)} + \frac{1}{\beta_2(1 - \gamma_2 \cos k)} \right) \\ + \frac{1}{\omega(k)} \left( \frac{1}{\beta_1(1 - \gamma_1 \cos k)} - \frac{1}{\beta_2(1 - \gamma_2 \cos k)} \right) \sum_{\ell \neq 0} \frac{\sin(\pi \ell / 2) \exp \left( -2\pi i \ell \frac{x - \omega'(k)t}{4L} \right)}{\pi \ell}. \quad (3.69)$$

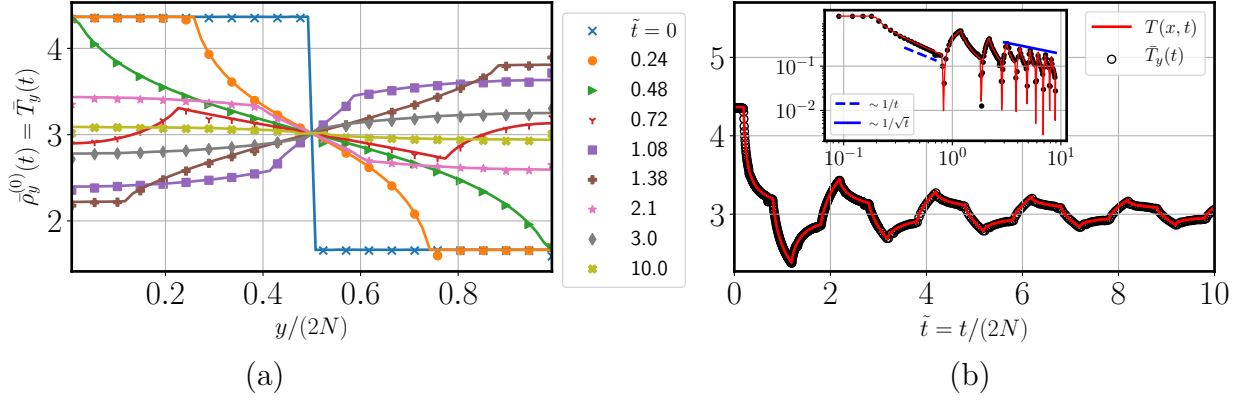


Figure 3.7: (a) Plot showing the coarse-grained temperature profile at different times  $\tilde{t} = t/(2N)$ . (b) shows the evolution of the temperature with time at a fixed coarse-grained point  $y/(2N) \approx 0.30$ . The inset in (b) shows the same curve on a log-log scale but with the steady state value subtracted. We observe a  $\sim 1/t$  decay at small times which, after many reflections from the boundaries, changes to a  $\sim 1/\sqrt{t}$  decay at large times as expected from the analytical expressions. In both figures, the points are calculated by coarse-graining the microscopic temperature profile whereas the continuous lines are obtained from the analytic GHD expressions. We find an excellent agreement between the coarse-grained microscopic and the GHD results. The coarse-graining is done over  $\Delta = 8$  consecutive sites. The parameters used are  $\beta_1 = 0.25, \beta_2 = 1.0, \gamma_1 = 0.4, \gamma_2 = 0.8$  and  $2N = 512$ .

Substituting Eq. (3.69) into Eq. (3.37), the evolution for  $\rho^{(n)}(x, t)$  can be formally written down as

$$\rho^{(n)}(x, t) = \rho_{GGE}^{(n)} + \sum_{\ell=1}^{\infty} \frac{\sin(\pi\ell/2)}{(\pi\ell/2)} \cos \frac{\pi\ell x}{2L} \left[ \frac{1}{\beta_1} C_{\ell}^{(n)}(\gamma_1, t) - \frac{1}{\beta_2} C_{\ell}^{(n)}(\gamma_2, t) \right], \quad (3.70)$$

where the stationary state density  $\rho_{GGE}^{(n)}$  is given by

$$\rho_{GGE}^{(n)} = \frac{1}{2} [g^{(n)}(\beta_1, \gamma_1) + g^{(n)}(\beta_2, \gamma_2)], \quad (3.71)$$

with  $g^{(n)}(\beta, \gamma)$  defined in Eq. (3.60) and  $C_{\ell}^{(n)}(\gamma, t)$  given by the integral

$$C_{\ell}^{(n)}(\gamma, t) = \int_0^{\pi} \frac{dk}{2\pi} \frac{2 \cos nk}{1 - \gamma \cos k} \cos \left( \frac{\pi\ell t}{2L} \cos \frac{k}{2} \right). \quad (3.72)$$

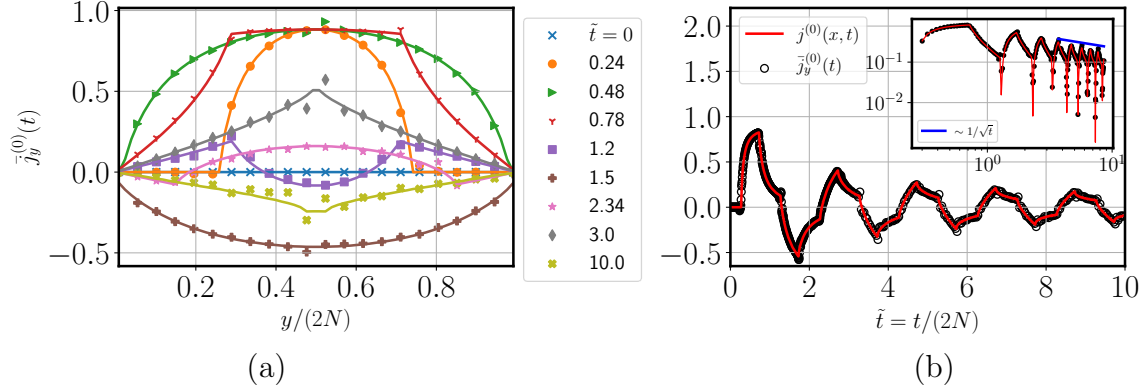


Figure 3.8: (a) Plot showing the coarse-grained energy current density profile at different times  $\tilde{t} = t/(2N)$ . (b) shows the evolution of the energy current density with time at a fixed coarse-grained point  $y/(2N) \approx 0.23$ . The inset in (b) shows the same curve on a log-log scale. We observe a  $\sim 1/\sqrt{t}$  decay at large times as expected from the analytical expressions. In both figures, the points are calculated by coarse-graining the microscopic energy current density profile whereas the continuous lines are obtained from the analytic GHD expressions. We find an excellent agreement between the coarse-grained microscopic and the GHD results. The coarse-graining is done over  $\Delta = 8$  consecutive sites. The parameters used are  $\beta_1 = 0.25, \beta_2 = 1.0, \gamma_1 = 0.4, \gamma_2 = 0.8$  and  $2N = 512$ .

Similarly, we can write down the formal expression for the currents  $\mathbf{j}^{(n)}(x, t)$

$$\mathbf{j}^{(n)}(x, t) = \sum_{\ell=1}^{\infty} \frac{\sin(\pi\ell/2)}{(\pi\ell/2)} \sin \frac{\pi\ell x}{2L} \left[ \frac{1}{\beta_1} D_{\ell}^{(n)}(\gamma_1, t) - \frac{1}{\beta_2} D_{\ell}^{(n)}(\gamma_2, t) \right], \quad (3.73)$$

where  $D_{\ell}^{(n)}(\gamma, t)$  is given by the integral

$$D_{\ell}^{(n)}(\gamma, t) = \int_0^{\pi} \frac{dk}{2\pi} \frac{2 \cos nk \cos(k/2)}{1 - \gamma \cos k} \sin \left( \frac{\pi\ell t}{2L} \cos \frac{k}{2} \right). \quad (3.74)$$

It can be shown that, in the large time limit, the densities and currents in Eq. (3.70) and Eq. (3.73) respectively relax to their equilibrium values as  $\sim 1/\sqrt{t}$ , similar to the finite-size case in Sec. (3.3.1). In Figs. (3.7-3.10), we show a comparison of the analytic results from hydrodynamics, for temperature, energy current density,  $Q^{(1)}$  density, and  $Q^{(1)}$  current density with those obtained numerically from the microscopics by computing averages of the corresponding microscopic quantities in Eqs. (3.31, 3.33) and using the correlations in Eq. (3.12). The qualitative features of the evolution of these quantities are similar to those for the finite chain in Sec. (3.3.1). We again find a good agreement

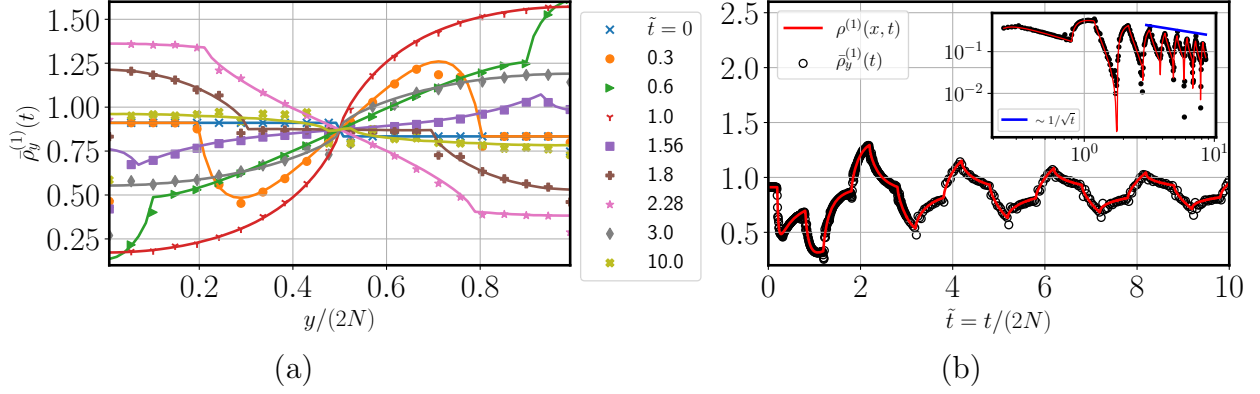


Figure 3.9: (a) Plot showing the coarse-grained  $Q^{(1)}$  density profile at different times  $\tilde{t} = t/(2N)$ . (b) shows the evolution of the  $Q^{(1)}$  density with time at a fixed coarse-grained point  $y/(2N) \approx 0.30$ . The inset in (b) shows the same curve on a log-log scale but with the steady state value subtracted. We observe a  $\sim 1/\sqrt{t}$  decay at large times as expected from the analytical expressions. In both figures, the points are calculated by coarse-graining the microscopic  $Q^{(1)}$  density profile whereas the continuous lines are obtained from the analytic GHD expressions. We find an excellent agreement between the coarse-grained microscopic and the GHD results. The coarse-graining is done over  $\Delta = 8$  consecutive sites. The parameters used are  $\beta_1 = 0.25$ ,  $\beta_2 = 1.0$ ,  $\gamma_1 = 0.4$ ,  $\gamma_2 = 0.8$  and  $2N = 512$ .

between hydrodynamics and exact numerics.

We expect the final state to be a GGE state characterised by Lagrange multipliers  $\{\lambda_n\}$  which are related to the average densities as

$$\rho_{GGE}^{(n)} = \int_{-\pi}^{\pi} \frac{dk}{2\pi} \frac{\cos nk}{\sum_{m=0}^{\infty} \lambda_m \cos mk}. \quad (3.75)$$

The expression in Eq. (3.75) can be easily inverted using the Fourier cosine series and we obtain the following explicit expressions for the Lagrange multipliers of the finite chain

$$\lambda_0 = \frac{1}{2\pi} \int_0^{\pi} dk \frac{1}{f(k)}, \quad (3.76a)$$

$$\lambda_n = \frac{1}{\pi} \int_0^{\pi} dk \frac{\cos nk}{f(k)} \quad \text{for } n > 1, \quad (3.76b)$$

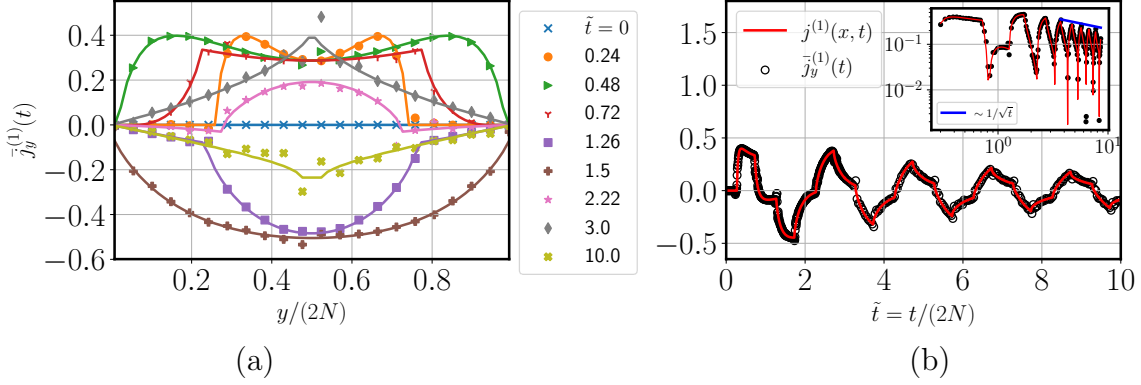


Figure 3.10: (a) Plot showing the coarse-grained  $Q^{(1)}$  current density profile at different times  $\tilde{t} = t/(2N)$ . (b) shows the evolution of the  $Q^{(1)}$  current density with time at a fixed coarse-grained point  $y/(2N) \approx 0.23$ . The inset in (b) shows the same curve on a log-log scale. We observe a  $\sim 1/\sqrt{t}$  decay at large times as expected from the analytical expressions. In both figures, the points are calculated by coarse-graining the microscopic  $Q^{(1)}$  current density profile whereas the continuous lines are obtained from the analytic GHD expressions. We find an excellent agreement between the coarse-grained microscopic and the GHD results. The coarse-graining is done over  $\Delta = 8$  consecutive sites. The parameters used are  $\beta_1 = 0.25, \beta_2 = 1.0, \gamma_1 = 0.4, \gamma_2 = 0.8$  and  $2N = 512$ .

where  $f(k)$  is given by

$$f(k) = \frac{1}{2}\rho_{GGE}^{(0)} + \sum_{n=1}^{\infty} \rho_{GGE}^{(n)} \cos nk. \quad (3.77)$$

Putting the values of the conserved densities from Eq. (3.71) into Eq. (3.76), we can compute the  $\{\lambda_n\}$  in the final state. In Fig. (3.11), we plot the stationary state density and the absolute values of the Lagrange multipliers on a log-linear scale. Unlike the case where the initial state is composed of two GEs, here we find that all densities and Lagrange multipliers are non-zero in the final state. However, both quantities decay exponentially for large  $n$ . Note that Eqs. (3.75)-(3.77) are valid even if the initial state is described by a product of two GGEs with an arbitrary number of nonzero parameters that have unequal values in the two halves of the chain. It is important to point out that these results are specific to the harmonic lattice due to the linear nature of interactions and the quadratic nature of the distributions involved, and may not hold for systems with non-linear interactions.

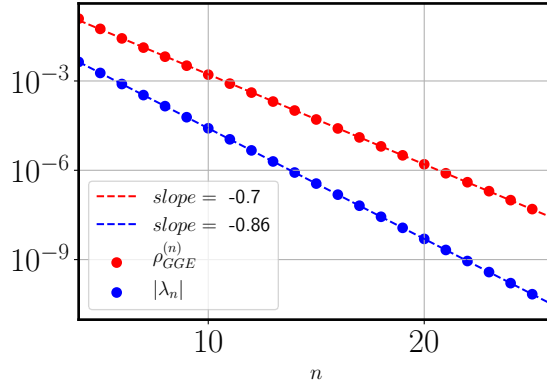


Figure 3.11: Plot showing exponential decay of the densities  $\rho_{GGE}^{(n)}$  and the absolute values of the Lagrange multipliers  $\lambda_n$  with increasing  $n$ . The points in red are calculated using Eq. (3.71) whereas the blue points are evaluated using Eq. (3.76). The dashed lines show an exponential fit to the data points. The parameters used are  $\beta_1 = 0.25, \beta_2 = 1.0, \gamma_1 = 0.4, \gamma_2 = 0.8$ .

### 3.4 Discussions and summary

In this work, we first provided a physically motivated derivation of the generalized hydrodynamics of a classical harmonic chain, based on the approach of the Wigner function. Our work thus makes connections between earlier work on harmonic chains [46, 48, 50, 51] with the recent developments in GHD. As an application, we studied the problem of thermalization of a harmonic chain starting from domain wall initial conditions.

Specifically, we studied the evolution of a classical harmonic chain with nearest-neighbor interactions starting from a domain wall initial state composed of either two GEs or two GGEs with unequal chemical potentials in the left and right halves of the chain. For each type of the initial distribution, we study both finite and infinite chains. In all cases, we found excellent agreement, at all times, between results from hydrodynamics with those obtained from exact numerics. We observe that a finite chain relaxes as  $\sim 1/\sqrt{t}$  to a steady state that is expected to be described by a GE or a GGE depending on whether we use the GE or GGE type of initial condition. For the GGE initial condition, the final state is also expected to be a GGE characterized by a set of Lagrange multipliers which we evaluate exactly in terms of the steady state densities. We find that this GGE steady state has an infinite number of Lagrange parameters with exponentially

decaying strengths. All currents decay to zero as  $\sim 1/\sqrt{t}$  as we approach the steady state due to reflections at the boundaries. For the case of an infinite chain, we find that even for the initial condition composed of two GEs, any finite region of the system tends, in the  $t \rightarrow \infty$  limit, towards a non-equilibrium steady state (NESS) in which the currents have nonzero but constant values. The NESS in the infinite chain is therefore expected to be a current-carrying GGE. The relaxation to this NESS happens as  $\sim 1/t$  for the densities and as  $\sim 1/t^2$  for the currents.

We note that the Wigner GHD equation is applicable for generic harmonic systems incorporating more complex force matrices in arbitrary dimensions and quantum statistics. These can be interesting extensions of the present work. For the quantum case, the computation of entanglement entropy in free fermionic systems using semiclassical hydrodynamics has generated a lot of interest [85, 86] and it would be of great interest to explore this in the context of quantum harmonic crystals. Another interesting open question would be to prove or demonstrate equilibration in the harmonic chain for a single realization that starts from an arbitrary initial condition. This has recently been proved [87] in the quantum case for non-interacting fermions while for a classical ideal gas, it has been established for initial conditions chosen from continuous distributions [22].



# Chapter 4

## Conclusions

In this thesis, we have investigated the possibility of thermalization and the applicability of hydrodynamics to non-interacting integrable systems. In chapter (2), we studied the Joule expansion of an ideal quantum gas on a circle, starting from an initial pure state that was confined to a part of the circle. Building upon the work done in [19] for the classical ideal gas, we considered two choices of macrovariables: the  $U$ -macrovariables and the  $f$ -macrovariables which correspond to coarse-graining in the real and phase space respectively. To define the  $U$ -macrostate, we divided the circle into a number of cells which are macroscopic themselves. The  $U$ -macrovariables are then the expectation values of the three conserved macroscopic fields: the total particle number, the total momentum, and the total energy. Although the ideal gas has an extensive number of conserved quantities, we chose to describe the macro-evolution in terms of these three usual hydrodynamic fields. While defining the  $U$ -macrostate for the quantum gas is very similar to the classical case, the  $f$ -macrostate is not that straightforward. This is because the classical  $f$ -macrostate in [19] was constructed by coarse-graining the single particle phase space and just counting the number of particles within each grid cell. This cannot be done for quantum gas due to the Heisenberg uncertainty principle. So we constructed a new basis, the wavepacket basis (see Eq. (2.37)), in which the basis states are localized in both position and momentum space, obeying the uncertainty principle. The expectation values of the occupation numbers in these new basis states are then used to define the  $f$ -macrovariables for the quantum gas.

To study the microscopic evolution of the quantum gas, we defined the Wigner dis-

tribution function (WDF) on the circle in Eq. (2.28). Note that the Wigner function can be negative and therefore cannot be interpreted as a probability density function. In the literature [78–82], the Husimi distribution and the Wehrl entropy have been used to study the irreversibility in interacting systems. However, it is an invertible transformation of the Wigner function and is therefore not suitable for our ideal gas. The wavepacket density on the other hand provides us with a coarse-grained Wigner function that can be used to define a non-trivial entropy function for the ideal gas.

For the  $U$ -macrostate, we found that the entropy grows monotonically and the curves converge as the coarse-graining scale is reduced [see Figs. (2.5, 2.10)]. This is because the  $U$ -macrovariables i.e. the number, momentum, and energy density fields actually attain their equilibrium values on the circle (subject to the constraints of the total particle number and the total energy). On the other hand, for the  $f$ -macrostate, the entropy is seen to have an oscillatory relaxation and the initial growth is proportional to the coarse-graining scale  $K$ . Thus, in the limit of  $K \rightarrow 0$ , the entropy does not grow. This is similar to the classical ideal gas [19] and is due to the fact that the momentum distribution for the ideal gas never evolves.

Many of the results in our study of the quantum ideal gas are similar to the classical case studied in [19]. However, there are striking differences as well and here we mention some of them.

- The  $f$ -macrostate observables for the quantum case are microscopic as the coarse-graining occurs on scales of  $\Delta x \Delta p \sim h$  where  $h$  is Planck's constant. For instance, the average occupation number for fermions,  $\langle \hat{n}_\alpha \rangle$ , are of order one.
- The change in the  $f$ -macrostate entropy per particle satisfies  $\log 2 \leq \Delta s_B^f \leq 2 \log 2$  for fermions, and  $0 \leq \Delta s_B^f \leq \log 2$  for bosons. The classical result is  $\log 2$  which is approached for both fermions and bosons in the high-temperature limit.
- The  $U$ -macrostate entropy for fermions in the low-temperature limit shows an initial flat region [see Fig. (2.5) (a)] which persists till time  $(L/4)/v_f$ , where  $L$  is the circle length and  $v_f$  is the Fermi velocity. This does not happen for the classical gas which is nothing but the high-temperature limit of the fermi gas.

At the same time, the many similarities between the classical and quantum ideal gases also indicate that the quantum statistics does not change much of the qualitative behavior of the relaxation to the steady state and the entropy. The study in [19] was extended to the case of an alternate mass hard particle gas (AMHPG) in [20] which is an interacting and non-integrable system. There it was found that the  $U$  and  $f$  macrostate entropies have identical curves and monotonic growth. In [21], the  $f$ -macrostate entropy is studied for 2-D hard rods and it was found that the growth curve has two parts. The first part, due to the free motion of the gas, has features similar to the ideal gas like the initial growth proportional to the coarse-graining scale and the oscillatory relaxation. The second part, which is due to the interparticle collisions, shows monotonic growth independent of the coarse-graining. This leads us to the conclusion that certain observables like particle and energy densities thermalize even in the absence of interactions. However, to observe thermalization and monotonic entropy growth irrespective of the choice of macrovariables, interactions do play a vital role. It would be interesting to study a weakly interacting quantum gas. However, this would be a highly entangled many-body system and thus very challenging to treat accurately.

In Chapter [3], we studied the other part of our thesis which was to check the applicability of generalized hydrodynamics (GHD) and approach to a generalized Gibbs ensemble (GGE) for the case of a non-interacting integrable model of a classical harmonic chain with nearest neighbor interactions. On intermediate scales of space and time, the evolution of integrable systems is expected to be described by the theory of generalized hydrodynamics (GHD) [42,45]. We decided to study the GHD evolution and approach to GGE for the classical harmonic chain due the following main reasons.

- The approach to GGE has been demonstrated mainly in quantum integrable models [28,36,41-44] and recently for the classical hard rods gas [38]. So it makes sense to explore more classical models in this context.
- A number of studies have established GHD for several interacting classical and quantum integrable systems such as Toda chain [54-57], the  $\delta$ -Bose gas [58] and hard rods [38,59]. Applicability of GHD to non-interacting systems however has not been widely explored. There are reasons, such as the possible absence of local

GGE, to believe that GHD may not apply to non-interacting systems. So it would be interesting to check its validity.

- For a non-interacting system such as the harmonic chain, the evolution is linear and thus a lot of quantities such as the conserved densities and the associated currents can be computed exactly using the GHD.
- In particular for the harmonic chain, two formalisms to study the macroscopic evolution can be found in literature: the correlation matrix method [46, 48] and the Wigner function method [67–70]. However, the connections between the two have not been elaborated in the physics literature. The connection to GHD also remained unexplored. So, we decided to elucidate these connections and work out the GHD in detail.

We studied the evolution of the harmonic chain starting from a Gaussian initial domain-wall state. The initial state composed of two Gibbs ensembles (GEs) (choice 1) is discussed in Sec. (3.3.1) while the one consisting of two generalized Gibbs ensembles (GGEs) (choice 2) is worked out in Sec. (3.3.2). For each type of the initial state, we studied both finite and infinite-length chains. We showed that the finite chain tends to a final expected GE or GGE depending on whether the initial state is composed of two GEs or two GGEs respectively. Both the conserved densities and the currents relax as  $\sim 1/\sqrt{t}$  to their respective equilibrium values. The currents all decay to zero due to reflections at the boundaries. For an infinite chain, both types of initial states lead to a final expected GGE state which is current carrying. Here, the densities and currents corresponding to the conserved quantities relax as  $\sim 1/t$  and  $\sim 1/t^2$  respectively. Starting from an arbitrary Gaussian initial domain-wall state, we were able to characterize the final expected GGE state completely by explicitly writing down its Lagrange multipliers in terms of the conserved quantities in Eqs. (3.76, 3.77). In [64], an infinite quantum harmonic chain was studied, and the final GGE state starting from an initial state composed of two GEs was explicitly evaluated. We can use the GHD formalism to reproduce that result while also studying the finite length case and the initial state composed of two GGEs. More interestingly, we can study the classical harmonic chain with long-range interactions and see if the GHD predictions hold against Hamiltonian evolution.

# Appendix A

## A.1 Marginals of the wavepacket density

Here we establish the fact mentioned in Sec. (2.4.2) that the marginals of the wave-packet density,  $D_\alpha$ , after integrating either over momentum or space, correspond respectively to the coarse-grained particle density and momentum density. Let us consider the momentum marginal first i.e. sum over  $r$

$$\begin{aligned}
 D_v(v, t) &= \sum_r D(r, v, t) = \sum_{r, m, n} \langle r, v | m \rangle \tilde{\rho}_1(p_m, p_n, t) \langle n | r, v \rangle \\
 &= \frac{1}{K} \sum_{r=1}^K \sum_{m, n \in \mathcal{R}_v} e^{2\pi i(m-n)r/K} \tilde{\rho}_1(p_m, p_n, t) \\
 &= \sum_{n \in \mathcal{R}_v} \tilde{\rho}_1(p_n, p_n, 0).
 \end{aligned} \tag{A.1}$$

Let us now consider the r-marginal i.e. sum over  $v$

$$D_r(r, t) = \sum_v D(r, v, t) = \int \frac{dx dx'}{LK} \sum_v \sum_{m, n \in \mathcal{R}_v} Q_{mn}(x, x', t), \tag{A.2}$$

$$Q_{mn}(x, x', t) = e^{2\pi i(-mx+nx')/L} e^{i(m-n)2\pi r/K} \rho_1(x, x', t). \tag{A.3}$$

Note that  $m, n \in \mathcal{R}_v$  which is given by

$$\mathcal{R}_v = \left\{ v - \frac{K-1}{2}, \dots, v + \frac{K-1}{2} \right\}. \tag{A.4}$$

We substitute  $m = v + \tilde{m}$  and  $n = v + \tilde{n}$  to get rid of the  $v$  dependence in the sums over

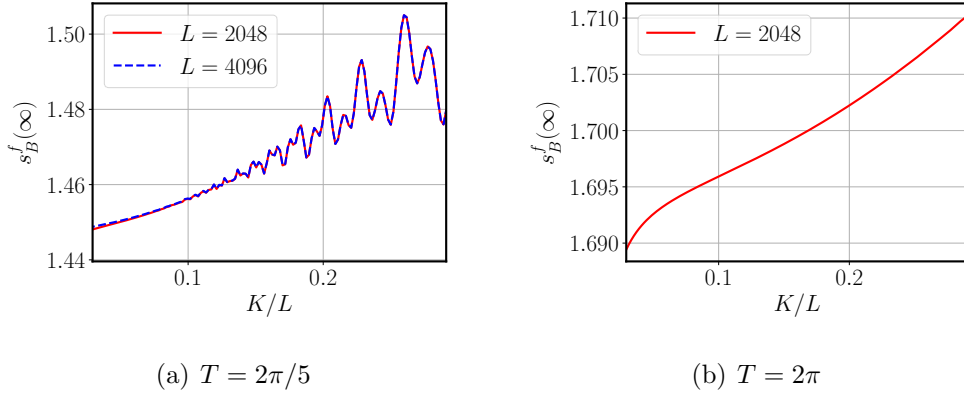


Figure A.1: **Fermions:** The late time value of the f-macrostate entropy per particle,  $s_B^f(\infty)$  as a function of the coarse-graining scale  $K$  for the low and intermediate temperatures. It seems that we require  $K/L \ll 1$  for the final value to not vary strongly with  $K$ . The variation also goes down with increasing temperature.

$m$  and  $n$ . We thus get

$$D_r(r, t) = \int \frac{dx dx'}{LK} \sum_v \sum_{\tilde{m}, \tilde{n} \in \mathcal{R}_0} e^{2\pi i v (x' - x)/L} Q_{\tilde{m}\tilde{n}}(x, x', t). \quad (\text{A.5})$$

Now since  $v$  takes values  $\vartheta K$  where  $\vartheta$  is an integer that runs from  $-\infty$  to  $+\infty$ , the sum over  $v$  can be done and gives

$$\begin{aligned} D_r(r, t) &= \int \frac{dx dx'}{K^2} \sum_{\tilde{m}, \tilde{n} \in \mathcal{R}_0} \delta(x - x') Q_{\tilde{m}\tilde{n}}(x, x', t) \\ &= \int_0^L \frac{dx}{K^2} \left| \sum_{\tilde{n} = -(K-1)/2}^{(K-1)/2} \exp\left[2\pi i \tilde{n} \left(\frac{x}{L} - \frac{r}{K}\right)\right] \right|^2 \rho_1(x, x, t) \\ &= \int_0^L dx h_K \left(\frac{x}{L} - \frac{r}{K}\right) n(x, t), \end{aligned} \quad (\text{A.6})$$

where  $n(x, t)$  is the particle density and  $h_K(x) = \frac{1}{K^2} \left(\frac{\sin \pi K z}{\sin \pi z}\right)^2$ .

## A.2 Maximizing the von Neumann entropy

In this section, we present a derivation for the formula of the maximal density matrix  $\hat{\rho}^*$  subject to the constraints  $\langle \hat{M}_k \rangle = \text{Tr}[\hat{\rho} \hat{M}_k]$  that does not require the operators to

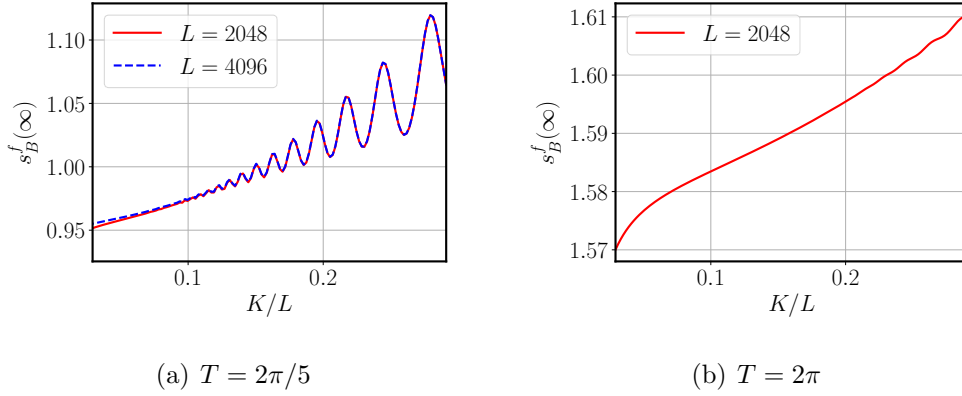


Figure A.2: **Bosons**: The late time value of the f-macrostate entropy per particle,  $s_B^f(\infty)$  as a function of the coarse-graining scale  $K$  for the low and intermediate temperatures. It seems that we require  $K/L \ll 1$  for the final value to not vary strongly with  $K$ . Also note that the variation with  $K$  is stronger for bosons as compared to fermions, so a relatively smaller  $K/L$  may be required for bosons. Here also, the variation goes down with increasing temperature.

commute. Consider a set of operators  $\hat{M}_k$ ;  $k = 1, 2, 3, \dots$  and a density matrix  $\hat{\rho}$  such that

$$\langle \hat{M}_k \rangle = \text{Tr}[\hat{\rho} \hat{M}_k] \quad (\text{A.7})$$

We want to construct a density matrix  $\hat{\rho}^*$  with maximal Von-Neumann entropy,  $S[\hat{\rho}] = -\text{Tr}[\hat{\rho} \ln \hat{\rho}]$ , subject to the constraints that the expectation values of all  $\hat{M}_k$  are given by some fixed values  $M_k$ . We start by writing down the functional to maximize with the corresponding Lagrange multipliers  $\lambda_k$  for each constraint  $\langle \hat{M}_k \rangle = M_k$

$$\mathcal{S}[\hat{\rho}] = -\text{Tr}[\hat{\rho} \ln \hat{\rho}] - \sum_k \lambda_k \left( \langle \hat{M}_k \rangle - M_k \right) - \lambda_0 (\text{Tr}[\hat{\rho}] - 1) \quad (\text{A.8})$$

Now given a Hermitian operator  $\hat{O}$ , we can define the following identity for any function of  $\hat{O}$

$$f(\hat{O}) = \frac{1}{2\pi i} \int_C dz \frac{f(z)}{z - \hat{O}} \quad (\text{A.9})$$

where the contour  $C$  encloses all eigenvalues of  $\hat{O}$ . Using Eq.(A.9), we can write

$$\hat{\rho} \ln \hat{\rho} = \frac{1}{2\pi i} \int_C dz \frac{z \ln z}{z - \hat{\rho}} \quad (\text{A.10})$$

Substituting Eq. (A.10) in Eq. (A.8), we get

$$\mathcal{S}[\hat{\rho}] = -\text{Tr} \left[ \frac{1}{2\pi i} \int_C dz \frac{z \ln z}{z - \hat{\rho}} + \sum_k \lambda_k \hat{M}_k \hat{\rho} + \lambda_0 \hat{\rho} \right] + \sum_k \lambda_k M_k + 1 \quad (\text{A.11})$$

Varying the entropy in Eq. (A.11) w.r.t  $\hat{\rho}$  yields

$$\delta \mathcal{S}[\hat{\rho}] = -\text{Tr} \left[ \left( \frac{1}{2\pi i} \int_C dz \frac{z \ln z}{(z - \hat{\rho})^2} + \sum_k \lambda_k \hat{M}_k + \lambda_0 \right) \delta \hat{\rho} \right] \quad (\text{A.12})$$

From Eq. (A.12), we see that the density matrix,  $\hat{\rho}^*$ , which maximises the entropy subject to the constraints, satisfies

$$\frac{1}{2\pi i} \int_C dz \frac{z \ln z}{(z - \hat{\rho}^*)^2} = -\sum_k \lambda_k \hat{M}_k - \lambda_0 \quad (\text{A.13})$$

The integral in Eq. (A.13) can be evaluated by noting that it has second-order poles at the eigenvalues of  $\hat{\rho}^*$ , and therefore we obtain

$$\ln \hat{\rho}^* + 1 = -\sum_k \lambda_k \hat{M}_k - \lambda_0 \quad (\text{A.14})$$

$$\hat{\rho}^* = \frac{1}{Z} \exp \left( -\sum_k \lambda_k \hat{M}_k \right); \quad Z = \text{Tr} \left[ \exp \left( -\sum_k \lambda_k \hat{M}_k \right) \right] \quad (\text{A.15})$$

The constant  $\lambda_0 - 1$  is absorbed in the normalization  $Z$ . This is the desired result for the density matrix. The Lagrange multipliers are fixed by the constraint equations.

### A.3 Dependence on $K$

Here we briefly discuss the dependence of our results on the coarse-graining parameter  $K$ .

**Fermions:** In Fig. (A.1), we plot the saturation value  $s_B^f(\infty)$  for different  $K$  and for the low and intermediate temperatures. We observe that as long as  $K \ll L$ , the saturation value does not vary strongly with  $K$ . Also, the variation becomes smaller with increasing temperature.

**Bosons:** The strong dependence on  $K$  can be understood from Fig. (A.2) which shows the variation of the saturation value of the f-macrostate entropy per particle with  $K$ . Here, we can clearly see that the variation is stronger for bosons as compared to fermions. As a result, the  $K$  values used in our numerical study are not small enough compared to the system size  $L$  for bosons, especially in the low-temperature case.

## A.4 Glossary

- $f, U$ : denote the two macrovariables studied in this work.
- $S_B^f, S_B^U$ : the Boltzmann entropies corresponding to the two macrovariables.
- $s_B^f, s_B^U$ : Boltzmann entropies per particle.
- $X$ : Phase space point.
- $|\Phi\rangle$ : Pure state wavefunction.
- $N, E, L$ : The total number of particles, the total energy, and the system size (Circle perimeter) respectively.
- $T, \beta, \mu$ : The temperature, the inverse temperature, and the chemical potential respectively.
- $a$ : Fraction of the circle occupied by the gas at time  $t = 0$ . In most cases  $a = 1/2$ .
- $m$ : Mass of the particles.
- $\mathcal{H}$ : Hilbert space.
- $\mathcal{H}_E$ : Subspace of the full Hilbert space corresponding to the energy  $E$ .
- $\hat{M}_k$ : Generic self-adjoint operators.
- $\nu, \mathcal{H}_\nu$ : Generic macrostate and the corresponding macro-space.
- $|\mathcal{H}_\nu|$ : Denotes the dimension of the  $\mathcal{H}_\nu$  macro-space.
- $\hat{P}_\nu$ : Projection operator onto the  $\mathcal{H}_\nu$  macro-space.

- $S_\nu$ : Boltzmann entropy corresponding to the  $\nu$  macrostate.
- $\mathcal{H}_{eq}$ : Equilibrium macro-space.
- $\hat{\rho}_{GC}, Z_{GC}$ : Generalized canonical density operator and the corresponding partition function.
- $\lambda_k$ : Lagrange multipliers (for satisfying the constraints) in the expression for  $\hat{\rho}_{GC}$ .
- $S_{GvN}$ : The Gibbs-von Neumann entropy of the system
- $\delta, A$ : Denote the size and number respectively of the coarse-grained cells in the  $U$ -macrostate.
- $\ell$ : Labels the coarse-grained cells in the  $U$ -macrostate.
- $\hat{N}_\ell, \hat{P}_\ell, \hat{E}_\ell$ : Denote the particle number, the momentum, and the energy operators respectively corresponding to the  $\ell^{\text{th}}$  cell in the  $U$ -macrostate.
- $K$ : Denotes the coarse-graining scale in the  $f$ -macrostate.
- $|\psi_\alpha\rangle \equiv |r, v\rangle$ : The wavepacket basis state localized in position around  $x = rL/K$  and in momentum around  $p = 2\pi\hbar v/L$ .
- $\hat{n}_\alpha, D_\alpha(t) \equiv D(r, v, t)$ : Denote the occupation number operator and the average occupancy (wavepacket density) respectively of the wavepacket basis state  $|\psi_\alpha\rangle$ .
- $|\chi_s\rangle, e_s, n_s$ : Denote the box energy eigenfunction, eigenvalue, and occupancy of the  $s^{\text{th}}$  level respectively.
- $|\varphi_n\rangle, p_n, \epsilon_n$ : Denote the circle energy eigenfunction, momentum, and energy eigenvalue of the  $n^{\text{th}}$  level respectively.
- $\hat{\Psi}_x, \hat{b}_n$ : Denote the annihilation operator in the position and in momentum space respectively.
- $\hat{\rho}_N$ : The  $N$ -particle density operator.
- $\hat{\rho}_1, \rho_1(x, x'), \tilde{\rho}_1(p_m, p_n)$ : The single-particle density operator and its matrix elements in the position and momentum space respectively.

- $V$ : Transformation matrix from the box to the circle basis.
- $f(e_s, \beta, \mu)$ : Denotes the Fermi/Bose function.
- $\hat{\rho}_1^P, \hat{\rho}_1^M$ : Denote the single-particle density operator corresponding to the pure and mixed state initial conditions respectively.
- $P(\{n_s\})$ : Denotes the grand canonical probability distribution of the configuration  $\{n_s\}$ .
- $w(x, p, t)$ : The Wigner function on the real line.
- $q_n$ : Denotes the half-integer momenta on the circle.
- $w(x, q_n, t)$ : The Wigner function on the circle.
- $\hat{N}, \hat{P}, \hat{E}$ : Denote the total particle number, the total momentum, and the total energy operators respectively.
- $\hat{n}(x, t), \hat{p}(x, t), \hat{e}(x, t)$ : Denote the local particle, momentum, and energy density operators respectively.
- $n(x, t), p(x, t), e(x, t)$ : Denote the expectation values of the local particle, momentum, and energy density operators respectively.
- $\mathcal{R}_v$ : The set of  $K$  integers centered around  $v$ .
- $v_{\pm}$ : The two end points of the set  $\mathcal{R}_v$ .
- $G_K(q, x)$ : The localized kernel that, when integrated over the Wigner function, yields the wavepacket density.
- $D_r(r, t), D_v(v, t)$ : The respective marginals of  $D(r, v, t)$ .
- $h_K(x)$ : The localized kernel that, when integrated with the particle density  $n(x, t)$ , yields the coarse-grained marginal  $D_r(r, t)$ .
- $\hat{\rho}_N^*$ : Maximal  $N$ -particle density operator subject to the wavepacket density constraints.

- $\lambda_\alpha$ : Lagrange multipliers (for satisfying the constraints) in the expression for  $\hat{\rho}_N^*$ .
- $\Delta s_B^f, \Delta s_B^U$ : The final change in the entropies of  $f$  and  $U$  macrostates respectively.
- $\rho$ : Particle density  $N/L$ .
- $\lambda_{\text{th}}$ : The thermal De-Broglie wavelength.
- $\tau_p$ : The period of oscillations of the particle density.
- $v_f$ : Fermi velocity.
- $\tau$ : The period of oscillations of the Boltzmann entropy  $S_B^f$ .
- $\tau_{\text{rec}}$ : The recurrence period.

# Appendix B

## B.1 GGE partition function

The GGE partition function in Eq. (3.7) is given by the integral

$$\begin{aligned}
 Z(\{\lambda_n\}) &:= \int_{-\infty}^{\infty} \prod_{j=1}^N dp_j dq_j \exp \left( - \sum_{n=0}^{N-1} \lambda_n Q^{(n)}(\mathbf{p}, \mathbf{q}) \right) \\
 &= \int_{-\infty}^{\infty} \prod_{j=1}^N dp_j dq_j \exp \left( - \frac{1}{2} \left[ \mathbf{p}^T \sum_n \lambda_n B^{(n)} \mathbf{p} + \mathbf{q}^T \sum_n \lambda_n M^{(n)} \mathbf{q} \right] \right)
 \end{aligned} \tag{B.1}$$

where we have used the expression for  $Q^{(n)}$  in Eq. (3.34) and the Lagrange multipliers are chosen such that  $\sum_n \lambda_n B_n$  and  $\sum_n \lambda_n M_n$  are positive definite matrices. The Gaussian integration can be easily performed once we know the eigenvalues of  $B^{(n)}$  and  $M^{(n)}$  matrices which are respectively given by  $\cos(nk_\ell)$  and  $\omega_{k_\ell}^2 \cos(nk_\ell)$  with  $k_\ell = \frac{\pi \ell}{N+1}$ ,  $\ell = 1, \dots, N$  and  $\omega_k^2 = 2(1 - \cos k)$ . We therefore get

$$Z(\{\lambda_n\}) = \sqrt{\frac{(2\pi)^N}{\prod_{\ell=1}^N \left( \sum_{n=0}^{N-1} \lambda_n \cos(nk_\ell) \right)}} \times \sqrt{\frac{(2\pi)^N}{\prod_{\ell=1}^N \omega_{k_\ell}^2 \left( \sum_{n=0}^{N-1} \lambda_n \cos(nk_\ell) \right)}}, \tag{B.2}$$

which can be simplified to yield Eq. (3.8).

## B.2 Density evolution corresponding to the initial condition composed of two GGEs

Here we show the steps leading to the density profiles in Eq. (3.59) starting from the expression for the Wigner function in Eq. (3.58). Substituting the Wigner function from Eq. (3.58) into Eq. (3.37), we obtain the following expression for  $\rho^{(n)}(x, t)$

$$\rho^{(n)}(x, t) = 2 \int_0^{\pi/2} \frac{d\theta}{\pi} \cos 2n\theta \frac{1}{\beta_1(1 - \gamma_1 \cos 2\theta)} - I^{(n)}(x, t) = g^{(n)}(\beta_1, \gamma_1) - I^{(n)}(x, t), \quad (\text{B.3})$$

where  $g^{(n)}(\beta, \gamma)$  is defined in Eq. (3.60) and  $I^{(n)}(x, t)$  is given by

$$I^{(n)}(x, t) = \int_0^{\pi/2} \frac{d\theta}{\pi} \cos 2n\theta \left( \frac{1}{\beta_1(1 - \gamma_1 \cos 2\theta)} - \frac{1}{\beta_2(1 - \gamma_2 \cos 2\theta)} \right) [\Theta(x - t \cos \theta) + \Theta(x + t \cos \theta)]. \quad (\text{B.4})$$

Differentiating Eq. (B.4) w.r.t  $x$  on both sides and simplifying yields

$$\frac{\partial I^{(n)}}{\partial x} = \frac{\cos 2n\theta^*}{\pi t \sin \theta^*} \left( \frac{1}{\beta_1(1 - \gamma_1 \cos 2\theta^*)} - \frac{1}{\beta_2(1 - \gamma_2 \cos 2\theta^*)} \right), \quad |x| < t \quad (\text{B.5})$$

where  $\theta^* = \cos^{-1}(|x|/t)$ . Integrating Eq. (B.5) w.r.t  $x$  gives

$$I^{(n)}(x, t) = \begin{cases} 0, & x < -t \\ \int_0^{\pi/2} \frac{d\theta}{\pi} \cos 2n\theta \left( \frac{1}{\beta_1(1 - \gamma_1 \cos 2\theta)} - \frac{1}{\beta_2(1 - \gamma_2 \cos 2\theta)} \right) \\ + \int_0^{\sin^{-1}(x/t)} \frac{d\theta}{\pi} \cos\{2n \cos^{-1} |\sin \theta|\} \left( \frac{1}{\beta_1(1 + \gamma_1 \cos 2\theta)} - \frac{1}{\beta_2(1 + \gamma_2 \cos 2\theta)} \right), & |x| < t \\ 2 \int_0^{\pi/2} \frac{d\theta}{\pi} \cos 2n\theta \left[ \left( \frac{1}{\beta_1(1 - \gamma_1 \cos 2\theta)} - \frac{1}{\beta_2(1 - \gamma_2 \cos 2\theta)} \right) \right], & x > t \end{cases} \quad (\text{B.6})$$

Using Eq. (3.60), we can rewrite Eq. (B.6) as

$$I^{(n)}(x, t) = \begin{cases} 0, & x < -t \\ \frac{1}{2} [g^{(n)}(\beta_1, \gamma_1) - g^{(n)}(\beta_2, \gamma_2)] \\ + \int_0^{\sin^{-1}(x/t)} \frac{d\theta}{\pi} \cos\{2n \cos^{-1} |\sin \theta|\} \left( \frac{1}{\beta_1(1 + \gamma_1 \cos 2\theta)} - \frac{1}{\beta_2(1 + \gamma_2 \cos 2\theta)} \right), & |x| < t \\ g^{(n)}(\beta_1, \gamma_1) - g^{(n)}(\beta_2, \gamma_2), & x > t \end{cases} \quad (\text{B.7})$$

Substituting Eq. (B.7) into Eq. (B.3) gives us the required expression in Eq. (3.59).



# Bibliography

- [1] L. D'Alessio, Y. Kafri, A. Polkovnikov, and M. Rigol, "From quantum chaos and eigenstate thermalization to statistical mechanics and thermodynamics," *Advances in Physics*, vol. 65, no. 3, pp. 239–362, 2016.
- [2] V. Allori, *Statistical Mechanics and Scientific Explanation: Determinism, Indeterminism and Laws of Nature*. WORLD SCIENTIFIC, Aug. 2019.
- [3] O. E. Lanford, "Entropy and equilibrium states in classical statistical mechanics," in *Statistical mechanics and mathematical problems*, pp. 1–113, Springer, 2007.
- [4] H. Poincaré, "On the three-body problem and the equations of dynamics," *Acta Math*, vol. 13, no. 1, 1890.
- [5] H. B. Callen, "Thermodynamics and an introduction to thermostatistics," 1998.
- [6] L. Boltzmann, "On Zermelo's paper "On the mechanical explanation of irreversible processes",", *Annalen der Physik*, vol. 60, pp. 392–398, 1897.
- [7] R. Feynman, *The Character of Physical Law, with new foreword*. MIT press, 2017.
- [8] O. E. Lanford, "On a derivation of the boltzmann equation," *Astérisque*, vol. 40, no. 117, pp. 0353–70020, 1976.
- [9] R. Penrose and N. D. Mermin, "The emperor's new mind: Concerning computers, minds, and the laws of physics," 1990.
- [10] B. Greene, *The fabric of the cosmos: Space, time, and the texture of reality*. Knopf, 2004.

- [11] J. L. Lebowitz, “Macroscopic laws, microscopic dynamics, time’s arrow and boltzmann’s entropy,” *Physica A: Statistical Mechanics and its Applications*, vol. 194, no. 1-4, pp. 1–27, 1993.
- [12] J. L. Lebowitz, “Boltzmann’s entropy and time’s arrow,” *Physics Today*, vol. 46, no. 9, p. 32, 1993.
- [13] S. Goldstein and J. L. Lebowitz, “On the (Boltzmann) entropy of non-equilibrium systems,” *Physica D*, vol. 193, no. 1, p. 53, 2004.
- [14] R. Griffiths, “Statistical irreversibility: classical and quantum.,” *Physical origins of time asymmetry*, pp. 147–159, 1994.
- [15] S. Goldstein, D. A. Huse, J. L. Lebowitz, and R. Tumulka, “Macroscopic and microscopic thermal equilibrium,” *Annalen der Physik*, vol. 529, no. 7, p. 1600301, 2017.
- [16] H. Tasaki, “Typicality of thermal equilibrium and thermalization in isolated macroscopic quantum systems,” *Journal of Statistical Physics*, vol. 163, no. 5, pp. 937–997, 2016.
- [17] T. Mori, T. N. Ikeda, E. Kaminishi, and M. Ueda, “Thermalization and prethermalization in isolated quantum systems: a theoretical overview,” *Journal of Physics B: Atomic, Molecular and Optical Physics*, vol. 51, no. 11, p. 112001, 2018.
- [18] W. De Roeck, C. Maes, and K. Netočný, “Quantum macrostates, equivalence of ensembles, and an h-theorem,” *Journal of mathematical physics*, vol. 47, no. 7, p. 073303, 2006.
- [19] S. Chakraborti, A. Dhar, S. Goldstein, A. Kundu, and J. L. Lebowitz, “Entropy growth during free expansion of an ideal gas,” *Journal of Physics A: Mathematical and Theoretical*, vol. 55, no. 39, p. 394002, 2022.
- [20] S. Chakraborti, A. Dhar, and A. Kundu, “Boltzmann’s entropy during free expansion of an interacting gas,” *Journal of Statistical Physics*, vol. 190, no. 4, p. 74, 2023.

- [21] P. L. Garrido, S. Goldstein, D. A. Huse, and J. L. Lebowitz, “Time evolution of the boltzmann entropy for a nonequilibrium dilute gas,” *Journal of Statistical Physics*, vol. 191, no. 8, p. 92, 2024.
- [22] S. De Bievre and P. E. Parris, “A rigorous demonstration of the validity of Boltzmann’s scenario for the spatial homogenization of a freely expanding gas and the equilibration of the Kac ring,” *Journal of Statistical Physics*, vol. 168, pp. 772–793, 2017.
- [23] S. Pandey, J. M. Bhat, A. Dhar, S. Goldstein, D. A. Huse, M. Kulkarni, A. Kundu, and J. L. Lebowitz, “Boltzmann entropy of a freely expanding quantum ideal gas,” *Journal of Statistical Physics*, vol. 190, no. 8, p. 142, 2023.
- [24] D. S. Dean, P. Le Doussal, S. N. Majumdar, and G. Schehr, “Wigner function of noninteracting trapped fermions,” *Phys. Rev. A*, vol. 97, p. 063614, Jun 2018.
- [25] M. Kulkarni, G. Mandal, and T. Morita, “Quantum quench and thermalization of one-dimensional fermi gas via phase-space hydrodynamics,” *Phys. Rev. A*, vol. 98, p. 043610, Oct 2018.
- [26] V. Eisler and Z. Rácz, “Full counting statistics in a propagating quantum front and random matrix spectra,” *Physical review letters*, vol. 110, no. 6, p. 060602, 2013.
- [27] S. Scopa, A. Krajenbrink, P. Calabrese, and J. Dubail, “Exact entanglement growth of a one-dimensional hard-core quantum gas during a free expansion,” *Journal of Physics A: Mathematical and Theoretical*, vol. 54, no. 40, p. 404002, 2021.
- [28] L. F. Santos, A. Polkovnikov, and M. Rigol, “Entropy of isolated quantum systems after a quench,” *Phys. Rev. Lett.*, vol. 107, p. 040601, Jul 2011.
- [29] E. Solano-Carrillo and A. Millis, “Theory of entropy production in quantum many-body systems,” *Physical Review B*, vol. 93, no. 22, p. 224305, 2016.
- [30] D. Šafránek, J. M. Deutsch, and A. Aguirre, “Quantum coarse-grained entropy and thermodynamics,” *Physical Review A*, vol. 99, no. 1, p. 010101, 2019.

- [31] D. Šafránek, J. Deutsch, and A. Aguirre, “Quantum coarse-grained entropy and thermalization in closed systems,” *Physical Review A*, vol. 99, no. 1, p. 012103, 2019.
- [32] D. Šafránek, A. Aguirre, and J. M. Deutsch, “Classical dynamical coarse-grained entropy and comparison with the quantum version,” *Phys. Rev. E*, vol. 102, p. 032106, Sep 2020.
- [33] D. Šafránek, A. Aguirre, J. Schindler, and J. M. Deutsch, “A brief introduction to observational entropy,” *Foundations of Physics*, vol. 51, oct 2021.
- [34] O. Darrigol and U. Frisch, “From newton’s mechanics to euler’s equations,” *Physica D: Nonlinear Phenomena*, vol. 237, no. 14-17, pp. 1855–1869, 2008.
- [35] O. Darrigol, “Between hydrodynamics and elasticity theory: the first five births of the navier-stokes equation,” *Archive for History of Exact Sciences*, vol. 56, no. 2, pp. 95–150, 2002.
- [36] M. Rigol, V. Dunjko, V. Yurovsky, and M. Olshanii, “Relaxation in a completely integrable many-body quantum system: an ab initio study of the dynamics of the highly excited states of 1d lattice hard-core bosons,” *Physical Review Letters*, vol. 98, no. 5, p. 050405, 2007.
- [37] N. Cocciaglia, A. Vulpiani, and G. Gradenigo, “Thermalization without chaos in harmonic systems,” *Physica A: Statistical Mechanics and its Applications*, vol. 601, p. 127581, 2022.
- [38] S. K. Singh, A. Dhar, H. Spohn, and A. Kundu, “Thermalization and hydrodynamics in an interacting integrable system: the case of hard rods,” *Journal of Statistical Physics*, vol. 191, no. 6, p. 66, 2024.
- [39] S. Ganapa, A. Apte, and A. Dhar, “Thermalization of local observables in the  $\alpha$ -FPUT chain,” *Journal of Statistical Physics*, vol. 180, no. 1, pp. 1010–1030, 2020.

- [40] N. Shiraishi and H. Tasaki, “Nature abhors a vacuum: A simple rigorous example of thermalization in an isolated macroscopic quantum system,” *Journal of Statistical Physics*, vol. 191, no. 7, p. 82, 2024.
- [41] P. Calabrese, F. H. Essler, and M. Fagotti, “Quantum quench in the transverse-field Ising chain,” *Physical Review Letters*, vol. 106, no. 22, p. 227203, 2011.
- [42] F. H. Essler, “A short introduction to generalized hydrodynamics,” *Physica A: Statistical Mechanics and its Applications*, p. 127572, 2022.
- [43] B. Pozsgay, “Quantum quenches and generalized Gibbs ensemble in a Bethe Ansatz solvable lattice model of interacting bosons,” *Journal of Statistical Mechanics: Theory and Experiment*, vol. 2014, no. 10, p. P10045, 2014.
- [44] B. Pozsgay and V. Eisler, “Real-time dynamics in a strongly interacting bosonic hopping model: global quenches and mapping to the XX chain,” *Journal of Statistical Mechanics: Theory and Experiment*, vol. 2016, no. 5, p. 053107, 2016.
- [45] B. Doyon, “Lecture notes on generalized hydrodynamics,” *SciPost Physics Lecture Notes*, p. 018, 2020.
- [46] R. Dobrushin, A. Pellegrinotti, Y. M. Suhov, and L. Triolo, “One-dimensional harmonic lattice caricature of hydrodynamics,” *Journal of Statistical Physics*, vol. 43, pp. 571–607, 1986.
- [47] A. Mielke, “Macroscopic behavior of microscopic oscillations in harmonic lattices via Wigner-Husimi transforms,” *Archive for Rational Mechanics and Analysis*, vol. 181, pp. 401–448, 2006.
- [48] R. Dobrushin, A. Pellegrinotti, Y. M. Suhov, and L. Triolo, “One-dimensional harmonic lattice caricature of hydrodynamics: second approximation,” *Journal of Statistical Physics*, vol. 52, pp. 423–439, 1988.
- [49] J. Percus, “Exact solution of kinetics of a model classical fluid,” *The Physics of Fluids*, vol. 12, no. 8, pp. 1560–1563, 1969.

- [50] C. Boldrighini, R. Dobrushin, and Y. M. Sukhov, “One-dimensional hard rod caricature of hydrodynamics,” *Journal of Statistical Physics*, vol. 31, pp. 577–616, 1983.
- [51] C. Boldrighini and Y. M. Suhov, “One-dimensional hard-rod caricature of hydrodynamics: “Navier–Stokes correction” for local equilibrium initial states,” *Communications in Mathematical Physics*, vol. 189, no. 2, pp. 577–590, 1997.
- [52] O. A. Castro-Alvaredo, B. Doyon, and T. Yoshimura, “Emergent hydrodynamics in integrable quantum systems out of equilibrium,” *Physical Review X*, vol. 6, no. 4, p. 041065, 2016.
- [53] B. Bertini, M. Collura, J. De Nardis, and M. Fagotti, “Transport in out-of-equilibrium XXZ chains: Exact profiles of charges and currents,” *Physical Review Letters*, vol. 117, no. 20, p. 207201, 2016.
- [54] H. Spohn, “Hydrodynamic equations for the Toda lattice,” *arXiv preprint arXiv:2101.06528*, 2021.
- [55] X. Cao, V. B. Bulchandani, and H. Spohn, “The GGE averaged currents of the classical Toda chain,” *Journal of Physics A: Mathematical and Theoretical*, vol. 52, no. 49, p. 495003, 2019.
- [56] G. Mazzuca, T. Grava, T. Kriecherbauer, K. T.-R. McLaughlin, C. B. Mendl, and H. Spohn, “Equilibrium spacetime correlations of the Toda lattice on the hydrodynamic scale,” *Journal of Statistical Physics*, vol. 190, no. 8, p. 149, 2023.
- [57] A. Kundu, “Integrable hydrodynamics of Toda chain: case of small systems,” *The European Physical Journal Special Topics*, pp. 1–10, 2023.
- [58] P. Ruggiero, P. Calabrese, B. Doyon, and J. Dubail, “Quantum generalized hydrodynamics,” *Physical Review Letters*, vol. 124, no. 14, p. 140603, 2020.
- [59] B. Doyon and H. Spohn, “Dynamics of hard rods with initial domain wall state,” *Journal of Statistical Mechanics: Theory and Experiment*, vol. 2017, no. 7, p. 073210, 2017.

- [60] J.-S. Caux, B. Doyon, J. Dubail, R. Konik, and T. Yoshimura, “Hydrodynamics of the interacting Bose gas in the Quantum Newton Cradle setup,” *SciPost Physics*, vol. 6, no. 6, p. 070, 2019.
- [61] M. Schemmer, I. Bouchoule, B. Doyon, and J. Dubail, “Generalized hydrodynamics on an atom chip,” *Physical Review Letters*, vol. 122, no. 9, p. 090601, 2019.
- [62] X. Cao, V. B. Bulchandani, and J. E. Moore, “Incomplete thermalization from trap-induced integrability breaking: Lessons from classical hard rods,” *Physical Review Letters*, vol. 120, no. 16, p. 164101, 2018.
- [63] N. Malvania, Y. Zhang, Y. Le, J. Dubail, M. Rigol, and D. S. Weiss, “Generalized hydrodynamics in strongly interacting 1d Bose gases,” *Science*, vol. 373, no. 6559, pp. 1129–1133, 2021.
- [64] V. Eisler and Z. Zimborás, “Entanglement negativity in the harmonic chain out of equilibrium,” *New Journal of Physics*, vol. 16, no. 12, p. 123020, 2014.
- [65] T. Dudnikova, A. Komech, and H. Spohn, “On the convergence to statistical equilibrium for harmonic crystals,” *Journal of Mathematical Physics*, vol. 44, no. 6, pp. 2596–2620, 2003.
- [66] C. Boldrighini, A. Pellegrinotti, and L. Triolo, “Convergence to stationary states for infinite harmonic systems,” *Journal of Statistical Physics*, vol. 30, pp. 123–155, 1983.
- [67] H. Spohn, “The phonon boltzmann equation, properties and link to weakly anharmonic lattice dynamics,” *Journal of Statistical Physics*, vol. 124, pp. 1041–1104, 2006.
- [68] T. Komorowski, S. Olla, L. Ryzhik, and H. Spohn, “High frequency limit for a chain of harmonic oscillators with a point Langevin thermostat,” *Archive for Rational Mechanics and Analysis*, vol. 237, pp. 497–543, 2020.
- [69] T. Dudnikova and H. Spohn, “Local stationarity for lattice dynamics in the harmonic approximation,” *arXiv preprint math-ph/0505031*, 2005.

- [70] C. Bernardin, F. Huvneers, and S. Olla, “Hydrodynamic limit for a disordered harmonic chain,” *Communications in Mathematical Physics*, vol. 365, pp. 215–237, 2019.
- [71] S. Pandey, A. Dhar, and A. Kundu, “Generalized hydrodynamics and approach to generalized gibbs equilibrium for a classical harmonic chain,” *Journal of Statistical Mechanics: Theory and Experiment*, vol. 2024, p. 103202, oct 2024.
- [72] E. Fick, G. Sauermann, and W. D. Brewer, *The quantum statistics of dynamic processes*, vol. 86. Springer, 1990.
- [73] E. Wigner, “On the quantum correction for thermodynamic equilibrium,” *Phys. Rev.*, vol. 40, pp. 749–759, Jun 1932.
- [74] M. Hillery, R. F. O’Connell, M. O. Scully, and E. P. Wigner, “Distribution functions in physics: Fundamentals,” *Physics reports*, vol. 106, no. 3, pp. 121–167, 1984.
- [75] N. Mukunda, “Algebraic aspects of the wigner distribution in quantum mechanics,” *Pramana*, vol. 11, no. 1, pp. 1–15, 1978.
- [76] N. Mukunda, “Wigner distribution for angle coordinates in quantum mechanics,” *American Journal of Physics*, vol. 47, no. 2, pp. 182–187, 1979.
- [77] M. V. Berry, “Semi-classical mechanics in phase space: a study of wigner’s function,” *Philosophical Transactions of the Royal Society of London. Series A, Mathematical and Physical Sciences*, vol. 287, no. 1343, pp. 237–271, 1977.
- [78] K. Husimi, “Some formal properties of the density matrix,” *Proceedings of the Physico-Mathematical Society of Japan. 3rd Series*, vol. 22, no. 4, pp. 264–314, 1940.
- [79] A. Wehrl, “On the relation between classical and quantum-mechanical entropy,” *Reports on Mathematical Physics*, vol. 16, no. 3, pp. 353–358, 1979.
- [80] H. Tsukiji, H. Iida, T. Kunihiro, A. Ohnishi, and T. T. Takahashi, “Entropy production from chaoticity in yang-mills field theory with use of the husimi function,” *Physical Review D*, vol. 94, no. 9, p. 091502, 2016.

- [81] T. Kunihiro, B. Müller, A. Ohnishi, and A. Schäfer, “Towards a theory of entropy production in the little and big bang,” *Progress of theoretical physics*, vol. 121, no. 3, pp. 555–575, 2009.
- [82] B. O. Goes, G. T. Landi, E. Solano, M. Sanz, and L. Céleri, “Wehrl entropy production rate across a dynamical quantum phase transition,” *Physical Review Research*, vol. 2, no. 3, p. 033419, 2020.
- [83] D. S. Dean, P. Le Doussal, S. N. Majumdar, and G. Schehr, “Nonequilibrium dynamics of noninteracting fermions in a trap,” *EPL (Europhysics Letters)*, vol. 126, no. 2, p. 20006, 2019.
- [84] M. Simoncelli, N. Marzari, and F. Mauri, “Wigner formulation of thermal transport in solids,” *Physical Review X*, vol. 12, no. 4, p. 041011, 2022.
- [85] B. Bertini, M. Fagotti, L. Piroli, and P. Calabrese, “Entanglement evolution and generalized hydrodynamics: noninteracting systems,” *Journal of Physics A: Mathematical and Theoretical*, vol. 51, no. 39, p. 39LT01, 2018.
- [86] M. Saha, M. Kulkarni, and A. Dhar, “Generalized hydrodynamic description of the page curve–like dynamics of a freely expanding fermionic gas,” *Physical Review Letters*, vol. 133, no. 23, p. 230402, 2024.
- [87] H. Tasaki, “Macroscopic Irreversibility in Quantum Systems: ETH and Equilibration in a Free Fermion Chain,” *arXiv preprint arXiv:2401.15263*, 2024.



# Publications

- **List of publications included in the thesis:**

1. Saurav Pandey, Abhishek Dhar and Anupam Kundu, Generalized hydrodynamics and approach to generalized Gibbs equilibrium for a classical harmonic chain, [J. Stat. Mech. 103202 \(2024\)](#).
2. Saurav Pandey, Junaid Majeed Bhat, Abhishek Dhar, Sheldon Goldstein, David A. Huse, Manas Kulkarni, Anupam Kundu and Joel L. Lebowitz, Boltzmann Entropy of a Freely Expanding Quantum Ideal Gas, [J. Stat. Phys. 190, 142 \(2023\)](#).

- **List of publications not included in the thesis:**

1. Arghya Das, Abhishek Dhar, Srashti Goyal, Anupam Kundu, Saurav Pandey, COVID-19: Analytic results for a modified SEIR model and comparison of different intervention strategies, [Chaos, Solitons & Fractals 144, 110595 \(2021\)](#).